

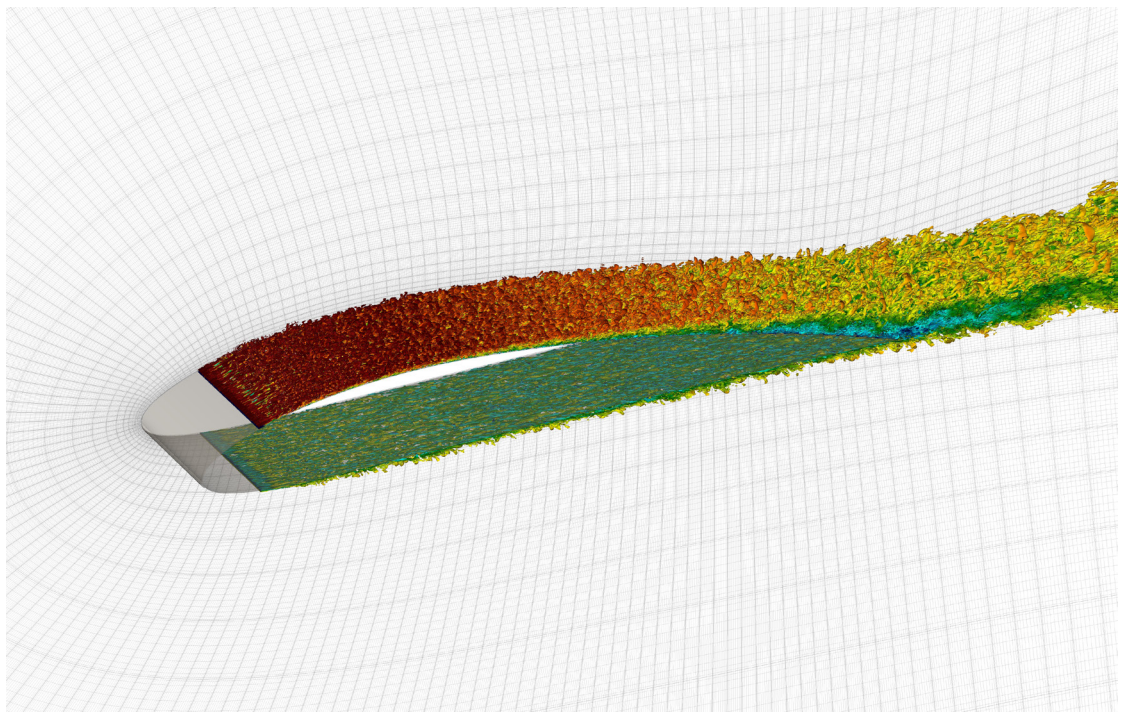


KTH ROYAL INSTITUTE
OF TECHNOLOGY

Doctoral Thesis in Engineering Mechanics

Coherent structures and control in wall-bounded turbulent flows

MARCO ATZORI



Coherent structures and control in wall-bounded turbulent flows

MARCO ATZORI

Academic Dissertation which, with due permission of the KTH Royal Institute of Technology,
is submitted for public defence for the Degree of Doctor of Philosophy on Monday the 14th June
2021, at 10:30 a.m, sal 5316, Faxén, Teknikringen 8, Stockholm.

Doctoral Thesis in Engineering Mechanics
KTH Royal Institute of Technology
Stockholm, Sweden 2021

© Marco Atzori

ISBN 978-91-7873-917-2
TRITA-SCI-FOU 2021:23

Printed by: Universitetsservice US-AB, Sweden 2021

Cover: Vortex clusters coloured with the horizontal velocity component in a high-fidelity numerical simulation of a NACA4412 airfoil at chord Reynolds number $Re_c = 200\,000$.

Coherent structures and control in wall-bounded turbulent flows

Marco Atzori

Simex/FLOW, KTH Engineering Mechanics, Royal Institute of Technology
SE-100 44 Stockholm, Sweden

Abstract

This thesis is concerned with two distinct topics related to the study of wall-bounded turbulence: the connection between instantaneous three-dimensional coherent structures and mean-flow properties, and the development and analysis of pre-determined control techniques for adverse-pressure-gradient boundary layers.

We examined regions with intense velocity fluctuations in various flowcases. In turbulent ducts we found that, on the one hand, the specific geometry of the domain has measurable effects on the shape and dimensions of these structures. On the other hand, however, their contribution to the mean secondary flow, which is the main distinguishing feature of turbulent ducts, is not particularly significant. Intense events contribute to the mean velocity in a similar way as in periodic channels, where the secondary flow is not present. Studying adverse- and zero-pressure-gradient turbulent boundary layers, we found that there are qualitative differences in how intense-fluctuation events affect the mean properties of these two flows. Our results suggest that coherent structures may help to explain history effects and development of the outer peak in wall-tangential fluctuations. An efficient algorithm for percolation analysis and an in-situ adaptor for the simulation code Nek5000 and the visualization software Paraview have also been developed as part of this effort.

We also created a new dataset including various combinations of uniform blowing and suction applied to a NACA4412 airfoil, employing high-fidelity numerical simulations and turbulence models. There are significant discrepancies between how the control interacts with turbulence under different pressure-gradient conditions, a fact that illustrates the need of considering test cases as similar as possible to operative conditions in control studies. We also found that the most promising control configuration for a wide range of Reynolds numbers is uniform blowing applied to the airfoil pressure side. In particular, it reduces both pressure and skin-friction contributions to the total drag, resulting in higher aerodynamic efficiency and potential net-energy saving when the actuation cost is included.

Key words: Turbulent boundary layers, numerical simulations, coherent structures, predetermined flow control.

Koherenta strukturer och kontroll i vägg begränsade turbulenta strömningar

Marco Atzori

Linné FLOW Centre, Kungliga Tekniska högskolan, Institutionen för Mekanik
SE-100 44 Stockholm, Sverige

Sammanfattning

Denna avhandling handlar om två olika ämnen relaterade till studien av vägg begränsad turbulens: sambandet mellan instantanatredimensionella koherenta strukturer och medelflödesegenskaper, och utveckling och analys av förutbestämda kontrolltekniker för gränsskikt med adverse tryckgradient.

Vi undersökte regioner med intensiva hastighetsfluktuationer i olika strömningsfall. I turbulenta rektangulära och kvadratiska kanaler ("ducts") fann vi att å ena sidan domänens specifika geometri har mätbara effekter på formen och storleken hos dessa strukturer. Å andra sidan är deras bidrag till det genomsnittliga sekundär flödet, som är huvudkarateristiken i turbulenta ducts, inte särskilt signifikant. Intensiva händelser bidrar till medelhastigheten på ett liknande sätt som i periodiska kanalströmmar, där sekundärflödet inte finns. När vi studerade adverse och nolltryckgradient turbulenta gränsskikt, fann vi att det finns kvalitativa skillnader i hur intensiva fluktuationer även manger påverkar medelegenskaperna för dessa två flöden. Våra resultat tyder på att sammanhangande strukturer kan hjälpa till att förklara historie effekter och utveckling av den yttre maximum i väggtangentiella fluktuationer. En effektiv algoritm för perkoleringanalys och en in-situ adapter för simuleringskoden Nek5000 och visualiseringsmjukvaran Paraview har också utvecklats som en del av detta arbete.

Vi också skapade en ny dataset med olika kombinationer av enhetlig blåsning och sugning applicerad på en NACA4412-vingprofil, med användning av högkvalitativa numeriska simuleringar och turbulensmodeller. Det finns signifikanta skillnader mellan hur kontrollen interagerar med turbulens under olika tryckgradientsförhållanden, vilket illustrerar behovet av att betrakta testfall som liknar operativa förhållanden i kontrollstudier. Vi fann också att den mest lovande kontrollkonfigurationen för ett brett spektrum av Reynoldstal är jämnt utblåsning applicerad på vingens trycksida. I synnerhet minskar det både tryck- och ytfrictionsbidraget, vilket resulterar i högre aerodynamisk effektivitet och potentiell nettoenergibesparing när kontrollkostnaden inkluderas.

Nyckelord: Turbulenta gränsskikt, numeriska simuleringar, koherenta strukturer, förutbestämd flödeskontroll.

Preface

The first part of the thesis consists of an introduction that explains the project motivations, a summary of selected results, and a brief discussion of our conclusions. The second part of the thesis contains 14 papers. In paper 1, we study the properties of the turbulent boundary layer developing over the suction side of a NACA4412 airfoil at various Reynolds number. In papers 2, 3, and 4, we analyse the effects of uniform blowing and suction applied to two cases considered in paper 1. In papers 5 and 6, we study how pressure gradients and control modify skin-friction generation. In paper 7, we describe the setup of a wind-tunnel experimental campaign that is conducted to validate and extend the results in paper 1. In papers 8 and 9, we study coherent structures, defined as intense Reynolds-stress events, in turbulent flows across square and rectangular ducts. In papers 10 and 11, the same methodology is used to investigate pressure-gradient and control effects in the cases examined in papers 2 and 4. In papers 12 and 13, we present a new and efficient code to perform percolation analysis on turbulent flows. In paper 14, we describe the implementation of an in-situ adaptor for spectral-element code for fluid simulations Nek5000 and the data-analysis software Paraview.

Note that published papers are adjusted to comply with the present thesis format for consistency, but their contents have not been altered as compared with their original counterparts.

Paper 1. R. VINUESA, P. NEGI, M. ATZORI, A. HANIFI, D. HENNINGSON & P. SCHLATTER, 2018. *Turbulent boundary layers around wing sections up to $Re_c = 1,000,000$.* Int. J. Heat and Fluid Flow **72**, 86–99.

Paper 2. M. ATZORI, R. VINUESA, G. FAHLAND, A. STROH, D. GATTI, B. FROHNAPFEL & P. SCHLATTER, 2020. *Aerodynamic effects of uniform blowing and suction on a NACA4412 airfoil.* Flow Turbul. Combus. **105**, 735–759.

Paper 3. M. ATZORI, R. VINUESA, A. STROH, D. GATTI, B. FROHNAPFEL & P. SCHLATTER, 2021. *Blowing and suction applied to non-uniform adverse-pressure-gradient boundary layers.* Internal Report.

Paper 4. G. FAHLAND, A. STROH, B. FROHNAPFEL, M. ATZORI, R. VINUESA, B. FROHNAPFEL, P. SCHLATTER & D. GATTI, 2021. *Investigation of Blowing and Suction for Turbulent Flow Control on Airfoils.* To appear in AIAA J.

Paper 5. Y. FAN, W. LI, M. ATZORI, R. POZUELO, P. SCHLATTER & R. VINUESA, 2020. *Decomposition of the mean friction drag in adverse-pressure-gradient turbulent boundary layers.* Phys. Rev. Fluids **5**, 114608.

Paper 6. Y. FAN, M. ATZORI, R. VINUESA, D. GATTI, P. SCHLATTER & W. LI, 2021. *Friction drag decompositon of the turbulent boundary layers on a NACA4412 airfoil under uniform blowing and suction*. Internal Report.

Paper 7. F. MALLOR, A. PARIKH, E. DOGAN, M. ATZORI, M. HAJIPOUR, N. TABATABAEI, R. ÖRLÜ, R. VINUESA & P. SCHLATTER, 2021. *Design and setup of a wing model in the Minimum-Turbulence-Level wind tunnel*. Internal Report.

Paper 8. M. ATZORI, R. VINUESA, A. LOZANO-DURÁN & P. SCHLATTER, 2018. *Characterization of turbulent coherent structures in square duct flow*. J. Phys.: Conf. Ser. **1001** (1), 012008.

Paper 9. M. ATZORI, R. VINUESA, A. LOZANO-DURÁN & P. SCHLATTER, 2021. *Intense Reynolds-stress events in turbulent ducts*. Int. J. Heat Fluid Flow **89**, 108802.

Paper 10. M. ATZORI, R. VINUESA, A. LOZANO-DURÁN & P. SCHLATTER, 2020. *Coherent structures in turbulent boundary layers over an airfoil*. J. Phys.: Conf. Ser. **105**, 735–759.

Paper 11. M. ATZORI, R. VINUESA & P. SCHLATTER. *Control effects on coherent structures in a non-uniform adverse-pressure-gradient boundary layer*. Internal Report.

Paper 12. W. KÖPP, A. FRIEDERICI, M. ATZORI, R. VINUESA, P. SCHLATTER & T. WEINKAUF. *Notes on Percolation Analysis of Sampled Scalar Fields*. Topology-Based Methods in Visualization (TopoInVis), Nyköping, Sweden, June 17 - 19, 2019.

Paper 13. A. FRIEDERICI, W. KÖPP, M. ATZORI, R. VINUESA, P. SCHLATTER & T. WEINKAUF. *Distributed Percolation Analysis for Turbulent Flows*. 2019 IEEE 9th Symposium on Large Data Analysis and Visualization (LDAV), 2019, pp. 42-51.

Paper 14. M. ATZORI, W. KÖPP, S. W. D. CHIEN, D. MASSARO, F. MALLOR, A. PEPLINSKI, M. REZAEI, N. JANSSON, S. JANSSON, R. MARKIDIS, E. LAURE, P. SCHLATTER & T. WEINKAUF, 2021. *In-situ visualization of large-scale turbulence simulations in Nek5000 with ParaView Catalyst*. Submitted to Journal of Supercomputing.

June 2021, Stockholm

Marco Atzori

Division of work between authors

Philipp Schlatter (PS) is the main advisor of this project, and Ricardo Vinuesa (RV) acts as co-advisor. The project is part of the research efforts coordinated by the consortium “In-Situ Big Data Analysis for Flow and Climate Simulations”, led by Tino Weinkauf (TW). Adrián Lozano-Durán (ALD) provided significant input in the study of coherent structures. Bettina Frohnapfel (BF) had an important role in initiating our work on control, and she coordinated our collaboration with the Karlsruhe Institute of Technology. Weipeng Li (WL) coordinated our collaboration with the Shanghai Jiao Tong University.

Paper 1. The numerical simulation at $Re_c = 1,000,000$ has been set up by Prabal S. Negi (PSN) and run by Ricardo Vinuesa (RV). The domain validation was performed by PSN. Marco Atzori (MA) performed the simulation at $Re_c = 200,000$. The post-processing has been carried out by RV, with input from MA. The paper has been written by RV with feedback from MA, PSN, Ardesir Hanifi, Dan Henningson, and Philipp Schlatter (PS).

Paper 2. The LESs have been performed by MA, with input from RV and PS. The RANS simulations have been performed by Georg Fahland (GF) with help from Alexander Stroh (AS) and Davide Gatti (DG). The post-processing has been carried out by MA, with input from RV (LESs), and by GF (RANS simulations). The paper has been written by MA with input from GF, RV, and PS. RV, PS, AS, DG, and BF revised the manuscript and provided feedback.

Paper 3. The LESs and post-processing has been performed by MA, with input from RV and PS. The paper has been written by MA, with input from RV and PS. RV, AS, DG, BF, and PS revised the manuscript and provided feedback.

Paper 4. The RANS simulations have been performed by GF, with input from AS, BT, and DG. The post-processing was carried out by GF (RANS data-set), and by MA (LES data-set). The paper has been written by GF, with input from MA, AS, BF, and DG, who also coordinated the work. BF, RV, PS and DG revised the manuscript and provided feedback.

Paper 5. The data-set has been analysed by Yitong Fan (YF), with input from WL, and from MA (for the NACA4412 data-set) and Ramon Pozuelo (RP, for the APG data-set). The paper has been written by YF, with input from WL. WL and RV initiated the work. WL, MA, RP, PS, and RV revised the manuscript and provided feedback.

Paper 6. The data-set has been analysed by YF, with input from MA. The LESs of control cases at $Re_c = 400,000$ have been performed by MA. The paper has been written by YF, with input from MA. WL coordinated the work and WL, MA, RV, DG, and PS revised the manuscript and provided feedback.

Paper 7. Fermín Mallor (FM), Agastya Parikh (AP) and Eda Dogan (ED) constructed the experimental set-up with input from Ramis Örlü (RO), and Majid Hajipour (MH). The experimental set-up was designed by ED, FM, AP, with input from RO, RV, and PS. A preliminary set of RANS simulations was

performed by MA and FM, and the set of RANS that appears in the paper have been performed by Narges Tabatabaei (NT). The post-processing has been performed by FM, MH and NT, with input from RV, RO, ED and PS. The paper has been written by FM, AP, and NT, with input from MH and MA. ED, MH, RV, RO, and PS revised the manuscript and provided feedback.

Paper 8. The structure analysis has been performed by MA, with input from RV, ALD, and PS. The paper has been written by MA, with input from RV. RV, ALD, and PS revised the manuscript and provided feedback.

Paper 9. The structure analysis has been performed by MA, with input from RV, ALD, and PS. The paper has been written by MA, with input from RV. RV, ALD, and PS revised the manuscript and provided feedback.

Paper 10. The structure analysis has been performed by MA, with input from RV, ALD, and PS. The paper has been written by MA, with input from RV. RV, ALD, and PS revised the manuscript and provided feedback.

Paper 11. The structure analysis has been performed by MA, with input from RV and PS. The paper has been written by MA, with input from RV. RV and PS revised the manuscript and provided feedback.

Paper 12. The data analysis has been performed by Wiebke Köpp (WK) and Anke Friederici (AF), with input from MA and Tino Weinkauf (TW). The paper has been written by WK and AF, with input from MA and TW. TW coordinated the work. MA, RV, PS, and TW revised the manuscript and provided feedback.

Paper 13. The percolation code has been developed by AF and WK. The data analysis has been performed by AF and WK, with input from MA. The paper has been written by WK and AF, with input from MA. TW coordinated the work. MA, RV, PS, and TW revised the manuscript and provided feedback.

Paper 14. The paper was initiated by Stefano Markidis (SM). The code has been developed by Niclas Jansson (NJ) and Mohamad Rezaei (MR), with input from MA. Test simulations have been performed by Daniele Massaro (DM) and FM, with input from MA and WK (for the visualization pipeline). The performance analysis has been carried out by WK and Steven W. D. Chien (SWDC), with input from SM. The paper has been written by MA, with input from WK, SWDC, SM, and NJ. TW, Erwin Laure (EL), and PS coordinated the work. Adam Peplinski, SM, RV, EL, PS, and TW revised the manuscript and provided feedback.

Other publications

The following papers, although related, are not included in this thesis.

R. VINUESA, A. PEPLINSKI, M. ATZORI, L. FICK, O. MARIN, E. MERZARI, P. NEGI, A. TANARRO & P. SCHLATTER, 2018. *Turbulence statistics in a spectral-element code: a toolbox for high-fidelity simulations*. Technical Report. TRITA-SCI-RAP 2018:010.

M. ATZORI, R. VINUESA, A. LOZANO-DURÁN & PHILIPP SCHLATTER, 2019. *Contribution of Reynolds-stress structures to the secondary flow in turbulent ducts*. Proceeding of the 11th International Symposium on Turbulence and Shear Flow Phenomena (TSFP-11).

M. ATZORI, R. VINUESA, D. GATTI, A. STROH, B. FROHNAPFEL & P. SCHLATTER, 2019. *Effects of different friction control techniques on turbulence developing around wings*. Proceedings of Direct and Large-Eddy Simulation (DLES) 12.

W. KÖPP, M. ATZORI, M. REZAI, N. JANSSON, R. VINUESA, E. LAURE, P. SCHLATTER & T. WEINKAUF, 2020. *Effects of Blowing and Suction on the Turbulent Flow around an Airfoil*. Entry V0058 at the Gallery of Fluid Motion <https://doi.org/10.1103/APS.DFD.2020.GFM.V0058>.

Conferences

Part of the work in this thesis has been presented at the following international conferences. The presenting author is underlined.

M. ATZORI, R. VINUESA & P. SCHLATTER. *Assessment of skin-friction-reduction techniques on a turbulent wing section*. ETMM12. Montpellier, France, 2018.

R. VINUESA, P. NEGI, M. ATZORI, A. HANIFI, D. HENNINGSON & P. SCHLATTER. *Reynolds-number effects in turbulent boundary layers around wing sections*. ETMM12. Montpellier, France, 2018.

M. ATZORI, R. VINUESA, A. LOZANO-DURÁN & P. SCHLATTER. *Coherent structures and secondary motion in turbulent square duct*. Euromech Colloquium 598. London, United Kingdom, 2018.

A. FRIEDERICI, W. KÖPP, M. ATZORI, R. VINUESA, P. SCHLATTER & T. WEINKAUF. *An efficient algorithm for percolation analysis and its application in turbulent duct flow*. Euromech Colloquium 598. London, United Kingdom, 2018.

G. FAHLAND, A. STROH, D. GATTI, B. FROHNAPFEL, M. ATZORI, R. VINUESA & P. SCHLATTER. *RANS Investigation of Blowing and Suction for Turbulent Flow Control on a Wing Section*. EDRCM. Karlsruhe, Germany, 2019.

M. ATZORI, R. VINUESA, G. FAHLAND, A. STROH, D. GATTI, B. FROHNAPFEL & P. SCHLATTER. *Effects of Uniform Blowing and Suction on Turbulent Wing Boundary Layers*. EDRCM. Karlsruhe, Germany, 2019.

M. ATZORI, R. VINUESA, A. LOZANO-DURÁN & P. SCHLATTER. *Contribution of Reynolds-stress structures to the secondary flow in turbulent ducts*. TSFP-11. Southampton, United Kingdom, 2019.

- F. MALLOR, E. DOGAN, M. ATZORI, A. PARIKH, R. VINUESA, R. ÖRLÜ & P. SCHLATTER. *Design considerations for the flow conditions around a wing model inside a wind tunnel.* Svenska Mekanikdagar. Stockholm, Sweden, 2019.
- W. KÖPP, A. FRIEDERICI, M. ATZORI, R. VINUESA, P. SCHLATTER & T. WEINKAUF. *Notes on Percolation Analysis of Sampled Scalar Fields.* TopoInVis 2019. Nyköping, Sweden, 2019.
- A. FRIEDERICI, W. KÖPP, M. ATZORI, R. VINUESA, P. SCHLATTER & T. WEINKAUF. *Distributed Percolation Analysis for Turbulent Flows.* 9th IEEE Symposium LDAV 2019. Vancouver, Canada, 2019.
- M. ATZORI, R. VINUESA, D. GATTI, A. STROH, B. FROHNAPFEL & P. SCHLATTER. *Effects of different friction control techniques on turbulent wings.* ERCOFTAC Workshop DLES 12. Madrid, Spain, 2019.
- M. ATZORI, R. VINUESA, A. LOZANO-DURÁN & P. SCHLATTER. *Is the secondary flow of Prandtl's second kind due to intense Reynolds-stress events?* 72rd Annual Meeting of the APS Division of Fluid Dynamics. Seattle, USA, 2019.
- M. ATZORI, R. VINUESA, G. FAHLAND, A. STROH, D. GATTI, B. FROHNAPFEL & P. SCHLATTER. *Increasing the aerodynamic efficiency of a NACA4412 airfoil with blowing and suction.* 73rd Annual Meeting of the APS Division of Fluid Dynamics. Chicago (Virtual), USA, 2020.

Contents

Abstract	v
Sammanfattning	vi
Preface	vii
 Part I - Overview and summary	
Chapter 1. Introduction	1
1.1. Context and motivations	3
1.2. Numerical simulations	8
Chapter 2. Control applied to a NACA4412 airfoil	9
2.1. Turbulent statistics	10
2.2. Aerodynamic properties	23
Chapter 3. Coherent structures	28
3.1. Intense events in turbulent ducts	29
3.2. Intense events in boundary layers over airfoils	49
3.3. Turbulent structures and time tracking	55
Chapter 4. Conclusions and Outlook	58
4.1. Control strategies	58
4.2. Coherent structures	59
Acknowledgements	62
Bibliography	63

Part II - Papers

Summary of the papers	69
Paper 1. Turbulent boundary layers around wing sections up to $Re_c = 1,000,000$	77
Paper 2. Aerodynamic effects of uniform blowing and suction on a NACA4412 airfoil	111
Paper 3. Blowing and suction applied to non-uniform adverse-pressure-gradient boundary layers	143
Paper 4. Investigation of Blowing and Suction for Turbulent Flow Control on Airfoils	177
Paper 5. Decomposition of the mean friction drag in adverse-pressure-gradient turbulent boundary layers	223
Paper 6. Friction drag decompositon of the turbulent boundary layers on a NACA4412 airfoil under uniform blowing and suction	247
Paper 7. Design and setup of a wing model in the Minimum-Turbulence-Level wind tunnel	283
Paper 8. Characterization of turbulent coherent structures in square duct flow	311
Paper 9. Intense Reynolds-stress events in turbulent ducts	333
Paper 10. Coherent structures in turbulent boundary layers over an airfoil	363
Paper 11. Control effects on coherent structures in a non-uniform adverse-pressure-gradient boundary layer	383
Paper 12. Notes on Percolation Analysis of Sampled Scalar Fields	405
Paper 13. Distributed Percolation Analysis for Turbulent Flows	425
Paper 14. In-situ visualization of large-scale turbulence simulations in Nek5000 with ParaView Catalyst	455

Part I

Overview and summary

CHAPTER 1

Introduction

The PhD project described in this thesis lasted from January 2017 to April 2021. I illustrate its different branches in Figure 1.1 and explain how it reaches the current state hereafter.

Our original aim was to study non-uniform adverse-pressure-gradient turbulent boundary layers and blowing and suction applied on these flows. During the first half of 2017, I started using Nek5000 to carry out simulations of the boundary layers around a NACA4412 airfoil (**Paper 1**). Soon after the project's beginning (March 2017), I joined the "In-Situ Big Data Analysis for Flow and Climate Simulations" consortium led by Tino Weinkauf, which aims to develop effective data-analysis tools for large numerical simulations. In June 2017, I started collaborating with Adrián Lozano-Durán at the third turbulent workshop (Madrid). During the workshop, I worked on square ducts and coherent structures (**Paper 8**). Although this was originally considered a test case only, I eventually spent a significant amount of time investigating the connections between intense Reynolds-stress events and secondary flow.

Between the end of 2017 and the beginning of 2018, following our first experience with coherent structures, Wiebke Köpp and Anke Friederici developed an efficient algorithm for percolation analysis (**Papers 12 & 13**), and we began to collaborate with Davide Gatti, Alexander Stroh, and Bettina Frohnapfel to study control strategies applied to the NACA4412 airfoil. Georg Fahland joined this collaboration soon after to perform RANS simulations of the same setup (**Papers 2, 3, & 4**). In 2018, I continued to work on coherent structures in the duct (**Paper 9**) and control simulations. A new part of the project also became relevant, which was to aid Mohamad Rezai, Wiebke Köpp, Anke Friederici, and Tino Weinkauf in developing an in-situ adaptor for Nek5000 and Catalyst-Paraview. This task was completed in the last quarter of 2018 with Niclas Jansson's help.

In June 2019, I started to work on coherent structures in turbulent boundary layers at the fourth turbulent workshop in Madrid (**Papers 10 & 11**) and to collaborate with Yitong Fan and Wiepeng Li to apply friction decompositions on turbulent boundary layers (**Papers 5 & 6**). Ramon Pozuelo provided data for this effort later. I was also involved in performing a preliminary set of RANS simulations to design an experiment at the KTH MTL wind tunnel

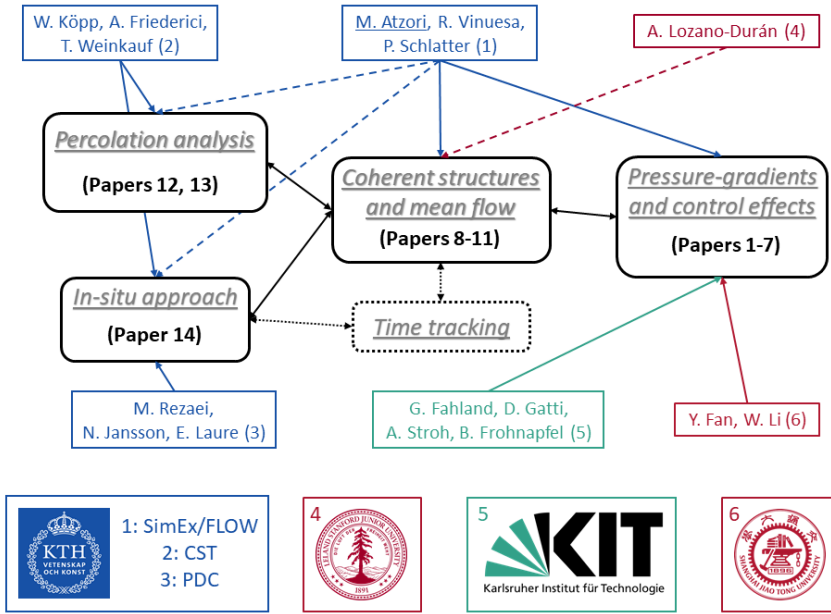


Figure 1.1: Branches and main collaborators of this project. The solid and dashed lines between topics and researchers denote leading and supporting roles, respectively.

(Paper 7). Fermín Mallor performed the simulations, and the experimental setup was eventually prepared by Fermín Mallor, Agastya Parikh, and Ramis Örlü with the help of Eda Dogan and, later, Narges Tabatabaei, who also performed a new set of RANS simulations. In the second half of 2019, I started to work with Miguel Zavala on in-situ tracking of coherent structures (we have not obtained significant results from a physical perspective yet). During the second half of 2019 and the first half of 2020, we performed tests on in-situ visualization (**Paper 14**), with the help of Fermín Mallor and Daniele Massaro (who performed simulations with in-situ visualization), Stefan Wei Der Chien and Stefano Markidis (who performed performance analysis), and Wiebke Köpp and Tino Weinkauf (who worked on the instructions for Paraview).

For the most part, 2020 saw the continuation of what was already in progress. The COVID-19 pandemic, which started to have tangible effects in Sweden from the second quarter of the year, had some repercussions on the project due to additional workload for many of the people involved and more difficult working conditions.

This project touched upon three distinct topics: 1) control effects on boundary layer with non-uniform adverse pressure gradients, 2) coherent structures and their connection with mean-flow properties, and 3) development of efficient data-analysis tools for numerical simulations. I had a leading role working on the first two topics, carrying out a significant portion of the simulations and post-processing tasks. I had a supporting role working on the last topic, *e.g.* providing expertise in computational fluid dynamics (CFD) to collaborators who were less familiar with this field.

Thesis structure. The first part of the thesis is an introduction and an overview of the project. In this Chapter, I briefly discuss the project motivations and provide a general description of the setup of our simulations. I present selected results on control effects in adverse-pressure-gradient boundary layers in Chapter 2 and on coherent structures in Chapter 3. In Chapter 4, I summarize our conclusions. The second part of the thesis contains published papers and technical reports that provide a more detailed description of our work. Overlapping between the two parts has been reduced as much as possible.

1.1. Context and motivations

The motivations of this project stem from, on the one hand, the relevance that wall-bounded turbulent flows have for our society and, on the other hand, the scientific and technical challenges that their understanding still poses. In the present section, I describe why the three main topics encountered in this project, *i.e.* control strategies, instantaneous coherent structures, and efficient data-analysis tools, are relevant in the general context of research on turbulence.

1.1.1. Control strategies

Turbulent flows are crucial in many industrial applications and natural phenomena. In the case of turbulent boundary layers developing on airfoils, effective control strategies for drag reduction would be highly beneficial for economic reasons and transport sustainability. The volume of air transport and the related greenhouse-gas emissions increased significantly in the last decades, and this trend will most likely continue once the COVID-19 pandemic ends. Figure 1.2 (top) shows the total CO₂ emissions due to aviation and its corresponding share of global emissions from 1950 to 2018 (data exported from Lee *et al.* 2021). Between 2010 and 2018, following a temporary decrease due to the financial crisis (2008), the aviation emissions had a yearly growth rate of 4 – 5%, reaching 1.04 billion tons and twice the amount of 1987. The comparable increase of all other emission sources over the same period has kept the total share at a low level of about 2.5%, although this share has also moderately increased, particularly in the last years. There are two main reasons why aviation emissions should not be overlooked, despite the relatively low share of total emissions. The first reason is that we do not currently have technology that would allow decarbonisation of air travelling, *e.g.* battery specific capacity would need to double in order

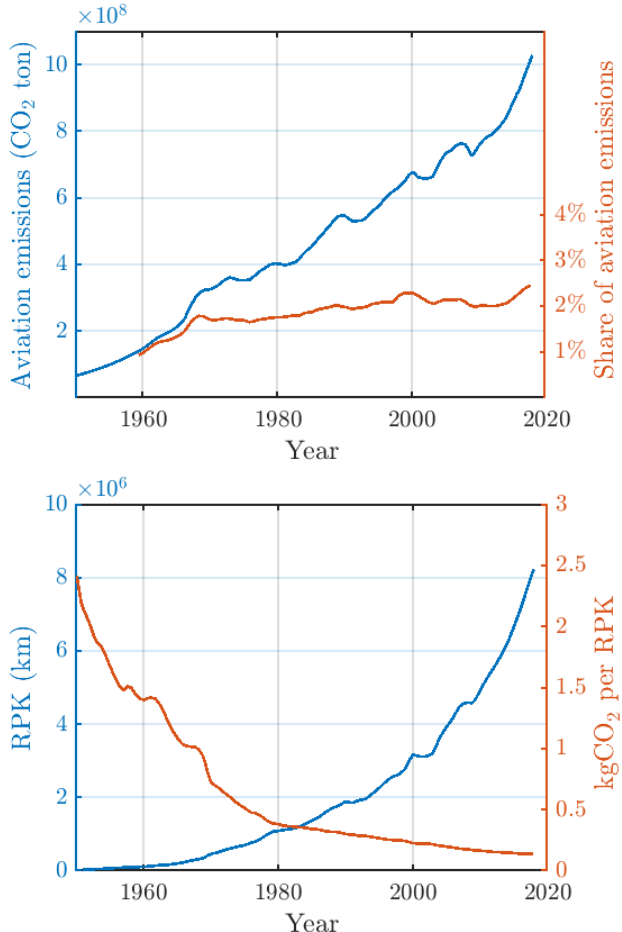


Figure 1.2: (Top) Aviation CO₂ emissions and corresponding share of total emissions and (bottom) revenue passenger kilometre (RPK) and emission per RPK from 1950 to 2018.

to make electric engines a viable solution for commercial airplanes (Bills *et al.* 2020).

The second reason, which also explains the more rapid increase in the share of total emission in the last years, is shown in Figure 1.2 (bottom) (data exported from Lee *et al.* 2021). This figure illustrates the revenue passenger kilometres (RPK), defined as the number of paying customers multiplied by the distance travelled, which is a measure of the total traffic, and the CO₂ emission per revenue passenger kilometre (kgCO₂ per RPK), which is a measure of efficiency. According to this metric, aviation efficiency was twenty times higher in 2018 than

in 1950 and eleven times higher than in 1960. This efficiency increase helped to reduce the total emissions. Air traffic will rise in the foreseeable future, while further gains in efficiency become progressively more difficult, which motivates the effort of developing control strategies. Unfortunately, effective control strategies have not been adopted on a large scale yet, notwithstanding the many academic studies in this area.

In studies on control, a crucial question is how to identify the most appropriate framework and test cases. Simulations seem to have advantages over experiments in this area because they allow “decoupling” technological difficulties (*e.g.* designing actuators) and theoretical questions. However, there is the potential danger of considering too unrealistic scenarios. In addition, the available computational resources do not allow high-fidelity numerical simulations of realistic study cases, and codes suited for complex geometries are often not optimized to deal with a very high number of degrees of freedom. At present, a substantial portion of numerical studies on control has been carried out on channel flows (*e.g.* Choi *et al.* 1994; Sumitani & Kasagi 1995) and zero-pressure-gradient boundary layers (*e.g.* Park & Choi 1999; Kametani *et al.* 2015; Mahfoze *et al.* 2019). Although it is perhaps reasonable to assume that the most important dynamic processes are similar in all wall-bounded turbulent flows, external and developing flows have specific properties. Furthermore, control effects on quantities such as lift and total drag in airfoils depend on changes in the global pressure distribution, which can also influence the control energy cost.

In this context, we created a new dataset using highly-resolved large-eddy simulations (LES) and Reynolds-averaged Navier–Stokes (RANS) simulations to describe the effects of uniform blowing and suction on a NACA4412 airfoil at various Reynolds numbers. The dataset is presented in **Papers 1, 2, & 3**, and we described the process of skin-friction generation and the impact of control strategies on coherent turbulent structures in **Papers 4-6, & 11**. During this project, an experimental campaign has also been initiated to corroborate the results of numerical simulation **Paper 7**.

1.1.2. *Coherent structures*

An important question in the study of any phenomenon related to turbulence is which data-analysis tools are most useful. Fully-developed turbulent flows are chaotic systems with a high number of independent degrees of freedom. Their mean properties are typically the most relevant ones from the application point of view, but they provide limited insights into the flow dynamics. Because of this reason the scientific community has tried to extract additional information from the instantaneous flow to formulate simplified models since the beginning of fluid mechanics. A possible option is to focus on regions of the flow that can be identified based on a specific condition, *i.e.* to study (instantaneous) “coherent structures”. We can gain an insightful perspective on how this approach has

evolved in the last decades by comparing the reviews by Hussain (1986) and Jiménez (2018).

In 1986, Fazle Hussain explained that coherent structures “*are the embodiment of our desire to find order in apparent disorder*” and conjectured that “*presumably being the tractable part of turbulent flows, [they] may contain most of the essential physics of turbulence*”. He also identifies the lack of data at the time as an issue that prevented further advancements, but he was hopeful on the application of this concept and wrote: “*We expect to see in the near future significant thrusts and accomplishments in turbulence management via coherent structures manipulation using active and passive controls.*”

More than 30 years later, and indeed after the beginning of this project, Jiménez (2018) summarized the advancements in this topic. He acknowledged that we have now much more information about the properties of single structures, such as the shape and time evolution of vortex clusters or ejection and sweeps, and the details of the near-wall cycle, which explains some of the relevant dynamics in wall-bounded turbulent flows (Kline *et al.* 1967; Gupta *et al.* 1971), but he also pointed out that there are still very significant open questions, such as the nature of the interactions between structures of different scales and the connection between instantaneous structures and mean velocity. Note that vortex clusters are regions of the flow where the rotational shear is more prominent than the shear stress (Jeong & Hussain 1995; Cucitore *et al.* 1999), and sweeps and ejections are structures defined in the context of the quadrant analysis (Wallace *et al.* 1972). Sweeps are regions of the flow where velocity fluctuations are positive in the streamwise direction and negative in the wall-normal direction, and ejections are regions of the flow where velocity fluctuations are negative in the streamwise direction and positive in the wall-normal direction.

Similarly to what happened for control strategies, many of the studies on coherent structures in the scientific literature have been carried out on canonical flows such as the periodic channel. This approach is perhaps more appropriate for coherent structures than for control strategies because of the more fundamental nature of these studies. Nevertheless, it leaves unanswered the question of whether we can use coherent structures to explain specific phenomena that occur in more complex flows. In this project, we investigated how intense Reynolds-stress events are related to the secondary flow of Prandtl’s second kind in turbulent ducts (**Papers 8 & 9**) and to the properties of non-uniform adverse-pressure-gradient boundary layers, including cases with control (**Papers 10 & 11**).

1.1.3. Efficient codes for data analysis

The cost of numerical simulations of a certain physical system is related to its number of degrees of freedom. In turbulent flows, the number of degrees of freedom is a measure of separation between (large) scales which carry a significant fraction of the energy and (small) scales responsible for energy dissipation, and

it can be estimated from the governing equations. The governing equations for Newtonian incompressible flows are:

$$\begin{aligned} \frac{\partial u_i}{\partial t} + u_j \frac{\partial u_i}{\partial x_j} &= -\frac{\partial p}{\partial x_i} + \frac{1}{Re} \frac{\partial^2 u_i}{\partial x_j \partial x_j} \\ \frac{\partial u_i}{\partial x_i} &= 0, \end{aligned} \quad (1.1)$$

where Re denotes the Reynolds number, u_i are the instantaneous velocity components, p is the pressure, x_i are the spatial coordinates, and t is time. Note that the summation convention applies for repeated indices. The Reynolds number $Re = UL/\nu$, defined in terms of a characteristics velocity U and length L , and the kinematic viscosity of the fluid, ν , is the only dimensionless parameter in these equations. Dimensional analysis based on energy conservation suggests that the ratio between the largest and the smallest scales is of the order of $Re^{3/4}$ (Frisch 1995), resulting in about $Re^{9/4}$ degrees of freedom for three-dimensional isotropic turbulence, which directly correlate with the number of grid points in a simulation without turbulence models. Choi & Moin (2012) formulated a more precise estimate for the specific case of a turbulent boundary layer developing over a flat plate, and they found that the number of grid points as a function of the Reynolds number scales as $Re_{L_x}^{13/7}$ for wall-resolved large-eddy simulations, and as $Re_{L_x}^{37/14}$ for direct numerical simulations. Note that Re_{L_x} is the Reynolds number based on the free-stream velocity and the flat-plate length. In practice, the number of grid points in the computational domain is also influenced by technical factors such as the meshing strategy, and it is typically extremely high for realistic Reynolds numbers.

The actual simulation costs in terms of CPU hours, memory, and storage requirements depend not only on the number grid points, but on both the numerical code and the methodology for data analysis as well. Assessing which of these requirements is the limiting factor depends on the available infrastructures. Note that central-processing-unit (CPU) hours measures the time required to execute a certain set instructions in a computer. Over the last decades, the increase of computational power due to technological progresses and investments, together with the development of more efficient software, allowed to carry out progressively larger simulations. For instance, Lee & Moser (2015) performed direct numerical simulations (DNSs) of turbulent channel flows using up to 121×10^9 grid points, and even higher numbers of grid points are employed in more fundamental studies on isotropic turbulence (Yeung & Ravikumar 2020).

Ideally, advancements in performing simulations are followed by corresponding improvements in storage capacity and performances of post-processing tools. Storage and post-processing techniques are, in fact, two aspects of the same challenge. On the one hand, assuming that there is enough computational power to carry out a certain simulation, the available storage determines the amount of data that can be saved, which set performance requirements for the

post-processing code. On the other hand, post-processing analyses determine the minimum amount of data which is needed. We worked on both sides of this topic during the project. In **Papers 12 & 13**, we present an efficient parallel algorithm for percolation analysis, which is the most expensive post-processing step in studies on coherent structures as **Papers 8–11**. In **Paper 14**, we present a preliminary performance measurement of in-situ visualization using Nek5000 and Paraview-Catalyst. The in-situ approach consists of linking a CFD code with external libraries, *e.g.* for image rendering, which can be used during the simulation, thus reducing the storage requirements significantly.

1.2. Numerical simulations

Most of the numerical simulations carried out during this project used codes already developed that required only maintenance interventions.

The LES of NACA4412 airfoil with and without control mentioned in **Papers 1–6, 10, 11, & 14** have been carried out using the open-source code Nek5000 (Fischer *et al.* 2008). This code is based on the spectral-element method (SEM) proposed by Patera (1984), which is a high-order variant of the finite-element method. The computational domain is divided into elements and, within each element, velocity and pressure are represented using a nodal base of Legendre polynomials. All the simulations mentioned in this project were performed using the $P_N P_{N-2}$ formulation (Maday & Patera 1984). In each element, velocity and pressure are defined on N^3 quadrature points distributed according to the Gauss–Lobatto–Legendre rule and $(N - 2)^3$ points distributed according to the Gauss–Lobatto rule, respectively, where $N - 1$ is the polynomial order. Velocity and pressure are decoupled using a time-splitting operation with a block LU decomposition (Fischer 1997). This code exhibits a high parallel efficiency which, together with the fast error convergence of high-order methods, makes it particularly suitable for simulations of incompressible flows from moderate to high Reynolds numbers (El Khoury *et al.* 2013; Offermans *et al.* 2016)

With respect to the released version of Nek5000, three components were added: tripping to induce laminar-to-turbulence transition, an implicit relaxation-time filter for LES, and a specific outflow boundary condition. The tripping is that used by Schlatter & Örlü (2012), with affects the flow similarly as devices in wind-tunnel experiments. It is defined as a pseudo-random force in the wall-normal direction with a 3D-Gaussian shape that changes with given time and spatial scales. Hosseini *et al.* (2016) used the same implementation to perform the first DNS simulation of a NACA4412 airfoil with turbulent flows. The LES filter is based on that employed in the deconvolution model proposed by Stolz *et al.* (2001) and Schlatter *et al.* (2004), and it consists of a volume force derived from the filtered velocity that acts on a certain number of the highest spectral modes. Its implementation in Nek5000 has been validated on channel-flow and airfoil simulations (Negi *et al.* 2018; Vinuesa *et al.* 2018). The outflow condition proposed by Dong *et al.* (2014) introduces local stress on the

outflow boundary if there is an energy flux from the boundary to the domain. I refer to **Papers 1 & 2** for a description of the simulation setup, and the PhD theses by Brynjell-Rahkola (2017) and Offermans (2019) for additional information about Nek5000.

The RANS simulations in **Papers 4 & 7** were performed with the finite-volume open-source code OpenFOAM (Weller *et al.* 2019), using the Semi-Implicit Method for Pressure-Linked Equations (SIMPLE) algorithm (Patankar & Spalding 1972). The discretization in OpenFOAM has been described *e.g.* by Holzmann (2018).

CHAPTER 2

Control applied to a NACA4412 airfoil

The application of control strategies on airfoils such as the NACA4412 profile is relevant and interesting under two different perspectives, *i.e.* how the control interacts with wall-bounded turbulence, and how it modifies aerodynamic properties. We created a new dataset to study uniform blowing and uniform suction using highly-resolved LES on a set of cases at moderate Reynolds numbers and RANS for a more extensive parameter study. The LES cases considered later on are listed in Table 2.1. R2REF and R4REF denote the uncontrolled cases at chord Reynolds numbers $Re_c = 200\,000$ and $400\,000$, respectively ($Re_c = U_\infty c/\nu$, where U_∞ is the incoming free-stream velocity, c is the chord length, and ν is the kinematic viscosity), and angle of attack 5° . An overview of the domain, including vortex clusters in the turbulent region and the spectral elements, is shown in Figure 2.1. The airfoil chord is aligned with the horizontal axes and the incoming flow velocity determines the angle of attack. The boundary conditions are determined using precursor RANS simulations on a much larger domain and laminar-to-turbulent transition is induced using tripping at $x/c = 0.1$ on both suction and pressure sides. Note that x/c denotes the distance from the airfoil leading edge along the chord normalized with the chord length, so that $x/c = 0$ and $x/c = 1$ are the locations of the (nominal) leading and trailing edges, respectively. The simulations are carried in dimensionless units, using a Cartesian frame of reference with origin coinciding with one vertex of leading edge. However, a rotated frame of reference for the turbulent statistics, and the subscripts $(\dots)_t$ and $(\dots)_n$ denote the wall-tangential and wall-normal directions, respectively. The configurations with control at lower Re_c includes uniform blowing and uniform suction applied on the suction side, and uniform blowing applied on the pressure side with two different intensities, *i.e.* $0.1\%U_\infty$ and $0.2\%U_\infty$. In addition, R2BD1 denotes a case with body-force damping, implemented to suppress velocity fluctuations in the wall-normal direction (Stroh *et al.* 2016) and calibrated to have similar effects on the skin friction as those of uniform blowing with $0.1\%U_\infty$ intensity. The control region is between $0.25 < x/c < 0.86$ for cases with control applied on the suction side and $0.2 < x/c < 1.00$ for cases with control applied on the pressure side. Note that the control region is shorter on the suction side to avoid mean separation. At higher Re_c , simulations have been carried out only for three control configurations with blowing or suction with the lowest intensity.

Table 2.1: Summary of the large-eddy simulations on airfoil with control considered in the present chapter.

Case	Control strategy
$Re_c = 200,000$	
R2REF ■	Reference case
R2BL1 ■	Uniform blowing ($0.1\%U_\infty$), suction side
R2BL2 ■	Uniform blowing ($0.2\%U_\infty$), suction side
R2SC1 ■	Uniform suction ($0.1\%U_\infty$), suction side
R2SC2 ■	Uniform suction ($0.2\%U_\infty$), suction side
R2BD1 ■	Body-force damping, suction side
R2PB1 ■	Uniform blowing ($0.1\%U_\infty$), pressure side
R2PB2 ■	Uniform blowing ($0.2\%U_\infty$), pressure side
$Re_c = 400,000$	
R4REF ■	Reference case
R4BL1 ■	Uniform blowing ($0.1\%U_\infty$), suction side
R4SC1 ■	Uniform suction ($0.1\%U_\infty$), suction side
R4PB1 ■	Uniform blowing ($0.1\%U_\infty$), pressure side

A particular control configuration that was also examined consists of a combination of blowing applied on the pressure side and suction applied on the suction side (**Papers 2 & 4**). This setup has the advantage of producing a zero net-flow rate, which could be beneficial in an industrial implementation, but it is ignored in this summary because coupling effects between control applied on both sides are almost negligible.

2.1. Turbulent statistics

The boundary layer developing on the suction side of a NACA4412 airfoil is subjected to a non-uniform adverse-pressure-gradient (APG) that rapidly grows from the point of maximum camber ($x/c = 0.4$) to the trailing edge ($x/c = 1.0$). The Clauser parameter, β , which is an indicator of the intensity of pressure-gradient effects, increases from ≈ 0.6 at ($x/c = 0.4$) to ≈ 170 at ($x/c = 1.0$) in the reference case at $Re_c = 200,000$, and from ≈ 0.6 to ≈ 140 at $Re_c = 400,000$. On the contrary, the boundary layer on the pressure side is subjected to a relatively weak favourable pressure gradient, which results in the lowest value of $\beta \approx -0.3$ at the trailing edge in both references cases. Note that $\beta = \delta^*/\tau_w dP/dx_t|_e$, where δ^* is the displacement thickness, τ_w is the wall-shear stress and $dP/dx_t|_e$ is the pressure gradient in the wall-tangetial direction evaluated at the boundary-layer edge. The wall-normal distance of the boundary-layer edge is identified using a method based on the diagnostic scaling (Vinuesa *et al.* 2016), as discussed in **Paper 1**.

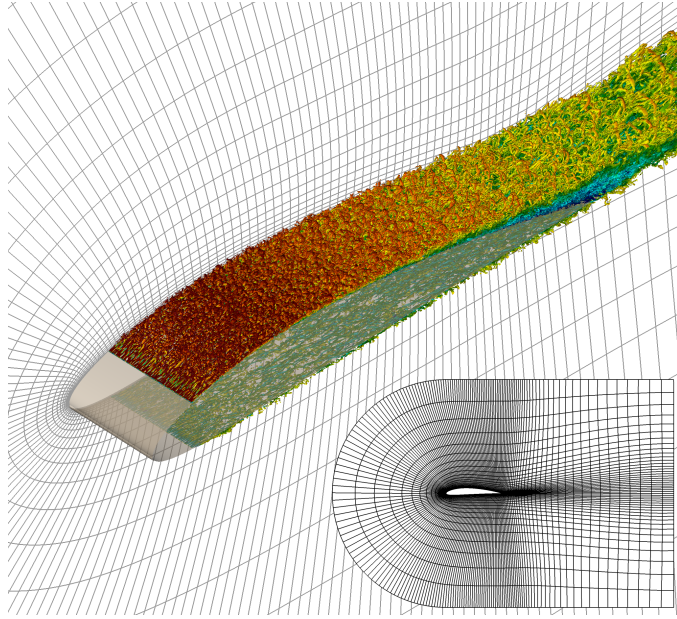


Figure 2.1: Spectral elements in a portion of the computational domain and vortex clusters for case R2REF (NACA4412 at $Re_c = 200,000$), colored with the streamwise velocity (dark red is $1.6U_\infty$ and dark blue $-0.18U_\infty$) and (insert) side view of the domain.

In the following, we will describe pressure-gradient effects comparing suction and pressure sides, and control effects comparing control and uncontrolled cases.

2.1.1. Boundary-layer development

The most evident consequences of strong adverse pressure gradients are perhaps the increase of boundary-layer thickness and decrease of skin friction. Figure 2.2 shows the Reynolds number based on the momentum thickness, denoted Re_θ , for all considered cases. Note that $Re_\theta = \theta U_e / \nu$, where $\theta = \int_0^{\delta_{99}} U_t / U_e (1 - U_t / U_e) dy_n$, y_n is the wall-normal distance, U_t is the mean velocity component in the wall-tangential direction, and $U_e = U_t(\delta_{99})$. On the pressure side, because of the streamwise development, Re_θ increases from ≈ 210 at $x/c = 0.2$ to ≈ 800 at $x/c = 1.0$ for the reference case at $Re_c = 400,000$ (R4REF). On the suction side, however, the growth rate of the boundary-layer thickness is much higher, and Re_θ increases from ≈ 380 at $x/c = 0.2$ to almost 3000 at $x/c = 1.0$ in the same case. Uniform blowing leads to an even higher momentum thickness and Re_θ . The effects of blowing with intensity 0.2% U_∞ at $Re_c = 200,000$ are quite significant. In particular, at the end of the control region, $x/c = 0.86$, Re_θ is increased from $\approx 1,300$ to $\approx 1,600$. On the other hand, both uniform suction

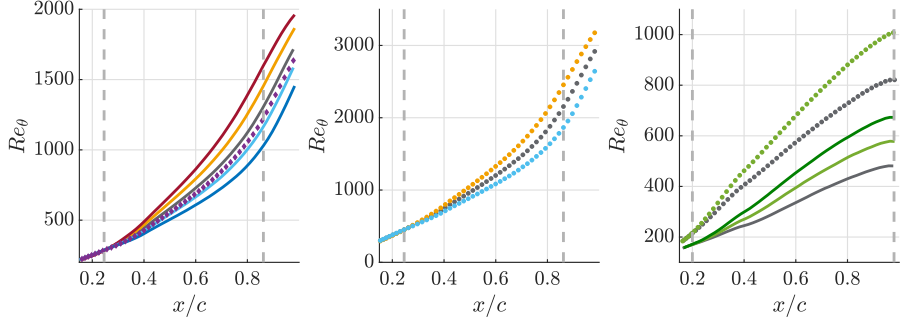


Figure 2.2: Reynolds number based on the momentum thickness as a function of the chord location, denoted by Re_θ and x/c , respectively, for (left) suction side for cases at $Re_c = 200,000$, (center) suction side for cases at $Re_c = 400,000$, and (right) pressure side. Solid lines and dotted lines denote blowing and uniform suction at $Re_c = 200,000$ and $Re_c = 400,000$, respectively, and diamonds denote body-force damping at $Re_c = 200,000$. Color code for control configurations as in Table 2.1. The vertical dashed lines denote the control regions.

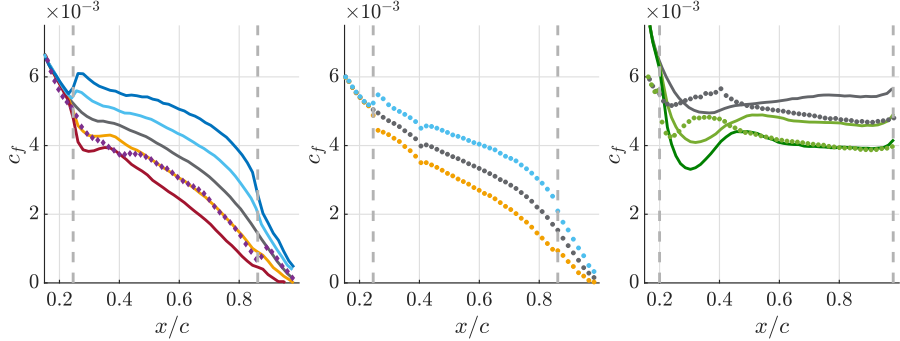


Figure 2.3: Local skin-friction coefficient as a function of the chord location, denoted by c_f and x/c , respectively, for (left) suction side for cases at $Re_c = 200,000$, (center) suction side for cases at $Re_c = 400,000$, and (right) pressure side. Solid lines and dotted lines denote blowing and uniform suction at $Re_c = 200,000$ and $Re_c = 400,000$, respectively, and diamonds denote body-force damping at $Re_c = 200,000$. Color code for control configurations as in Table 2.1. The vertical dashed lines denote the control regions.

and body-force damping reduce Re_θ , although body-force damping by a smaller amount.

Figure 2.3 shows the skin-friction coefficient defined in terms of the local edge velocity, $c_f = \tau_w / (\frac{1}{2} \rho U_e^2)$. On the suction side, the strong APG after the point of

maximum camber causes a rapid decrease in skin friction, almost leading to mean separation in the reference cases at both Reynolds numbers. On the pressure side, c_f exhibits two distinct trends, decreasing on the case at higher Re_c , but increasing on the case at lower Re_c . This fact is probably a consequence of the low Reynold number in R2REF and the weak favourable pressure gradient. Uniform blowing causes a further decrease, and its downstream effects are sufficient to lead to separation eventually in the case with stronger blowing intensity. Skin-friction reduction due to blowing is almost uniform in the control region on both suction and pressure sides, even though the reference c_f is decreasing for the suction side. Similarly, the skin-friction increase due to suction is also almost uniform so that the relative effects of both control strategies increases in the region of strong APG. Interestingly, body-force damping effects are more dependent on the streamwise location than those of uniform blowing. Body-force damping is implemented as a volume force in the wall-normal direction active below $y^+ = 20$, and its intensity is determined by a fixed coefficient calibrated to yield a certain skin-friction reduction. The results in Figure 2.3 (left) shows that the body-force efficiency, for the particular intensity considered in this simulation, is highest near $x/c = 0.4$, which is a location with relatively weak APG, suggesting that the pressure gradient can have a relevant impact on this model for opposition control.

The qualitative effects of uniform blowing on the streamwise development of the boundary layer on the suction side are similar to those of an even stronger adverse pressure gradient. Similarities between blowing and suction and pressure gradients are also apparent on the mean-velocity and Reynolds-stress profiles, as discussed later on.

2.1.2. Mean velocity and Reynolds stress

The inner-scaled wall-tangential component of the mean velocity (U_t^+) as a function of the inner-scaled wall-normal distance (y_n^+) is shown in Figure 2.4 for streamwise location $x/c = 0.75$ and all considered cases, together with that of a zero-pressure-gradient (ZPG) boundary layer at similar friction Reynolds number. On the suction side, U_t^+ in the uncontrolled cases exhibits higher values in the wake region than in the ZPG boundary layer, which is a distinct feature of APG boundary layers, and this profile is in relatively good agreement with the ZPG reference at a lower distance from the wall. Uniform blowing also leads to higher U_t^+ in the wake region, but it modifies the velocity profiles closer to the wall as well (Stevenson 1963). A similar phenomenon can be observed for the wall-normal mean-velocity component, V_n^+ (not shown here). Adverse pressure gradients cause higher wall-normal convection, which is further enhanced by uniform blowing (and reduced by suction). However, $V_n^+ \propto (y_n^+)^2$ at the wall in the absence of transpiration, while it is constant in the near-wall region in case of blowing or suction. Body-force damping has an even more substantial effect on mean velocity. In particular, U_t^+ is significantly higher than the reference in the buffer region and even higher than U_t^+ for the case of

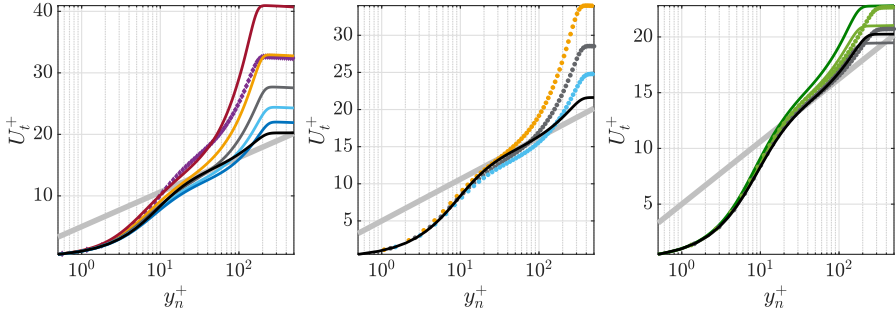


Figure 2.4: Inner-scaled mean velocity component in the wall-tangential direction as a function of the inner-scaled wall-normal distance, denoted by U_t^+ and y_n^+ , respectively, at $x/c = 0.75$ and for (left) suction side for cases at $Re_c = 200,000$, (center) suction side for cases at $Re_c = 400,000$, and (right) pressure side. Solid lines and dotted lines denote blowing and uniform suction at $Re_c = 200,000$ and $Re_c = 400,000$, respectively, and diamonds denote body-force damping at $Re_c = 200,000$. The colour code is as in Table 2.1, and the black lines denote ZPG TBL at similar friction Reynolds number (Eitel-Amor *et al.* 2014). The gray lines in the background denote $U_t^+ = 1/\kappa(\ln y_n^+ + C)$, with $\kappa = 0.41$ and $C = 2.05$.

blowing with similar skin-friction reduction. However, the wake velocity is the same in these two controlled cases.

Pressure gradient and control have also very evident effects on velocity fluctuations. The inner- and outer-scaled wall-tangential velocity fluctuations and Reynold-shear stress as functions of the inner-scaled wall-normal distance for all cases and the ZPG reference are shown in Figure 2.5. The inner-scaled velocity fluctuations have higher intensity in APG than in ZPG boundary layers, which is in part due to the lower friction velocity, and also a different distribution with respect to the distance from the wall. In particular, $\overline{u^2}^+$ exhibits a second maximum farther from the wall. In the reference case at $Re_c = 400,000$ and $x/c = 0.75$ (Figure 2.5, centre), for instance, the friction Reynolds number is $Re_\tau \approx 350$, the velocity fluctuation inner peak is located at $y_n^+ \approx 13$ and the outer peak is at $y_n^+ \approx 110$, and $\overline{u^2}^+$ is always higher than in the ZPG boundary layer. However, when the fluctuations are scaled in outer units, the inner peak of the wall-tangential velocity fluctuations becomes lower in the APG case than in the ZPG reference. This fact appears to suggest that the APG, through the strong wall-normal convection, redistributes structures towards the outer layer rather than energize turbulent fluctuations at all distances from the wall. The velocity fluctuations on the pressure side are in relatively good agreement with the ZPG dataset, showing only minor deviations due to the favourable pressure gradient.

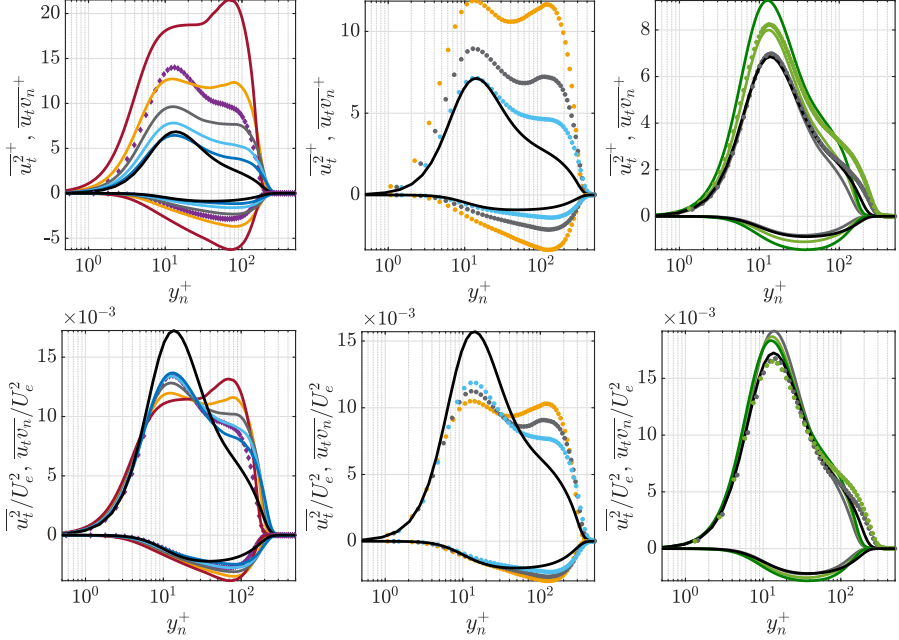


Figure 2.5: (Top) Inner-scaled and (bottom) outer-scaled fluctuations of the wall-tangential velocity component, denoted by $\overline{u^2}^+$ and $\overline{u^2}/U_e^2$, respectively, as functions of the inner-scaled wall-normal distance, denoted by y_n^+ , at $x/c = 0.75$ and for (left) suction side for cases at $Re_c = 200,000$, (center) suction side for cases at $Re_c = 400,000$, and (right) pressure side. Solid lines and dotted lines denote blowing and uniform suction at $Re_c = 200,000$ and $Re_c = 400,000$, respectively, and diamonds denote body-force damping at $Re_c = 200,000$. The colour code is as in Table 2.1, and the black lines denote ZPG TBL at similar friction Reynolds number (Eitel-Amor *et al.* 2014).

Blowing and suction modify the inner-scaled fluctuations $\overline{u^2}^+$ by increasing and decreasing them, respectively. Similarly to what was observed for the APG, blowing and suction effects on the outer-scaled fluctuations $\overline{u^2}/U_e^2$ are different for the inner and outer peaks. On the one hand, uniform blowing enhances wall-normal convection increasing the outer-peak intensity and decreasing that of the inner peak even further. Note that the effects of the stronger blowing at $Re_c = 200,000$ are sufficiently strong to make the outer peak larger than the inner peak. On the other hand, uniform suction reduces wall-normal convection, decreases the outer peak, and increases the inner peak of $\overline{u^2}/U_e^2$. An additional interesting phenomenon that is particularly evident for the velocity fluctuations is the blowing applied to the pressure side, at both Reynolds and intensities, has a less evident impact than on the suction side. This fact is particularly

apparent comparing the effects of the stronger blowing on suction and pressure sides at $Re_c = 200,000$.

The control effects on the velocity fluctuations show complex interactions between uniform blowing and suction and pressure gradients. In the next sections, we will examine the budget of turbulent kinetic energy and how the various described phenomena contribute to the change of skin friction.

2.1.3. Budget of the turbulent kinetic energy

Tanarro *et al.* (2020b) examined the turbulent-kinetic-energy (TKE) budget for the reference case at $Re_c = 400,000$, and they performed a comparison with the same quantities in a ZPG boundary layer at a similar Reynolds number. They observed that the TKE dissipation expressed in inner units is enhanced at all wall-normal locations, which is the result of higher production in the outer layer and higher viscous diffusion near the wall. However, similarly to what was observed for the wall-tangential velocity fluctuations, the outer-scaled profiles of TKE production in the inner layer and viscous diffusion close to the wall are lower in the APG boundary layer than in ZPG reference. Subsequently, the APG also exhibits lower outer-scaled dissipation in the inner layer, and only in the outer layer the outer-scaled production and dissipation are higher in the APG boundary layer than in the ZPG reference. The remaining three terms of the TKE budget, *i.e.* turbulent transport, velocity-pressure-gradient correlation and convection, are of relatively small intensity in this flow. The inner-scaled turbulent transport is more intense in APG than ZPG boundary layer, but the outer-scaled one is less intense. To the contrary, velocity-pressure-gradient correlation and convection are higher in APG than in ZPG in both inner and outer units. However, note that convection is negligible at most wall-normal distances, with the sole exception of the boundary-layer edge, where all the other terms are also very small.

We focus on the effects on the TKE budget of uniform blowing and suction for the cases at higher Reynolds number. We illustrate the inner and outer-scaled wall-normal profiles of each term of the TKE budget for Cases R4REF, R4BL1, and R4SC1 ($Re_c = 400,000$) at $x/c = 0.7$ in Figure 2.6. Uniform blowing and suction have effects qualitatively similar to those of pressure gradients for most terms and wall-normal distances, in particular in inner-scaled units. Almost all the terms in inner-scaled units are of higher intensity for uniform blowing and lower intensity for uniform suction, which is qualitatively similar to what was observed for APG and FPG, respectively. The only exception is convection near the wall ($y_n^+ < 10$), which is negative for uniform blowing but positive for uniform suction; however, its contribution to the total budget is almost negligible. Note that the modulus of the inner-scaled convection is slightly higher for blowing than for suction, a fact that is due to the different friction velocity.

The control effects on the outer-scaled profiles are less strong for this blowing and suction intensity than the pressure-gradient effects. In particular,

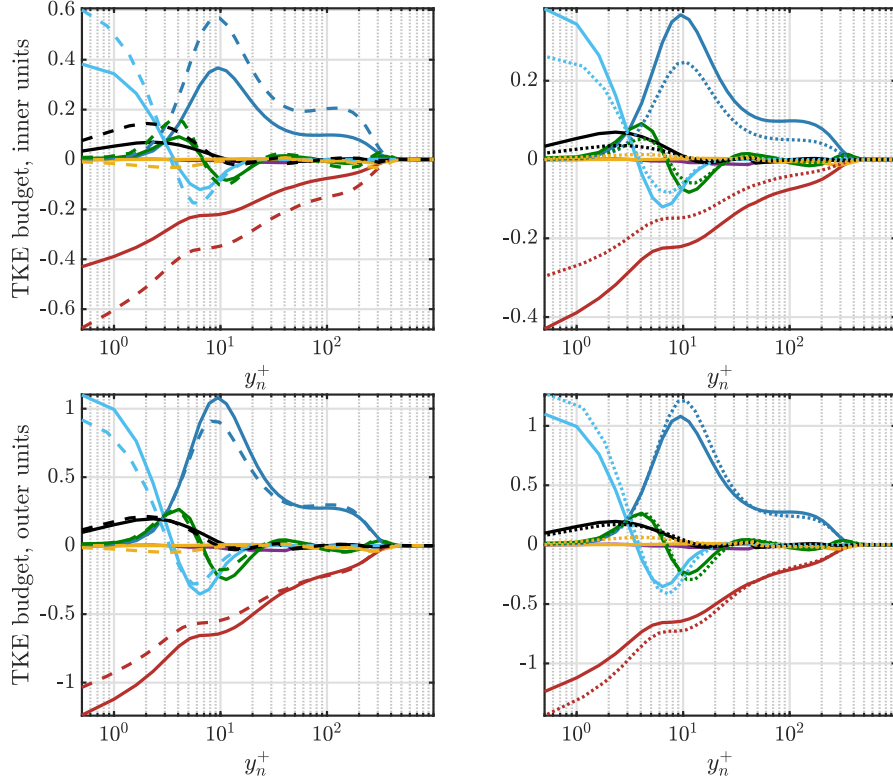


Figure 2.6: Turbulent kinetic energy budgets in (top) inner and (bottom) outer scaling, for the reference case at $Re_c = 400,000$ (Case G, solid lines); we show (left) uniform blowing and (right) uniform suction at the same Reynolds number (Case H, in dashed lines, and Case I, in dotted lines, respectively). The colour code for the various terms is as follows: production (■), dissipation (■), velocity-pressure-gradient correlation (■), turbulent transport (■), viscous diffusion (□), velocity-pressure-gradient correlation (□), and convection (□).

the outer-scaled production, viscous diffusion and dissipation in the inner layer are lower for uniform blowing and higher for uniform suction. Production and dissipation are slightly more intense in the outer layer, but the differences between the two cases with control and the reference are almost negligible. Similarly, the outer-scaled velocity-pressure-gradient correlations for the cases with control are in very good agreement with the reference, which is different than what was observed comparing APG and ZPG boundary layers. Lastly, the convection in the near-wall region has virtually the same intensity for uniform blowing and uniform suction, but opposite sign.

2.1.4. Skin-friction contributions

Even in the case of predetermined control such as uniform blowing or suction, to explain a specific change in skin friction in turbulent flows is still not obvious. A possible approach to investigate this problem is to try to separate how different processes concur to generating friction, which is the reason behind deriving identities that express the total friction as a sum of the distinct contributions. The so-called FIK identity (Fukagata *et al.* 2002) is one of such decompositions. It is derived by applying a triple integration by parts to the turbulent boundary layer equation that results in four main contributions:

$$c_f = c_f^\delta + c_f^T + c_f^D + c_f^P. \quad (2.1)$$

The first contribution, denoted by c_f^δ , is related to the boundary-layer thickness:

$$c_f^\delta = \frac{4(1 - \delta^*/\delta_{99})}{Re_\delta}, \quad (2.2)$$

where $Re_\delta = U_e \delta_{99} / \nu$. This contribution diminishes moving downstream toward the trailing edge. It is not negligible in the present cases at a relatively low Reynolds number (particularly on the airfoil pressure side), but it would not be relevant in most realistic applications. Uniform blowing and suction slightly increases and decreases c_f^δ , respectively, because of their effects on the boundary-layer thickness.

The second contribution, denoted by c_f^T and shown as a function of the streamwise location x/c in Figure 2.7, includes explicitly the Reynolds-shear stress:

$$c_f^T = -4 \int_0^1 (1 - \eta) \bar{u}_t v_n d\eta. \quad (2.3)$$

Note that the integration variable is the wall-normal distance normalized with the boundary-layer thickness, $\eta = y_n/\delta_{99}$. This contribution is higher in cases with more energetic turbulent fluctuations, and it increases significantly in the region of strong APG. Uniform blowing, which gives even higher velocity fluctuations, also increases c_f^T , while uniform suction and body-force damping reduce it.

The third contribution in the FIK identity, shown in Figure 2.8, is denoted by c_f^D and includes all the terms which would vanish in turbulent flows fully developed in the streamwise direction. It is sometimes written as:

$$c_f^D = -2 \int_0^1 (1 - \eta)^2 I_x d\eta, \quad (2.4)$$

where the term I_x includes mean-velocity and fluctuation derivatives in the wall-tangential direction, and wall-normal convection:

$$I_x = \frac{\partial U_t^2}{\partial x_t} + \frac{\partial \bar{u}_t^2}{\partial x_t} + \frac{\partial (U_t V_n)}{\partial \eta} - \frac{1}{Re_\delta} \frac{\partial^2 U_t}{\partial x_t^2}. \quad (2.5)$$

This contribution has very high values on the suction side and its streamwise evolution is a consequence of the equilibrium between the two terms including

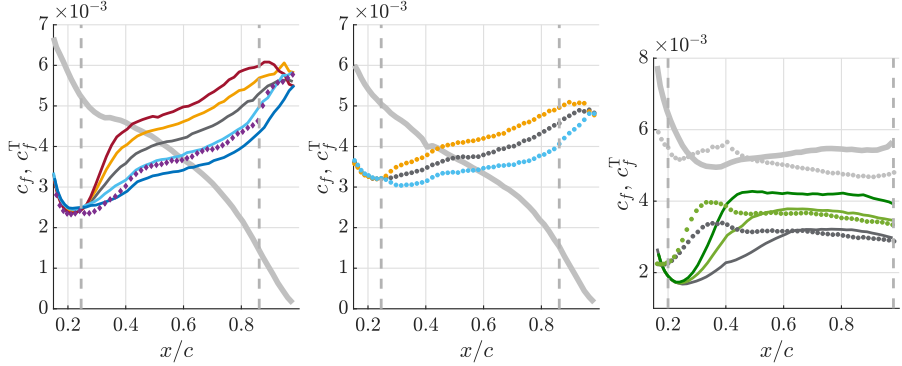


Figure 2.7: Turbulent-fluctuations contribution in the FIK decomposition (2.3) as a function of the chord location, denoted by c_f^T and x/c , respectively, for (left) suction side for cases at $Re_c = 200,000$, (center) suction side for cases at $Re_c = 400,000$, and (right) pressure side. Solid and dotted lines denote blowing and uniform suction at $Re_c = 200,000$ and $Re_c = 400,000$, respectively, whereas diamonds denote body-force damping at $Re_c = 200,000$. Color code for control configurations as in Table 2.1. The grey solid and dotted lines denote the total c_f of the reference cases. The vertical dashed lines denote the control regions.

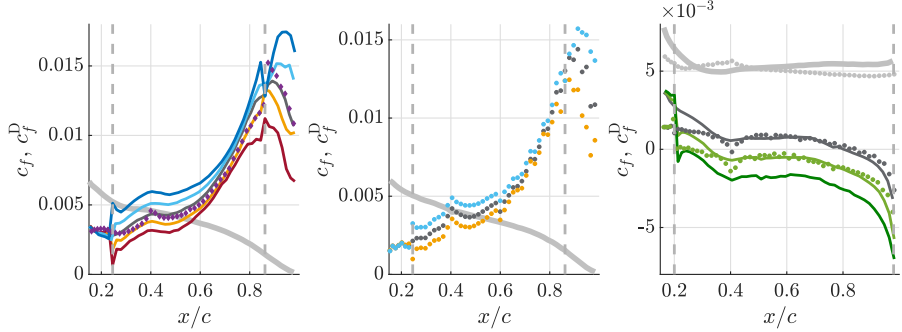


Figure 2.8: Development contribution in the FIK decomposition (2.4) as a function of the chord location, denoted by c_f^D and x/c , respectively, for (left) suction side for cases at $Re_c = 200,000$, (center) suction side for cases at $Re_c = 400,000$, and (right) pressure side. Solid and dotted lines denote blowing and uniform suction at $Re_c = 200,000$ and $Re_c = 400,000$, respectively, whereas diamonds denote body-force damping at $Re_c = 200,000$. Color code for control configurations as in Table 2.1. The grey solid and dotted lines denote the total c_f of the reference cases. The vertical dashed lines denote the control regions.

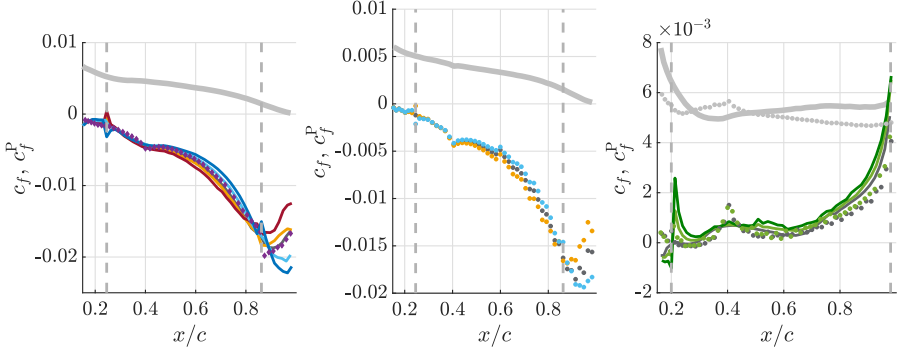


Figure 2.9: Pressure-gradient contribution in the FIK decomposition (2.6) as a function of the chord location, denoted by c_f^D and x/c , respectively, for (left) suction side for cases at $Re_c = 200,000$, (center) suction side for cases at $Re_c = 400,000$, and (right) pressure side. Solid and dotted lines denote blowing and uniform suction at $Re_c = 200,000$ and $Re_c = 400,000$, respectively, whereas diamonds denote body-force damping at $Re_c = 200,000$. Color code for control configurations as in Table 2.1. The grey solid and dotted lines denote the total c_f of the reference cases. The vertical dashed lines denote the control regions.

the wall-tangential and wall-normal mean-velocity components, $\partial U_t^2 / \partial x_t$ and $\partial(U_t V_n) / \partial \eta$. These terms have opposite signs and are significantly increased in absolute value by both APG and blowing, but with two different outcomes. The adverse pressure gradient increases the intensity of the positive term, $\partial U_t^2 / \partial x_t$, more than that of the negative term, $\partial(U_t V_n) / \partial \eta$, thus leading to a high c_f^D . Uniform blowing increases the intensity of $\partial(U_t V_n) / \partial \eta$ more than that of $\partial U_t^2 / \partial x_t$, resulting in a lower c_f^D than the in the uncontrolled case. Uniform suction, on the other hand, descrease the absolute value of both terms, but more so for the negative term $\partial(U_t V_n) / \partial \eta$, eventually resulting in a higher c_f^D than the in the reference.

The fourth contribution, denoted by c_f^P and shown in Figure 2.9 includes explicitly the pressure gradient:

$$c_f^P = -2 \int_0^1 (1 - \eta)^2 \frac{\partial P}{\partial x_t} d\eta. \quad (2.6)$$

This contribution is negative in the case of APG boundary layers, and it is the term of the FIK identity that explains the descrease of skin friction in these flows. It increases slightly in absolute value by blowing and reduced by suction. Because on the suction side c_f^P is negative, it contributes to skin-friction reduction for blowing and to skin-friction increase for suction, but on the pressure side c_f^P is positive, and thus increasing c_f .

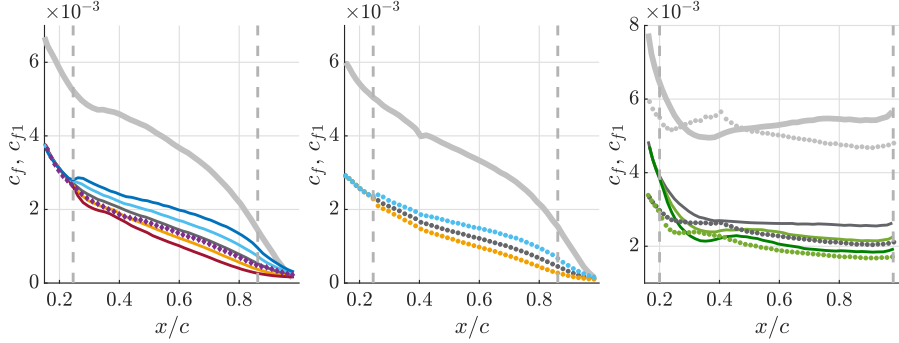


Figure 2.10: Viscous-dissipation contribution in the RD decomposition (2.8) as a function of the chord location, denoted by c_{f1} and x/c , respectively, for (left) suction side for cases at $Re_c = 200,000$, (center) suction side for cases at $Re_c = 400,000$, and (right) pressure side. Solid lines and dotted lines denote blowing and uniform suction at $Re_c = 200,000$ and $Re_c = 400,000$, respectively, and diamonds denote body-force damping at $Re_c = 200,000$. Color code for control configurations as in Table 2.1. The grey solid and dotted lines denote the total c_f of the reference cases. The vertical dashed lines denote the control regions.

Difficulties in the physical interpretation of the FIK identity motivated Renard & Deck (2016) to derive a new skin-friction decomposition based on the kinetic-energy budget. In the RD decomposition, the skin friction is expressed as a sum of three contributions:

$$c_f = c_{f1} + c_{f2} + c_{f3}. \quad (2.7)$$

The first term, shown in Figure 2.10, is related to viscous dissipation:

$$c_{f1} = \frac{2}{U_e^3} \int_0^{\delta_{99}} \nu \left(\frac{\partial U_t}{\partial y_n} \right)^2 dy_n. \quad (2.8)$$

Note that the RD decomposition is derived in a frame of reference where the wall is moving with the free-stream velocity, and the upper limit of the integration is the free-stream. The best generalization of this expression in the case of the boundary layer on an airfoil is not obvious, but a possible solution is to assume $U_\infty = U_e$ and δ_{99} as upper limit. Although this assumption is against the spirit of the RD decomposition, we verified that extending the integration farther from the wall does not have a significant impact for the qualitative discussion presented here. The contribution c_{f1} progressively decreases as Re increases moving toward the trailing edge, more rapidly on the suction side than on the pressure side because of the APG, and it is reduced by blowing and body-force damping, and increased by suction.

The second term of the RD decomposition, shown in Figure 2.11, is related

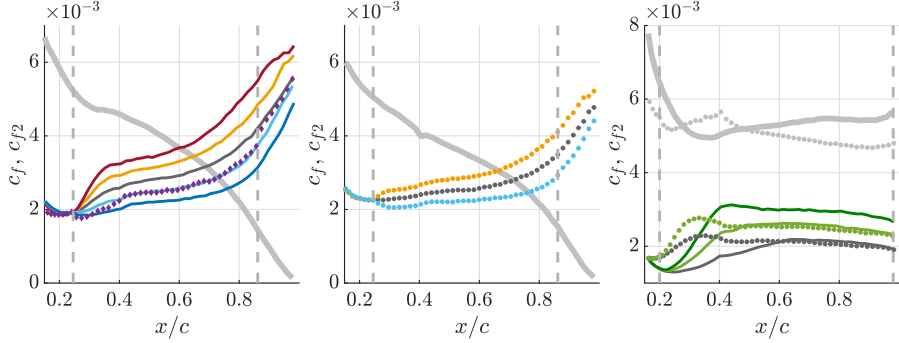


Figure 2.11: Turbulent-kinetic-energy contribution in the RD decomposition (2.9) as a function of the chord location, denoted by c_{f2} and x/c , respectively, for (left) suction side for cases at $Re_c = 200,000$, (center) suction side for cases at $Re_c = 400,000$, and (right) pressure side. Solid lines and dotted lines denote blowing and uniform suction at $Re_c = 200,000$ and $Re_c = 400,000$, respectively, and diamonds denote body-force damping at $Re_c = 200,000$. Color code for control configurations as in Table 2.1. The grey solid and dotted lines denote the total c_f of the reference cases. The vertical dashed lines denote the control regions.

to TKE production:

$$c_{f2} = \frac{2}{U_e^3} \int_0^{\delta_{99}} -\bar{uv} \frac{\partial U}{\partial y} dy. \quad (2.9)$$

This term is obviously similar to the turbulent-fluctuation contribution of the FIK identity, c_f^T (2.3), and it has a similar behaviour *i.e.* is significantly increased by the adverse pressure gradient and by uniform blowing, which enhances velocity fluctuations, and decreased by uniform suction and body-force damping. An interesting difference between c_f^T and c_{f2} is that the latter represents a lower fraction of the total skin friction where the adverse pressure gradient is relatively weak, but it also increases more sharply in the last portion of the airfoil, where the adverse pressure gradient is very strong. This result is perhaps because even though APGs generally yield more intense fluctuations, only at very high β the TKE production increases significantly in the outer region.

The third term, shown in Figure 2.12, is related to the boundary-layer development:

$$c_{f3} = \frac{2}{U_e^3} \int_0^{\delta_{99}} (U - U_e) \frac{\partial \tau}{\partial y} dy. \quad (2.10)$$

Note that $\tau = \nu(\partial U_t / \partial y_n) - \bar{u}_t \bar{v}_n$ denotes the total shear stress. This term can be expanded to show that it includes mean convection, streamwise development, and the pressure gradient, and it is thus equivalent to the combined development

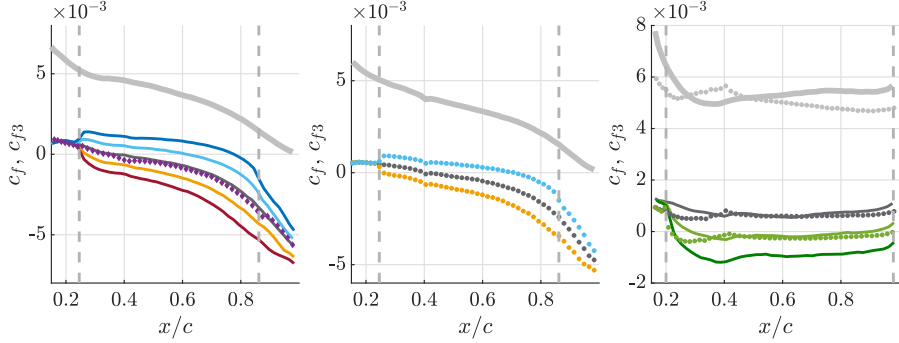


Figure 2.12: Development contribution in the RD decomposition (2.9) as a function of the chord location, denoted by c_{f3} and x/c , respectively, for (left) suction side for cases at $Re_c = 200,000$, (center) suction side for cases at $Re_c = 400,000$, and (right) pressure side. Solid lines and dotted lines denote blowing and uniform suction at $Re_c = 200,000$ and $Re_c = 400,000$, respectively, and diamonds denote body-force damping at $Re_c = 200,000$. Color code for control configurations as in Table 2.1. The grey solid and dotted lines denote the total c_f of the reference cases. The vertical dashed lines denote the control regions.

and pressure contributions in the FIK identity. The strong adverse pressure gradient on the suction side and uniform blowing reduce c_{f3} , while uniform suction increases it.

A more detailed analysis of the FIK and RD contributions is presented in **Papers 4, 5, & 6**, focusing on a specific streamwise location and also examining the wall-normal profiles of the integrands of the most relevant terms.

2.2. Aerodynamic properties

The objective of applying control strategies on wing profiles is ultimately to improve the lift-to-drag ratio, denoted by L/D . Lift and drag in airfoils are measured using the lift (C_l) and (C_d) drag coefficients, which are the lift and drag forces per unit area normalized with the dynamic pressure of the incoming flow, respectively:

$$\begin{aligned} C_l &= \frac{F_l}{qA} = \frac{2}{\rho U_\infty^2 A} \int_A \tau_w(\hat{t} \cdot \hat{k}) dA + \frac{2}{\rho U_\infty^2 A} \int_A (p - p_0)(\hat{n} \cdot \hat{k}) dA \\ C_d &= \frac{F_d}{qA} = \underbrace{\frac{2}{\rho U_\infty^2 A} \int_A \tau_w(\hat{t} \cdot \hat{i}) dA}_{C_{d,f}} + \underbrace{\frac{2}{\rho U_\infty^2 A} \int_A (p - p_0)(\hat{n} \cdot \hat{i}) dA}_{C_{d,p}} . \end{aligned} \quad (2.11)$$

In these expressions, A is the airfoil surface, $q = \frac{1}{2}\rho U_\infty^2$ is the dynamic pressure of the free stream, and F_l , F_d are the components of the total force applied to

Table 2.2: Integrated lift (C_l), integrated skin-friction ($C_{d,f}$) and pressure ($C_{d,p}$) contributions to the total drag (C_d), and the aerodynamic efficiency (L/D) for the cases considered in this chapter. The values in parenthesis are the relative change with respect to the reference.

Case	C_l	$C_{d,f}$	$C_{d,p}$	$C_d = C_{d,f} + C_{d,p}$	L/D
$Re_c = 200,000$					
R2REF	0.867	0.0128	0.0087	0.0215	41
R2BL1	0.833 (-4%)	0.0122 (-4%)	0.0099 (+14%)	0.0221 (+3%)	38 (-7%)
R2BL2	0.796 (-8%)	0.0117 (-8%)	0.0113 (+31%)	0.0231 (+8%)	34 (-15%)
R2SC1	0.898 (+4%)	0.0133 (+4%)	0.0076 (-12%)	0.0210 (-2%)	43 (+6%)
R2SC2	0.925 (+7%)	0.0140 (+10%)	0.0066 (-24%)	0.0206 (-4%)	45 (+11%)
R2BD1	0.879 (+1%)	0.0121 (-5%)	0.0083 (-4%)	0.0204 (-4%)	43 (+6%)
R2PB1	0.871 (+0%)	0.0123 (-4%)	0.0084 (-3%)	0.0207 (-3%)	42 (+4%)
R2PB2	0.880 (+1%)	0.0119 (-7%)	0.0084 (-3%)	0.0203 (-5%)	43 (+6%)
$Re_c = 400,000$					
R4REF	0.894	0.0109	0.0066	0.0175	51
R4BL1	0.854 (-4%)	0.0103 (-5%)	0.0080 (+21%)	0.0183 (+5%)	47 (-9%)
R4SC1	0.924 (+3%)	0.0115 (+6%)	0.0058 (-12%)	0.0173 (-1%)	53 (+4%)
R4PB1	0.899 (+0%)	0.0104 (-5%)	0.0066 (-0%)	0.0169 (-3%)	53 (+4%)

the airfoil in the perpendicular and parallel directions to the airfoil trajectory, respectively. Note that τ_w is the shear stress at the wall, p_0 is the reference pressures, and \hat{t} , \hat{n} , \hat{k} , and \hat{i} are the unit vectors in the directions parallel to airfoil surface, perpendicular to the airfoil surface, parallel to the airfoil trajectory and perpendicular to the airfoil trajectory, respectively. On the one hand, the lift force is predominantly due to pressure. On the other hand, the skin-friction contribution to drag, denoted hereafter by $C_{d,f}$, is the most relevant, but the pressure contribution, denoted by $C_{d,p}$, can be not negligible. Furthermore, C_d decreases if the Reynolds number Re_c increases, and $C_{d,p}$ decreases faster than $C_{d,f}$ as the boundary layer becomes thinner (assuming that transition to turbulence occurs at a constant location).

2.2.1. Control effects in LES

The control effects on L/D are determined by the modifications of the three different terms C_l , $C_{d,f}$, and $C_{d,p}$, as shown in Table 2.2 for the LES considered cases so far. Uniform blowing and uniform suction applied on the suction side modify both pressure and skin-friction contributions to drag substantially. Uniform blowing, which increases the boundary-layer thickness, increases the pressure drag, while uniform suction, decreasing the boundary-layer thickness, reduces the pressure drag. At these moderate Reynolds numbers, both blowing and suction effects on the suction side are relatively stronger on $C_{d,p}$ than on $C_{d,f}$, and the pressure drag is high enough that blowing causes higher total drag, while suction causes lower total drag. At the same time, uniform blowing on the

suction side results in lower C_l and uniform suction in higher C_l and, eventually, blowing gives lower L/D , and suction higher L/D , both at $Re_c = 200,000$ and $400,000$. Interestingly, uniform blowing applied on the pressure side reduces drag but, despite the fact that it increases the boundary-layer thickness, it still results in lower pressure drag and lower total drag (this effect is discussed in **Paper 4**). In addition, it also increases C_l and hence the lift-to-drag ratio. Body-force damping reduces both skin friction and pressure contributions to drag, increasing L/D as well. A discussion of the statistical significance of these results is presented in **Paper 3**.

Reynolds-number effects are not in the same direction for blowing and suction applied on the suction side. In particular, although the pressure drag decreases from 40% of the total drag at $Re_c = 200,000$ to 38% at $Re_c = 400,000$, its relative change increases due to blowing. This phenomenon causes uniform blowing on the suction side to reduce the lift-to-drag ratio even more at $Re_c = 400,000$ than at $Re_c = 200,000$. Uniform-suction relative effects on $C_{d,p}$ and $C_{d,f}$, however, are similar at both Reynolds numbers, which leads to a lower impact on drag at $Re_c = 400,000$ than at $Re_c = 200,000$ as $C_{d,p}$ becomes less important. Uniform blowing applied to the pressure side is less sensitive to the Reynolds number (at least in this range of Re_c).

2.2.2. RANS and Reynolds-number effects

It is not feasible to use high-fidelity numerical simulations to extend the range of Reynolds numbers. Therefore a comprehensive parameter study was conducted with RANS simulations, using a standard formulation of $k-\omega$ – SST model (Menter 1993) (more details are provided in **Paper 4**). Direct comparisons between the well-resolved LESs described so far and these RANS simulations are difficult because of the inevitable differences between the two setups. In particular, RANS simulations require boundary conditions for quantities such as turbulent kinetic energy (k) and specific dissipation rate (ω), and transition to turbulent has to be induced by introducing a source term for k . In addition, RANS can take advantage of a much larger domain, where free-stream inflow conditions can be directly applied. We found that the discrepancies of lift and drag in the uncontrolled cases between both methodologies are relatively high and of the order of magnitude of control effects, but control effects themselves are in better agreement. For instance, at $Re_c = 400,000$, the difference in total drag between the reference cases is $\approx 3\%$. However, uniform blowing with intensity 0.1% of U_∞ applied to the suction side changes C_d by +5% and +4% in LES and RANS, respectively. This fact suggests that RANS can be employed to discuss the general trends.

Figure 2.13 shows $C_{d,f}$, $C_{d,p}$, and the total C_d for uniform blowing and suction applied to the suction side for Reynolds numbers between $Re_c = 200,000$ and $4,000,000$. The trends identified with LESs at lower Re_c are also observed in this dataset. Uniform blowing and suction have opposite effects on pressure and skin-friction drag components, qualitatively. However, the increase in pressure

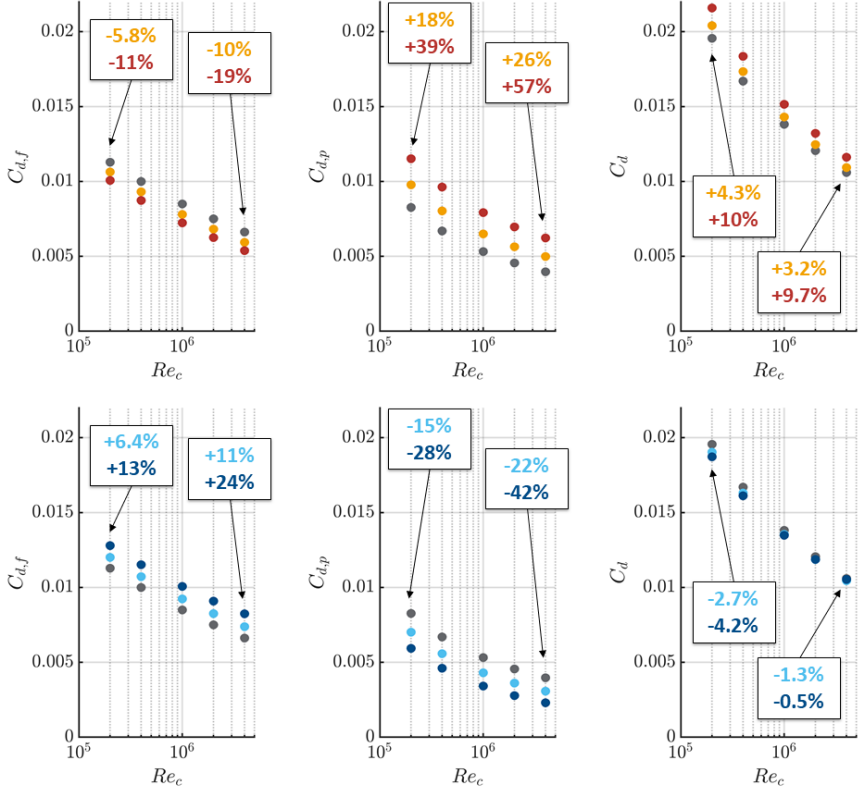


Figure 2.13: Control effects on the suctions side in RANS simulations. (Left) Integrated skin-friction ($C_{d,f}$), (centre) pressure drag ($C_{d,p}$), and (right) total drag (C_d) as functions of the chord Reynolds number, denoted by Re_c , for (top) uniform suction and (bottom) uniform blowing. The lighter and darker colors denote intensities $0.1\%U_\infty$ and $0.2\%U_\infty$, respectively.

drag due to blowing is higher than the corresponding decrease due to suction. At the same time, the increase in skin-friction drag due to suction is higher than the corresponding decrease due to blowing. These facts, and the equilibrium between $C_{d,p}$ and $C_{d,f}$, lead to the unfortunate results that drag reduction due to suction becomes less relevant quite rapidly as Re_c increases, while drag increase due to blowing is more persistent. For instance, uniform suction with intensity $0.1\%U_\infty$ yields $-2.5\%C_d$ at $Re_c = 200,000$ but $-1.3\%C_d$ at $Re_c = 4,000,000$. Uniform blowing the same intensity gives $+4.3\%C_d$ at $Re_c = 200,000$ and $+3.2\%C_d$ at $Re_c = 4,00,000$. A second relevant difference between uniform blowing and uniform suction is the varying effectiveness for increasing actuation intensity. On the one hand, at $Re_c = 4,000,000$, increasing blowing intensity

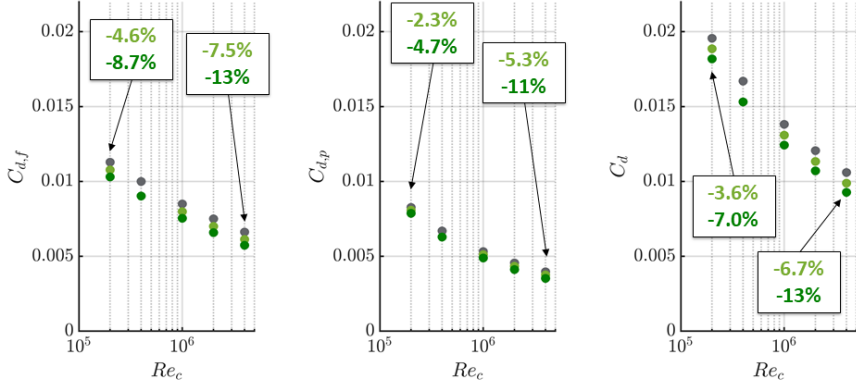


Figure 2.14: Effects of uniform blowing applied to the pressure side in RANS simulations. (Left) Integrated skin-friction ($C_{d,f}$), (centre) pressure drag ($C_{d,p}$), and (right) total drag (C_d) as functions of the chord Reynolds number, denoted by Re_c . The lighter and darker colors denote intensities $0.1\%U_\infty$ and $0.2\%U_\infty$, respectively.

amplifies the pressure-drag increase more than the skin-friction reduction, so that $0.2\%U_\infty$ blowing gives $+9.7\%C_d$. On the other hand, increasing suction intensity amplifies the skin-friction increase more than the pressure drag reduction, and $0.2\%U_\infty$ suction gives only $-0.5\%C_d$ at $Re_c = 4,000,000$.

Uniform blowing applied to the pressure side exhibits trends that are more encouraging for industrial applications, as shown in Figure 2.14. In particular, skin-friction and pressure contributions to drag are always decreased, and the relative effect of the control increases at a higher Reynolds number. For instance, blowing with intensity $0.1\%U_\infty$ gives $-3.5\%C_d$ at $Re_c = 200,000$ and $-6.7\%C_d$ at $Re_c = 4,000,000$.

A very significant yet difficult question to address is whether a theoretical lift-to-drag increase also corresponds to net energy savings. In **Paper 4**, the same approach as that proposed by Beck *et al.* (2018) is used to estimate the actuation cost, considering a pump efficiency compatible with an external air supply. Our results indicate that uniform blowing applied over the pressure side can realistically be used to obtain energy savings. The actual practicality and convenience of further developing this control in a realistic scenario depend on technical considerations which are beyond the scope of the present project.

CHAPTER 3

Coherent structures

All incompressible turbulent flows have the same governing equations in common and thus share general properties, such as large-scale separation depending on the Reynold number and energy transfer between production and dissipation scales. However, they also exhibit a wide range of distinct phenomena due to geometrical constraints and distinct symmetry properties in different flows. We focused on the study of intense Reynolds-stress events in square and rectangular ducts, as well as APG turbulent boundary layers to describe how these structures are related to mean-flow properties. Intense Reynolds-stress events are defined as connected regions in the domain where the instantaneous velocity fluctuations are higher than a threshold based on the value of the root-mean-square of the considered velocity components (the connected regions are defined through a six-point connectivity stencil). This approach was introduced as a three-dimensional extension of the classic quadrant analysis (Wallace *et al.* 1972) by Lozano-Durán *et al.* (2012), who studied intense events of tangential Reynolds stress (\bar{uv}) in turbulent channel flows. The same method can also be applied to intense events for all the off-diagonal components of the Reynolds-stress tensor, defined according to the conditions:

$$|uv| > H_{uv} u_{\text{rms}} v_{\text{rms}}, \quad |uw| > H_{uw} u_{\text{rms}} w_{\text{rms}} \quad \text{and} \quad |vw| > H_{vw} v_{\text{rms}} w_{\text{rms}}. \quad (3.1)$$

The actual thresholds H_{XX} (called “hyperbolic hole”, referring to the hyperbola $uv = H_{uv}$ in the uv plane) are scalar values, while the normalisation terms $u_{\text{rms}} v_{\text{rms}}$, $u_{\text{rms}} w_{\text{rms}}$ and $v_{\text{rms}} w_{\text{rms}}$ are one-dimensional profiles for the channel and two-dimensional fields for the duct and the airfoil. Note that the normalization terms are chosen in order to detect the coherent structures homogeneously at the various wall-normal distances. A similar procedure was adopted by Nagaosa & Handler (2003), while studying vortex clusters with the Q criterion (Hunt *et al.* 1988), and by del Álamo *et al.* (2006), who used a similar threshold for the discriminant criterion (Chong *et al.* 1990). (Moisy & Jiménez 2004) introduced the percolation analysis in their study of vortical and dissipative coherent structures in homogeneous isotropic turbulence, and Lozano-Durán *et al.* (2012) employed it to qualitatively assess the effectiveness of the threshold. In the percolation analysis the ratio between the volume of the largest structure, \mathcal{V}_{\max} , and the total volume occupied by all the structures, \mathcal{V}_{all} , is computed for

different values of H . For low values of H most of the domain is occupied by few large objects and $\mathcal{V}_{\max}/\mathcal{V}_{\text{all}} \approx 1$, while for large enough values of H only few and more isolated points fulfil the condition, therefore $\mathcal{V}_{\max}/\mathcal{V}_{\text{all}} \ll 1$. The fact that the percolation crisis occurs, *i.e.* there is a relatively sharp transition between $\mathcal{V}_{\max}/\mathcal{V}_{\text{all}} \approx 1$ and $\mathcal{V}_{\max}/\mathcal{V}_{\text{all}} \ll 1$, is an evidence that the threshold properly captures the non-homogeneity of the flow.

It is worth mentioning that a percolation crisis can appear in many systems with a high number of degrees of freedom and certain connectivity and statistical properties, regardless of the underlying physical processes (Stauffer & Aharony 1994). In fluid mechanics, percolation theory has been used to study laminar-to-turbulent transition, *e.g.* by Lemoult *et al.* (2016), which is not to be confused with its use for structure identification. In the context of transition to turbulence, the order parameter that determines the occurrence of a percolation crisis is typically the Reynolds number. In the context of structure identification, the percolation analysis is a tool to assess whether the scalar field used in the identification process is sufficiently homogenous (as shown in **Paper 8**). In **Paper 12**, we discuss how the statistical properties of a scalar field are related to the percolation crisis.

3.1. Intense events in turbulent ducts

In **Papers 9 & 10**, we study the properties of intense Reynolds-stress events in square and rectangular ducts, performing a comparison with the same structures in channel flows at similar Reynolds numbers and focusing on possible connections with the secondary flow of Prandtl's second kind. In the present section, we describe the results for the square ducts at friction Reynolds numbers $Re_\tau = 180$ and $Re_\tau = 360$ (Re_τ denotes the value at the center plane). In fact, the analyses presented here are to some extent more detailed than those in **Papers 9 & 10**, and they serve to illustrate the complexity of this topic. Note that the material in the present section is a partial reproduction of <https://arxiv.org/pdf/1906.00886.pdf>, which has not appeared in the peer-reviewed literature.

The following notation is adopted for the duct: U denotes the streamwise mean velocity component, V the vertical component and W the spanwise component, for both channel and duct. The mean is defined as an average over time and the homogeneous directions (streamwise for the duct, streamwise and spanwise for the channel). The instantaneous fluctuations with respect of the mean are denoted with lower-case variables, the components of the Reynolds-stress tensor with $\bar{u}_i u_j$, whereas root-mean-squared values and ensemble averages over the fields are indicated explicitly as ξ_{rms} and ξ_{ens} , respectively. Note that the differences between time and ensemble average are due only to statistical uncertainty, *e.g.* $U = U_{\text{ens}}$, for a number of samples large enough and time average long enough. In the duct the origin of the reference frame is located at the bottom-left corner for an observer looking toward the streamwise direction, so that the two vertical walls are at $z = 0$ and $z = 2h$ and the two horizontal

Case	Re_b	Re_τ	Δx^+	Δy^+	Δz^+	No. fields
D. 180	2500	178	(1.98, 9.80)	(0.09, 4.74)	(0.09, 4.74)	879
D. 360	5693	356	(1.99, 9.88)	(0.15, 4.65)	(0.15, 4.65)	404
C. 180	3250	186	9.1	(0.10, 6.1)	4.5	76
C. 360	6739	354	8.7	(0.05, 5.8)	4.3	37

Table 3.1: Simulation parameters for the considered cases. The resolution is indicated in terms of the maximum and minimum grid spacing in inner units.

walls at $y = 0$ and $y = 2h$. Unless stated otherwise, outer scaling is employed, *i.e.* the velocity components are scaled with the bulk velocity and the spatial coordinates with the half-height of the duct/channel.

The data-set for the square duct is part of the data-set described by Vinuesa *et al.* (2014, 2018), and the resolutions as well as the number of fields employed for these cases are reported in Table 3.1. The length of the computational domain is $L_x = 25$ for the duct and the size in the streamwise and spanwise directions for the channel are, respectively, $L_x = 12\pi$ and $L_z = 4\pi$ for $Re_\tau = 180$ and $L_x = 8\pi$ and $L_z = 3\pi$ for $Re_\tau = 360$.

3.1.1. Scaling properties of the secondary flow

Turbulent ducts are characterized by the secondary flow of Prandtl's second kind, which leads to non-vanishing mean velocity on the plane perpendicular to the streamwise direction. The recent DNSs performed by Pirozzoli *et al.* (2018); Gavrilakis (2019) showed that, above a certain transitional friction Reynolds number $Re_\tau \approx 300$, the secondary flow in the square duct exhibits two different scaling in the corner and centre regions. If the cross-stream velocity components are scaled with the bulk velocity, the profiles are in good agreement in the corner region when the distance from the wall is expressed in viscous units, and in the centre region when the distance from the wall is scaled with the duct height. Figure 3.1 shows the vertical component of the mean velocity for $Re_\tau = 180$ and $Re_\tau = 360$. Note that $Re_\tau = 180$ is low enough to still observe Reynolds-number effects in the comparison between these two cases. In the lower-left quadrant of the duct at $Re_\tau = 180$, V exhibits one local maximum located at $(y^+ = 76; z^+ = 11)$, followed by a local minimum at $(y^+ = 49; z^+ = 49)$ and a second local maximum at $(y^+ = 35; z^+ = 125)$, which implies that a saddle point is located along the centre-line of the cross section. For $Re_\tau = 360$ the same three local extrema are observed at approximately the same inner-scaled locations: (78; 11), (50; 50) and (22; 118), respectively. Furthermore, a new local maximum appears along the centre-line and the saddle point migrates to an intermediate position between the third and the forth local maxima. The matching between V at the two different Reynolds numbers in the corner region is not valid for all y^+ , which is expected because points such as $(y^+ = 150, z^+ = 11)$ in the duct at $Re_\tau = 180$ belong to the region where

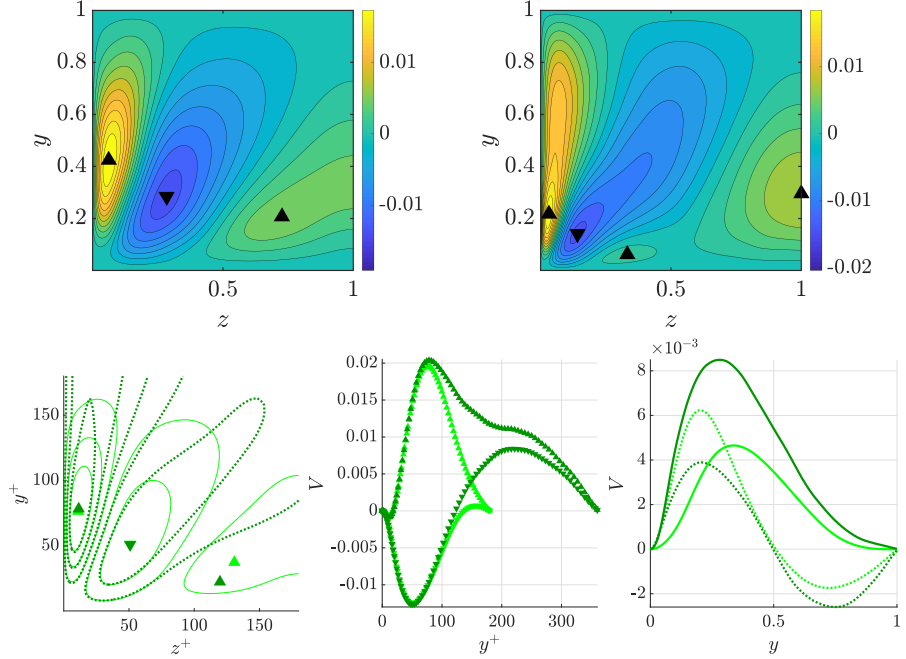


Figure 3.1: Top row: mean of the vertical component of the velocity V for one quadrant of the duct at (left) $Re_\tau = 180$ and (right) $Re_\tau = 360$. Local maxima and local minima are indicated with \blacktriangle and \blacktriangledown , respectively. Bottom row: scaling properties of V . Dark green and light green for $Re_\tau = 360$ and $Re_\tau = 180$, respectively. (Left) Contour and locations of maxima and minima coordinates scaled in inner-units. (Middle) Vertical profile of V as function of the inner-scaled vertical coordinate for the first maximum (\blacktriangle , $z^+ \approx 11$) and minimum (\blacktriangledown , $z^+ \approx 50$) and (right) as function of the outer-scaled vertical coordinate for the second maximum (dotted line, $z^+ \approx 120$) and third maximum for $Re_\tau = 360$ (solid line, $z = 1$).

the centre circulation takes place, *i.e.* the outer-scaling region of the domain. Nevertheless, the inner scaling remains valid far above the bisector, *e.g.*: up to $y^+ \approx 50$ for $z^+ = 11$ and up to $y^+ \approx 100$ for $z^+ = 50$.

The profiles corresponding to the location of the third maximum do not exhibit a clear scaling, neither in inner or in outer units. In fact, if scaled in outer units, the velocity profile for $Re_\tau = 180$ at the position of the second maximum overlaps with that at the centre-plane for $Re_\tau = 360$ only in a region near the wall, and it is close to the that of the second maximum for $Re_\tau = 360$ farther from the wall. The profile at the centre-plane of the profiles in the duct at $Re_\tau = 180$ does not match with any of the profiles in duct at $Re_\tau = 360$.

Given the properties of the V field that we have just discussed, we examined in detail the contributions of the coherent structures to the secondary flow at two spanwise locations: the local minimum of V and the centre-plane (*i.e.* $z^+ \simeq 11$ and $z = h$, respectively). The first choice is motivated by the fact that for this profile there is good agreement between the two Reynolds numbers if V is scaled in outer units and the wall-normal coordinate in inner units. The latter because the behaviour for $Re_\tau = 360$ at that spanwise location is similar to the one observed by Pirozzoli *et al.* (2018) for the same location at higher Reynolds numbers and because the centre-plane of the duct has in common with the channel flow that $W = 0$.

3.1.2. Structure identification

The effect of increasing the scalar threshold is illustrated in Figure 3.2 (top left) for uv events in square duct at $Re_\tau = 180$, which shows the contours of the identified structures for $H_{uv} = 0.5, 2$ and 4 . Note that in order to estimate the structure volume, denoted by \mathcal{V} , we assigned to each grid-point in the computational domain a characteristic volume based on the local grid spacing, and the volume of each structure is estimated as the sum of the characteristic volume of the grid points which belong to it. In the cases considered here the percolation analysis unveiled that the conditions (3.1) are not fully appropriate when applied to the entire domain, since the normalisation factors become negligible near the wall. Subsequently, a correction was introduced by excluding from the connectivity the region of the domain below $y^+ = 1$, computed with τ_w at the centre-plane. The wall distance $y^+ = 1$ was chosen for the correction because applying it in a wider region of the domain gives no appreciable differences in the results of the percolation analysis.

The percolation diagram is shown in Figure 3.2 (top right) for all the cases and the considered structures, together with the probability for uv events detected for different values of H_{uv} , in all the cases considered here (middle and right panels, respectively). The percolation diagrams of uv and vw events are very similar in channel and in duct flow. However, they are different from that of uw in the channel, while they are almost indistinguishable for uv and uw in the duct, as it is implied by the symmetry of the case. Small differences can be observed between the two different Reynolds numbers and in general between channel and duct. In particular, the percolation crisis is less evident for the duct at $Re_\tau = 180$ and in both Reynolds numbers is more sharp in the channel than in the duct.

At the present state, it is not possible to discriminate whether such discrepancy is due to structural differences in both flows or rather to the different shape of the domain. In this section, we focus on characterising the behaviour of the detected structures for a certain range of H_{XX} and we do not optimise the threshold. The percolation crisis always occurs at a value of H between 1.0 and 1.5 , and we observe that there are qualitative differences between the region of the domain sampled before and after the percolation crisis. In the first case,

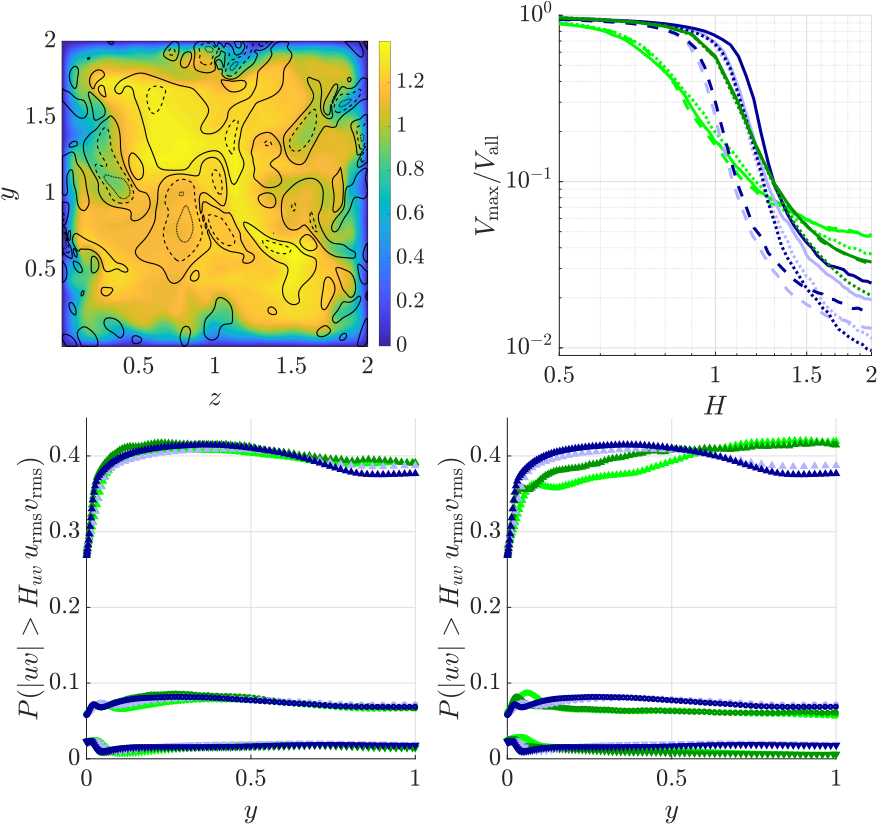


Figure 3.2: Top row: (left) slice orthogonal to the streamwise direction for duct flow at $Re_\tau = 180$, coloured with the instantaneous streamwise component of the velocity. The black solid, dashed and dotted lines represent the boundaries of intense uv events sampled for $H_{uv} = 0.5, 2.0$ and 4.0 , respectively. (Right) Percolation diagram for: uv (solid lines), uw (dashed lines) and vw (dotted lines). Channel in blue, duct in green and dark and light colour for $Re_\tau = 360$ and $Re_\tau = 180$, respectively. Bottom row: probability of detection for uv as a function of the distance from the wall for: $H_{uv} = 0.5$ (\blacktriangle), $H_{uv} = 2.0$ (\bullet) and $H_{uv} = 4.0$ (\blacktriangledown). Channel compared with (left) the centre-plane ($z = 1$) and (right) a near-corner vertical profile ($z = 0.1$) of the duct. Colours as for the top row.

\mathcal{V}_{all} can be a relatively small fraction of the domain, *e.g.* $\approx 40\%$ for $H_{uv} = 0.5$, but despite this fact it is not possible to clearly identify the most intense events because they are incorporated into very large structures. To the contrary, in the second case, for which \mathcal{V}_{all} is even smaller, *e.g.* $\approx 7\%$ for $H_{uv} = 2$, the

intense events are isolated, since a further increase of $H_{uv} = 2$ implies mostly a reduction of the volume for each event, rather than their splitting.

The probability of belonging to a detected structure is in very good agreement between channel and duct at the centre-plane at both the Reynolds numbers and for all the values of H_{uv} in the range considered. Its dependence on the wall-normal distance is weak, with the exception of the near-wall region ($y^+ < 15$), where very strong fluctuations are less likely. For the duct, it is also important to assess how the probability of detection differs at different spanwise locations. At $z = 0.1$ ($z^+ = 18$ and $z^+ = 36$ for $Re_\tau = 180$ and $Re_\tau = 360$, respectively) the proximity of the vertical wall affects the probability of detection. However, the discrepancy between this region of the domain and the core region is less important for values of H_{uv} higher than the one at which the percolation crisis occur. Similar results are obtained for uw and vw events, not shown here. These observations confirm that the normalisation factors are adequate and therefore it is possible to compare the coherent structures in the various cases.

3.1.3. Contributions to the secondary flow: core region

In the following we define $\Xi_{XX}^>$ as the fractional contribution to the variable Ξ sampled of over events XX detected according to conditions (3.1) and $\Xi_{XX}^<$ the fractional contribution over the portion of the domain which does not fulfil the same condition. The fractional contributions are computed as ensemble averages and weighted with the sampled volume fraction, so that their sum recovers the ensemble average over the entire data-set, *i.e.* $\Xi_{ens} = \Xi_{XX}^> + \Xi_{XX}^<$. For example, $U_{uv}^>$ is the mean streamwise velocity conditioned to the presence of strong uv and weighted by the corresponding volume fraction and $U_{uv}^<$ is the mean streamwise velocity averaged over the complementary part of the domain. These can be expressed mathematically as:

$$U_{uv}^> = \frac{\mathcal{V}_{uv}}{\mathcal{V}} \int U \delta_{uv} d\mathcal{V} \quad \text{and} \quad U_{uv}^< = \frac{\mathcal{V} - \mathcal{V}_{uv}}{\mathcal{V}} \int U (1 - \delta_{uv}) d\mathcal{V}, \quad (3.2)$$

where \mathcal{V} is the volume of the entire domain, \mathcal{V}_{uv} is the volume occupied by intense uv events (for a certain value of H_{uv}) and δ_{uv} is 1 if $|uv| > H_{uv} u_{rms} v_{rms}$ and 0 elsewhere. It is important to note that $\Xi_{XX}^>$ reflects both the intensity of the fluctuations and their probability of occurrence. For example, $|\Xi_{XX}^>|$ can be higher for $H_{XX} = 2.0$ than for $H_{XX} = 4.0$ in a certain region, because a higher threshold H_{XX} corresponds to stronger fluctuations, but at the same time to a smaller portion of the domain.

The scope of the decomposition $\Xi_{ens} = \Xi_{XX}^> + \Xi_{XX}^<$ is two-fold: on the one hand, it allows to investigate how more and less intense events contribute to the realisation of Ξ_{ens} ; on the other hand, given that the probability of detection is in good agreement for a certain H_{XX} , it allows a direct comparison between intense and weak events in the different cases.

We firstly compare the core region of the duct and the channel. Figure 3.3 shows the contribution of intense uv events to the vertical component of the

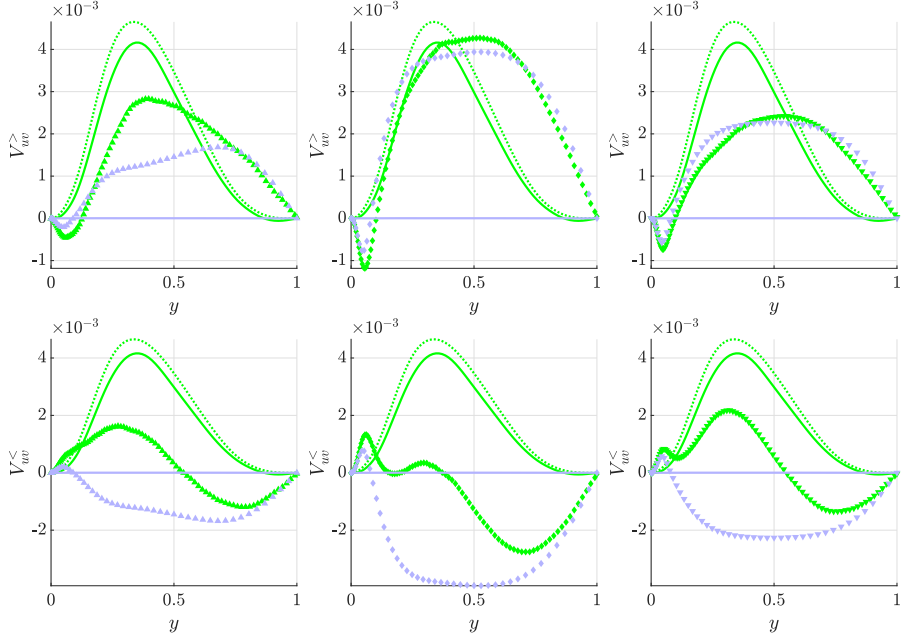


Figure 3.3: Contribution to the vertical mean component of the velocity from (top row) uv structures and (bottom row) the complementary portion of the domain for (light green) duct at the centre-plane and (light blue) channel at $Re_\tau = 180$. The fractional contributions are denoted with symbols and for increasing H_{uv} from left to right: $H_{uv} = 0.5$ (\blacktriangle), $H_{uv} = 2.0$ (\circ) and $H_{uv} = 4.0$ (\blacktriangledown). The ensemble average (solid lines) and the time average (dotted lines) are reported as reference.

mean velocity $V_{uv}^>$ and the complementary $V_{uv}^<$ in channel and duct for $Re_\tau = 180$ at the centre-plane. In the channel, $V_{uv}^>$ is negative for $y^+ < 15$ and positive elsewhere, and $V_{uv}^< = -V_{uv}^>$, in agreement with the definitions above and the fact that in the channel $V = 0$. The absolute values of $V_{uv}^>$ and $V_{uv}^<$ increase as H_{uv} increases at all wall-distances up to $H_{uv} \approx 2.0$, for which \mathcal{V}_{all} is $\approx 7\%$ of the total volume, and decreases for higher H , since too few events are sampled. This behaviour of $V_{uv}^>$ is in agreement with the observations by Lozano-Durán *et al.* (2012), who reported that intense ejections ($u < 0, v > 0$) are prevalent among intense uv in the channel, with the exception of the near-wall region where such events are inhibited by the presence of the wall.

In the duct a more complex behaviour is observed. At the centre-plane the relation between $V_{uv}^>$ and the mean V_{ens} varies at different wall-normal locations, and since $V \neq 0$, $V_{uv}^> \neq -V_{uv}^<$. Near the wall ($y^+ < 15$), $V_{uv}^>$ is negative and its intensity increases at higher H_{uv} , similarly to what was observed in channel flow. In the region between $y^+ \approx 20$ and $y \approx 0.4$, where the secondary flow

is more intense, $V_{uv}^>$ decreases as H_{uv} increases up to $H \approx 0.5$, increases for larger H_{uv} between $H_{uv} \approx 0.5$ and $H_{uv} \approx 2.0$, and decreases again for $H_{uv} > 2$. However, for $y > 0.4$, $V_{uv}^>$ follows the same behaviour as $V_{uv}^<$ in channel flow, increasing for higher H_{uv} up to $H \approx 2$ and decreasing for larger H_{uv} .

Interestingly, $V_{uv}^>$ in channel and duct are in good agreement for $H_{uv} \approx 2.0$ and higher. Furthermore, in the intermediate region between $y^+ = 20$ and $y = 0.4$, where the secondary motion is more intense, $V_{uv}^>$ of both duct and channel are in good agreement with V_{ens} in the duct, thus reaching in both cases the same intensity of the secondary motion. On the other hand, for $y > 0.4$, where the secondary flow is less intense, there is no agreement between V_{ens} and $V_{uv}^>$.

The contribution to V from the not sampled portion of the domain, $V_{uv}^<$, has a complementary trend. In the region between $y^+ = 20$ and $y = 0.4$, since $V_{uv}^< \approx V_{ens}$, $V_{uv}^<$ has an intensity lower than the same quantity in the channel. However, it becomes more relevant farther from the wall, where the weakening of the secondary motion is due to the balance between the positive $V_{uv}^>$ and the negative $V_{uv}^<$, which is the same phenomenon that in the channel leads to $V = 0$.

The contributions for channel and duct at $Re_\tau = 360$ are shown in Figure 3.4. In the channel, the trend for increasing H_{uv} is as for $Re_\tau = 180$: $V_{uv}^>$ (and $|V_{uv}^<|$) increases as H_{uv} gets larger up to $H_{uv} \approx 2.0$ and decreases for higher H_{uv} . In the duct, as opposed to the previous case, in the region where the secondary flow is particularly intense (approximately between $y^+ \simeq 20$ and $y \simeq 0.4$), $V_{uv}^>$ monotonically decreases with H_{uv} . As for the cases at $Re_\tau = 180$, for $H_{uv} \geq 2$, the $V_{uv}^>$ distributions are in very good agreement between channel and duct. However, $V_{uv}^>$ accounts for less than half of the intensity of the secondary flow, thus the contribution from weak events is more relevant ($|V_{uv}^<| > |V_{uv}^>|$) and it significantly differs between duct and channel.

These results can be summarised as follows: for every H_{uv} , at the wall-normal distances where $V_{uv}^>$ in the channel is higher than V in the duct, $V_{uv}^>$ and $V_{uv}^<$ in channel and duct are in relatively good agreement; for H_{uv} larger than the critical one identified by the percolation analysis, *i.e.* when the intense events are isolated, $V_{uv}^>$ are always in good agreement, at every wall-normal distance between channel and ducts, and such agreement is better for more rare events. Furthermore, the dependence on the wall-normal distance of $V_{uv}^>$ for intense events in the duct does not resemble that of V in the duct and it seems to be unaffected by the existence of the secondary flow.

As previously mentioned, in duct flows all the off-diagonal terms of the Reynolds-stress tensor are different than zero, and the fact that the cross-stream term appears in the transport equation for the mean cross-stream vorticity suggests that vw events may play an important role in the generation of the secondary motion. However, despite some quantitative differences, their contribution to V turned out to be qualitatively similar to that of uv events.

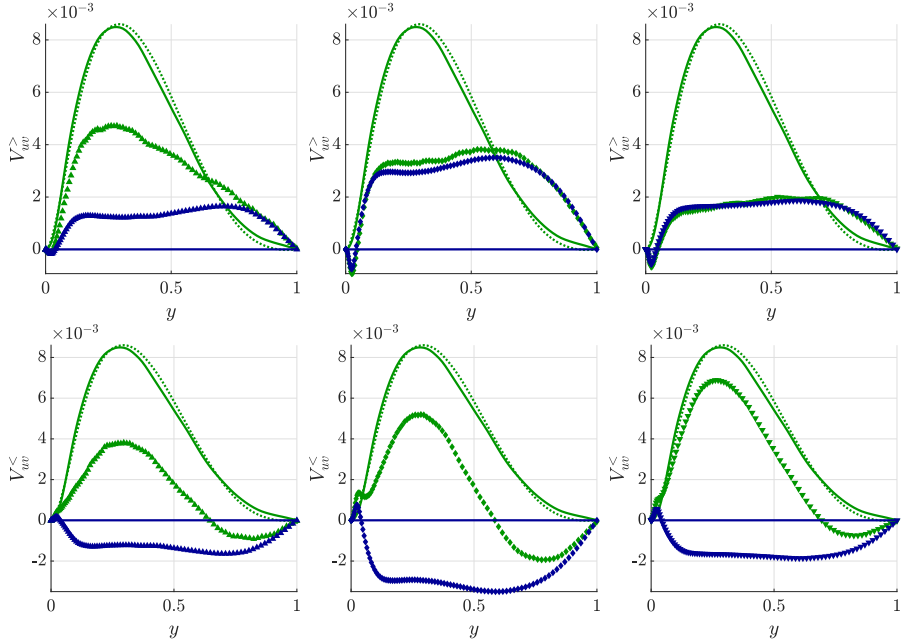


Figure 3.4: Contribution to the vertical mean component of the velocity from (top row) uv structures and (bottom row) the complementary portion of the domain for (dark green) duct at the centre-plane and (dark blue) channel at $Re_\tau = 360$. Symbols and lines as in Figure 3.3.

Figure 3.5 illustrates $V_{vw}^>$ at the centre-plane V for all the considered cases. In general, vw events have weaker fluctuations than uv , as can be argued by observing $\mathcal{V}_{\max}/\mathcal{V}_{\text{all}}$ in the percolation diagram, which after the crisis is lower for vw than for uv in all cases, as observed in Figure 3.2. Subsequently, in channel flow when H_{vw} is such that the contribution $V_{vw}^>$ is maximised, $V_{vw}^>$ is lower than $V_{uv}^>$, and the optimal thresholds that maximised $V_{vw}^>$ is $H_{vw} \simeq 1$, instead of $H_{uv} \simeq 2$ for uv (at both Reynolds numbers). At the centre-plane in the duct, as for $V_{uv}^>$, the $V_{vw}^>$ profile from the duct is in good agreement with that of the channel for $H_{vw} > 2$, but the two Reynolds numbers are more similar than the respective $V_{uv}^>$ profiles, since $V_{vw}^>$ in the region of more intense secondary flow is higher for $H_{vw} \approx 0.5$ than for $H_{vw} \approx 2$. This is due to the fact that $V_{vw}^>$ for $H_{vw} = 2.0$ is lower than V , as it happens for $V_{uv}^>$ at $Re_\tau = 360$.

3.1.4. Contributions to the secondary flow: corner region

We consider now the contribution to the secondary flow of intense events near the vertical walls. In Figure 3.6 we show $V_{uv}^>$ and $V_{uv}^<$ at the location of the first minimum of V ($z^+ \approx 50$) and $V_{uv}^>$ in the channel. Since in this region of the

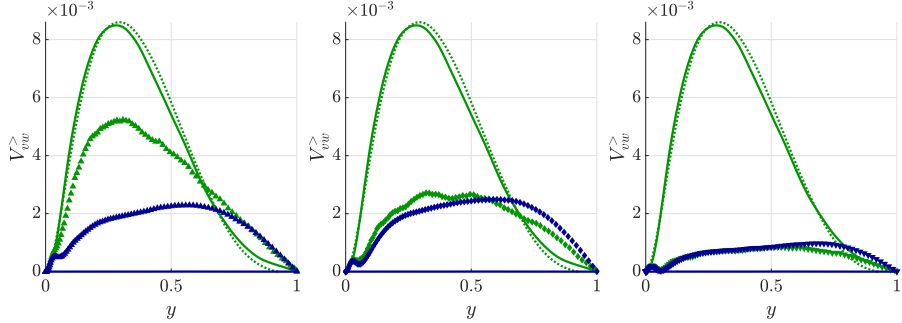


Figure 3.5: Contribution to the vertical component of the mean velocity V from vw events for (dark green) duct at the centre-plane and (dark blue) channel at $Re_\tau = 360$. Symbols and lines as in Figure 3.3.

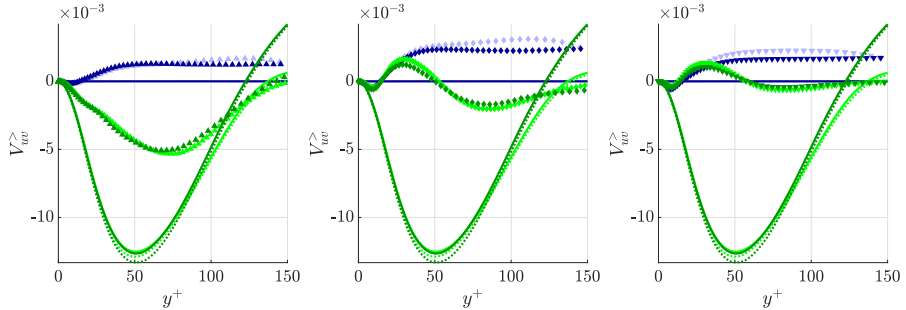


Figure 3.6: Contribution to the vertical mean component of the velocity from (top row) uv structures for (green) duct at the location of the first minimum ($z^+ \approx 50$) and (blue) channel. Dark and light colours for $Re_\tau = 360$ and $Re_\tau = 180$, respectively. Symbols for the thresholds and the time and ensemble average as in Figure 3.3.

duct V scales where it is expressed as a function of the inner-scaled wall-normal distance, the data are reported for both Reynolds numbers.

It is worth noting that at this location V of the duct is negative, which makes the behaviour of $V_{uv}^>$ not trivial to predict, given the predominance of ejections among intense events in the channel and at the duct core. In fact, $V_{uv}^>$ is qualitatively different from V at the duct core region and in the channel. For $H_{uv} = 0.5$, *i.e.* before the percolation crisis, $V_{uv}^>$ in the duct is negative and it differs from $V_{uv}^>$ at every wall-distance. However, as H_{uv} increases, the absolute value of the contribution $V_{uv}^>$ decreases monotonically and eventually $V_{uv}^>$ changes sign in the region below the corner bisector ($y^+ \approx 50$). For H_{uv} high enough to isolate the intense events, in the region $y^+ < 25$ the contribution

$V_{uv}^>$ is again in good agreement with the that of the channel. Therefore, it is possible to conclude that in this region ejections are still dominant among the intense events, despite the fact that the secondary flow has negative sign. On the other hand, for $y^+ > 25$, $V_{uv}^>$ does not match with the distribution of the channel in either of the two Reynolds numbers.

Interestingly, the location of the bisector, $y^+ = 50$, is also the location where $V_{uv}^>$ changes sign where the most intense events are considered. The fact that for $y^+ > 50$ the contribution $V_{uv}^>$ for the duct is negative, is a clear sign of the influence of the vertical wall on the coherent structure near the corner. Such events are perceived as intense spanwise fluctuations by the flow on the vertical wall and they show a preferential orientation towards the nearest horizontal wall.

It is worth noting that, although the contribution $V_{uv}^>$ remains relatively low, this is the only circumstance for which it is possible to observe a qualitative difference between intense events in channel and duct.

At each wall-normal location, the absolute value of $V_{uv}^>$ is significantly lower than that of V , and for $H_{uv} = 4.0$ $V_{uv}^>$ almost vanishes above the corner bisector ($y^+ > 50$), since in that region the probability of detection is also particularly low (Figure 3.2). Therefore, $V_{uv}^<$ has a predominant role in the near-corner region, for both Reynolds numbers. In particular, for $H_{uv} = 2.0$, $V_{uv}^<$ is already of the order of magnitude of V , and for $H_{uv} = 4.0$ the agreement between V and $V_{uv}^<$ is remarkably good.

The relative importance of the fractional contributions to the mean velocity for $z^+ = 50$ is also observed for the entire near-corner region of the duct ($z^+ < 50$). We also examined the contributions to V from vw events, $V_{vw}^<$ and $V_{vw}^>$, but they are similar to the ones previously described and they are not shown here.

3.1.5. Coherent structures: location and size

In this section we examine the geometrical properties of the coherent structures in terms of their distance from the wall and the value of the threshold H_{uv} . We focus on uv events, because they have the highest contribution to the secondary motion, and we take into account the symmetries in the channel and the duct: in the former, we apply a change of reference system to the structures from which the centre of mass is located in the upper half of the domain; in the latter, all the structures are referred to the lower-left quadrant. Note that the centre of mass of the structures is defined as:

$$\mathbf{x}_{\text{cm}} = \frac{1}{\mathcal{V}} \sum_{i=1}^N \mathcal{V}_i \mathbf{x}_i, \quad (3.3)$$

where N is the number of connected grid points in the structure, \mathcal{V}_i the characteristic volume assigned to each grid point, \mathbf{x}_i is the position of the point and \mathcal{V} is the total volume.

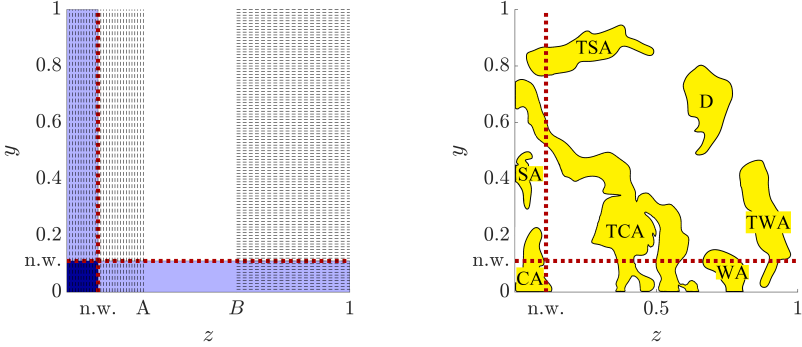


Figure 3.7: Summary of the structure classification in the duct. (Right) Regions of domain relevant for the structure analysis. The regions defined in inner units are illustrated for $Re_\tau = 180$ only. Near-wall (n.w.) regions ($y^+ < 20$ or $z^+ < 20$) and the near-corner region ($y^+ < 20$ and $z^+ < 20$), spanwise regions (vertical dashed lines) A ($z^+ < 50$) and (horizontal dashed lines) B ($z > 0.6$). (Left) Realistic representation of objects which belong to the different families: detached (D), wall attached (WA), side attached (SA), tall-wall attached (TWA), tall-side attached (TSA), corner attached and tall-corner attached (TCA). The figure does not represent an actual instantaneous cross-section.

In channel flows three different families of structures are identified, which we will denote as follows: wall-attached objects (WA), whose centre of mass is located in a near-wall region below $y^+ \approx 20$; detached objects (D), located far from the wall; and tall wall-attached (TWA), which extend from the region near the wall up to the core of the channel, sometimes being connected with both walls. In duct flows, uv are classified into seven different families using the location of the nearest points to both walls, y_{\min} and z_{\min} , and the centre of mass. These families are defined as follows: detached structures (D), with $y_{\min}^+ > 20$ and $z_{\min}^+ > 20$; wall-attached structures (WA), $y_{\text{cm}}^+ < 20$; side-attached structures (SA), $z_{\text{cm}}^+ < 20$; tall-wall attached structures (TWA), $y_{\min}^+ < 20$; tall-side attached structures (TSA), $z_{\min}^+ < 20$; corner attached structures (CA), $y_{\text{cm}}^+ < 20$ and $z_{\text{cm}}^+ < 20$; and tall-corner attached structures (TCA), $y_{\text{cm}}^+ < 20$ and $z_{\text{cm}}^+ < 20$. Note that TCA structures are often large objects with some ramification attached to perpendicular walls, rather than

We define two distinct spanwise regions in the duct, as shown in Figure 3.7: region A extends from the vertical wall to $z^+ = 50$, which is the location of the minimum of V ; region B extends from the $z = 0.6$ to the centre of the duct. The structures are assigned to region A or B based on the position of the centre of mass, discarding the ones which are located neither in A nor B. The existence of the objects belonging to each family is shown by the joint-probability density functions (JPDF, denoted by $p(X, Y)$ hereafter for two generic variables X

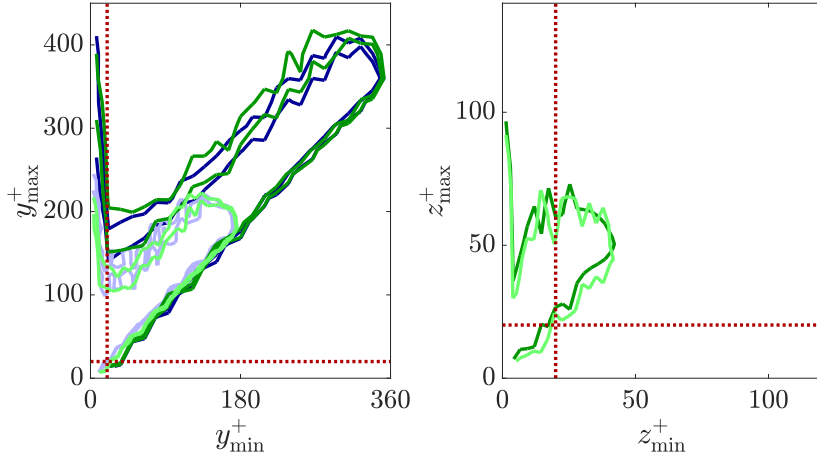


Figure 3.8: (Left) JPDF of the minimum and maximum distance of the identified objects to the horizontal walls in the duct region B and in the channel. (Right) JPDF of the minimum and maximum distance of the identified objects to the vertical walls in region A. The contours represent 95% of the sampled objects. The dotted red lines are $y^+ = 20$ and $z^+ = 20$. Blue for channel and green for duct flow. Dark and light colour for $Re_\tau = 360$ and $Re_\tau = 180$, respectively.

and Y), of the minimum and maximum distances from the horizontal wall and vertical walls. In Figure 3.8 we show $p(y_{\min}^+, y_{\max}^+)$ and $p(z_{\min}^+, z_{\max}^+)$, in region B in the duct and the channel, and in region A of the duct, respectively. It is possible to note a number of similarities in $p(y_{\min}^+, y_{\max}^+)$ between channel and duct at the same Reynolds number: the existence of objects extending from the near-wall region to the core region in both flows ($y_{\min}^+ < 20$ and $y_{\max}^+ > 20$) and, in particular, of very large objects which extend through the near-wall region to the opposite half of the domain ($y_{\min}^+ < 20$ and $y_{\max}^+ > 180$ for $Re_\tau = 180$ and $y_{\min}^+ < 20$ and $y_{\max}^+ > 360$ for $Re_\tau = 360$).

Interestingly, despite the fact that the geometrical constraints prevent a proper matching of $p(y_{\min}^+, y_{\max}^+)$ in inner-scaling, $y^+ < 20$ is recognisable at both Reynolds numbers as the region from where the TWA objects originate, since for higher y^+ there are no structures with an extension in the vertical direction comparable to that of TWA structures. On the other hand, $p(z_{\min}^+, z_{\max}^+)$ for region B exhibits a very good agreement between both Reynolds numbers. Note that such agreement is not limited to the extreme values of z_{\min}^+ and z_{\max}^+ , which is just a consequence of the sampling region being defined in inner units.

An aspect which has received little attention in similar studies is how the classification into different families is affected by the choice of the threshold H_{uv} . This is in part due to the fact that the percolation analysis provides natural choices of H_{uv} based either on fractions of the critical value for which the

percolation crisis occurs, or on the optimal value at which the highest number of structured are detected. Furthermore, the contributions of the structures to the statistics generally have a relatively smooth dependency on H_{uv} (Lozano-Durán *et al.* 2012). However, $V_{uv}^>$ changes qualitatively in the duct for different H_{uv} , and in particular in the core region it is in better agreement with the channel for higher H_{uv} at both Reynolds numbers.

We therefore examined how the volume fraction occupied by different families evolves with respect volume of all the identified structures \mathcal{V}_{all} for different values of H_{uv} (including those for which we compared $V_{uv}^>$), as shown in Table 3.2.

In channel flow, where the D, WA and TWA families are considered, the effect of increasing H_{uv} is to reduce the relative space occupied by TWA structures, to the advantage of both WA and D objects. For $H_{uv} = 0.5$, *i.e.* a threshold lower than the critical one but still high enough to have a high number of individual structures, most of the points fulfilling the condition are gathered in large TWA objects which together provide $\approx 90\%$ of \mathcal{V}_{all} (results not shown here). Despite this, \mathcal{V}_{all} is between $\approx 30\%$ and $\approx 40\%$ of the entire computational domain. For $H_{uv} = 2.0$ the TWA objects still occupy the largest portion of volume among all the types of structures, but their relative importance is reduced to $\approx 60\%$ of \mathcal{V}_{all} . For even higher values of the threshold, *e.g.* for $H_{uv} = 4.0$, only the stronger fluctuations are still detected and therefore most of the TWA are broken down into D structures, which then become the most representative in terms of volume ($\approx 70\%$ of \mathcal{V}_{all}). Note that at such high values of H_{uv} , only rare and small very intense events are sampled and \mathcal{V}_{all} is $\approx 2\%$ of the domain.

In duct flow, where seven different families are defined, the effect of increasing the threshold is more complex. Similarly to the channel, the largest structures with $H_{uv} = 0.5$, which are TCA connected to at least two contiguous walls, account for more than the $\approx 90\%$ of \mathcal{V}_{all} . However, as H_{uv} increases, the contribution of TCA to the total volume drops and, for $H_{uv} = 2.0$, it is reduced to less than 10% of \mathcal{V}_{all} . Interestingly, at this H_{uv} the combined volume fraction from tall-attached objects (TWA, TSA and TCA) is lower in the duct than in the channel, and, subsequently, detached and wall-attached objects (WA and SA) have a higher share of \mathcal{V}_{all} . For $H_{uv} = 4.0$, following the same trend previously observed in channel flow, large attached structures become less important than detached ones in terms of occupied volume.

Reynolds-number effects can also be observed in the distribution of structures among families for both channel and duct. Since the near-wall region is a relatively smaller portion of the domain (in outer scaling) for higher Reynolds number, the volume fraction of D objects increases and that of SA and WA decreases as the Reynolds number increases. On the other hand, the volume fraction of tall attached objects has a weaker Reynolds-number dependence, since the bigger objects in these families tend to extend through a large portion of the cross section of the domain, a fact that is in agreement with what was

reported for channel at much higher Reynolds number by Lozano-Durán *et al.* (2012).

Table 3.2: Number of structures in the entire data-set N_{struct} , ratio between the overall volume occupied by structures and the computational domain $\mathcal{V}_{\text{all}}/\mathcal{V}_{\text{domain}}$, fraction in terms of number of objects volume (the latter in bold font) for uv structures of different families in channel (c) and duct (d).

$Re_\tau = 180$			
H_{uv}	1.0	2.0	4.0
N_{struct}	$343 \cdot 10^3$	$313 \cdot 10^3$	$154 \cdot 10^3$
$\mathcal{V}_{\text{all}}/\mathcal{V}_{\text{domain}}$	<u>0.20</u>	<u>0.07</u>	<u>0.02</u>
D(c)	0.60 (0.10)	0.52 (0.30)	0.50 (0.68)
WA(c)	0.25 (0.01)	0.26 (0.05)	0.33 (0.07)
TWA(c)	0.15 (0.89)	0.22 (0.65)	0.17 (0.25)
N_{struct}	$1.16 \cdot 10^6$	$877 \cdot 10^3$	$390 \cdot 10^3$
$\mathcal{V}_{\text{all}}/\mathcal{V}_{\text{domain}}$	<u>0.20</u>	<u>0.07</u>	<u>0.01</u>
D(d)	0.45 (0.13)	0.46 (0.31)	0.44 (0.52)
WA(d)	0.16 (0.02)	0.16 (0.06)	0.22 (0.12)
SA(d)	0.14 (0.04)	0.15 (0.08)	0.16 (0.09)
TWA(d)	0.07 (0.14)	0.09 (0.32)	0.08 (0.19)
TSA(d)	0.09 (0.17)	0.08 (0.15)	0.04 (0.05)
CA(d)	0.07 (≈ 0)	0.05 (0.01)	0.06 (0.02)
TCA(d)	0.02 (0.50)	0.01 (0.07)	≈ 0 (0.01)
$Re_\tau = 360$			
H_{uv}	1.0	2.0	4.0
N_{struct}	$448 \cdot 10^3$	$362 \cdot 10^3$	$174 \cdot 10^3$
$\mathcal{V}_{\text{all}}/\mathcal{V}_{\text{domain}}$	<u>0.20</u>	<u>0.07</u>	<u>0.02</u>
D(c)	0.65 (0.13)	0.58 (0.36)	0.52 (0.79)
WA(c)	0.23 (0.01)	0.24 (0.02)	0.33 (0.04)
TWA(c)	0.12 (0.86)	0.18 (0.62)	0.15 (0.17)
N_{struct}	$1.46 \cdot 10^6$	$1.31 \cdot 10^6$	$565 \cdot 10^3$
$\mathcal{V}_{\text{all}}/\mathcal{V}_{\text{domain}}$	<u>0.34</u>	<u>0.11</u>	<u>0.02</u>
D(d)	0.52 (0.11)	0.50 (0.42)	0.48 (0.72)
WA(d)	0.14 (0.01)	0.14 (0.03)	0.21 (0.06)
SA(d)	0.15 (0.01)	0.14 (0.03)	0.17 (0.05)
TWA(d)	0.06 (0.05)	0.10 (0.34)	0.08 (0.14)
TSA(d)	0.09 (0.08)	0.09 (0.13)	0.03 (0.03)
CA(d)	0.03 (0.01)	0.02 (≈ 0)	0.03 (≈ 0)
TCA(d)	0.01 (0.73)	0.01 (0.05)	≈ 0 (≈ 0)

3.1.6. Dimension of structures in different families

In the following we describe the geometrical properties of the structures belonging to the various families, with the main aim of identifying features which distinguish coherent structures in duct and channel flow.

The structure sizes are defined based on the bounding box, *i.e.* the length in the streamwise direction is defined for each structure as $\Delta_x = x_{\max} - x_{\min}$. The sizes are scaled in viscous units, employing in the duct the wall-shear stress at the centre plane, despite the fact that it is not uniform in the spanwise direction. Note that scaling with the local friction velocity was also considered, but since most of the coherent structures are relatively large the results do not differ significantly. We observed that the choice of H_{uv} has a lower impact on the probability density functions (PDF) of the sizes than on the volume fraction for the different families, therefore we report the PDF only for $H_{uv} = 2.0$ in most cases.

We firstly examine the size of small objects attached to the wall. Figure 3.9 (top) shows the PDF of the lengths in the three directions for the CA and the WA objects in regions A and B in the duct and the WA objects in the channel (CA are all included in region A of the duct by definition). There is good agreement between the data of the same family scaled in inner units for the two Reynolds numbers, as well as between the WA structures in region B of the duct and the WA objects in the channel. Interestingly, the WA structures in region A of the duct are longer than in region B and in the channel, despite having the same size in y and z . On the other hand, the longest CA structures are as long as the longest WA objects in region B and the WA structures in channel flow, despite the fact that the most common CA structures are shorter than the WA structures for all the directions, and in particular in z .

The presence of the vertical wall in the duct and the geometrical constraints of the domain have a strong impact on the sizes of TWA objects, which are shown in Figure 3.9 (middle) for the channel and the two spanwise regions in the duct. TWA structures in region A are significantly smaller than in region B or in the channel and their sizes scale in inner units in all the directions. On the other hand, since the largest TWA structures in region B of the duct and in the channel occupy the entire extension of the domain in the vertical direction, the distribution of Δ_y does not scale in inner units, but, interestingly, there is good agreement between channel and duct at the same Reynolds number.

It is important to note that the disagreement between the PDFs of Δ_x and Δ_y from TWA structures in regions A and B of the duct is not entirely due to a fundamental difference in the geometrical properties of intense uv events. Instead, it is in part a consequence of the fact that objects in region A that are large enough to match the size of the TWA structures in region B, also become attached to both walls and therefore are classified as TCA.

The similarities between the large TCA and TWA objects in the absence of the vertical wall can be appreciated in Figure 3.9 (bottom), where the PDF of sizes are shown for the TCA structures in regions A and B of the duct and the

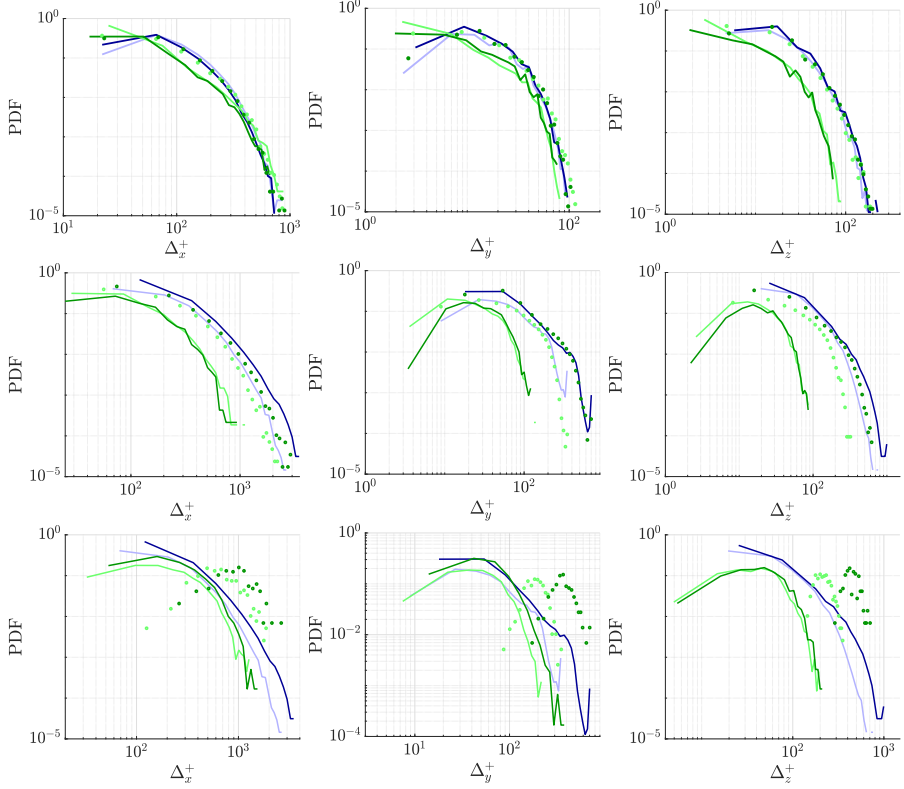


Figure 3.9: PDF of: (left column) Δ_x^+ , (middle column) Δ_y^+ and (right column) Δ_z^+ , for $H_{uv} = 2.0$. Top row: (blue solid lines) WA in channel, (green solid lines) WA in duct, region A, (green symbols) WA in duct, region B, (dashed lines) CA in duct. Middle row: (blue solid lines) TWA in channel, (green solid lines) TWA in duct, region A, (green symbols) TWA in duct, region B. Bottom row: (blue solid lines) TWA in channel, (green solid lines) TCA in duct, region A, (green symbols) TCA in duct, region B. Bottom row, left: TCA in region B for $H_{uv} = 1.0$ in symbols. Dark and light colour for $Re_\tau = 360$ and $Re_\tau = 180$, respectively.

TWA structures in the channel. The PDF of the sizes Δ_x^+ and Δ_y^+ of the TCA structures in regions A are in better agreement with those of TWA objects in the channel than the TWA sizes in the same region, although the largest TCA structures in the duct in region A remain shorter than the TWA in the channel, both in the x and y directions. The size in the spanwise direction is smaller for both TWA and TCA structures in region A, but for TCA it peaks at $\Delta_z^+ = 50$, with a relatively high number of structures for $\Delta_z^+ > 100$, namely twice the length of region A itself.

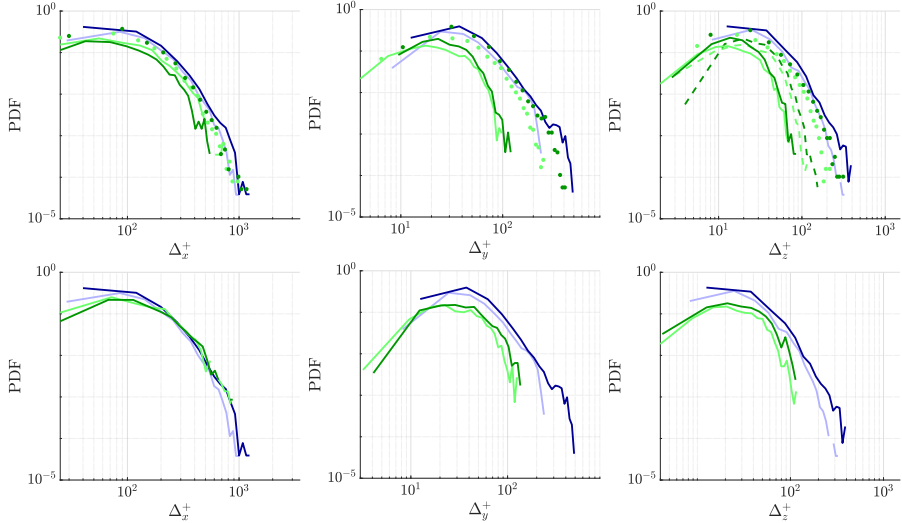


Figure 3.10: PDF of: (left column) Δ_x^+ , (middle column) Δ_y^+ and (right column) Δ_z^+ , for $H_{uv} = 4.0$. Top row: (blue solid lines) TWA in channel, (green solid lines) TWA in duct, region A, (green symbols) TWA duct, region B. Bottom row: (blue solid lines) TWA in channel, (green solid lines) TCA in duct, region A, (green symbols) TCA in duct, region B. Bottom row, left: TCA in region B for $H_{uv} = 1.0$ in lines with symbols. Dark and light colour for $Re_\tau = 360$ and $Re_\tau = 180$, respectively.

The PDF distributions for TCA structures in region B is severely affected by the combined conditions of being attached to two contiguous walls and having the centre of mass at a relatively high distance from the vertical walls. Subsequently, this family is characterised by very large objects for which the PDFs of Δ_y^+ and Δ_z^+ scale well in outer units. The most common TCA structures in region B have $\Delta_y^+ \approx 180$ and $\Delta_y^+ \approx 360$ (*i.e.* $\Delta_y \approx 1$) for $Re_\tau = 180$ and $Re_\tau = 360$, respectively, and similar Δ_z^+ , with both smaller and larger structures being relatively less likely.

It is interesting to note that, as suggested by the dependency of the volume fraction for the different families on different H_{uv} , the geometrical properties of TCA objects in region B are the most affected by the choice of the threshold. This is shown only for Δ_x^+ : for $H_{uv} = 1.0$, at both Reynolds numbers, several TCA structures in region B are almost as long as the entire computational domain, which is in agreement with the fact that such threshold is lower than the critical one.

We describe the effects of a higher threshold considering the PDFs of the sizes for $H_{uv} = 4.0$, which are shown in Figure 3.10. As previously discussed, for this value of the threshold the total number of detected structures is lower

than half of the total for $H_{uv} = 2.0$, and \mathcal{V}_{all} is never above 2% of the domain volume. Nevertheless, most of the trends observed at $H_{uv} = 2.0$ are still present. The PDFs of the sizes for small attached objects are in very good agreement with the curves at $H_{uv} = 2.0$ and are not shown here, while the large attached objects are in general smaller in both channel and duct. The PDFs of Δ_x^+ and Δ_y^+ for TWA structures in region B of the duct remain in good agreement with those of the TWA structures in the channel, and the Δ_z^+ PDFs are more similar in the two flows than at $H_{uv} = 2.0$. Furthermore, for $H_{uv} = 4.0$ the TWA structures are shorter than for $H_{uv} = 2.0$ both in the core of the duct and in the channel and thus the agreement of their Δ_x^+ PDF with that of TCA structures in the corner region of the duct is better at $H_{uv} = 4.0$ than at lower values of H_{uv} .

The most relevant differences between the properties of the structures for $H_{uv} = 2.0$ and $H_{uv} = 4.0$ are related to the size of the structures in the vertical direction. In fact, whereas in both channel and duct with $H_{uv} = 2.0$ it is possible to observe the existence of objects as large in y as the vertical length of the domain, at $H_{uv} = 4.0$ the probability of such events to be detected is negligible. Furthermore, TCA objects in region A of the duct are more similar to the TWA structures in the same region, as opposed to what is observed for the TWA structures in region B, and are too small to be affected by geometrical constraints. Subsequently, their Δ_y^+ PDFs scale in inner-units. Finally, it is interesting to note that the TCA family is virtually absent from region B of the duct at both Reynolds numbers.

3.1.7. Minimal flow in turbulent ducts

A possible way to further investigate the secondary flow of Prandtl's second kind in turbulent ducts is to use the concept of minimal-flow units (Jiménez & Moin 1991). The secondary flow of second kind is only present in turbulent flows, so reducing the range of active scales in the domain can be beneficial in clarifying its origin and what are the turbulent structures relevant for it. A similar perspective but different techniques have been employed in other studies for this goal. For instance, Pinelli *et al.* (2010) carried out simulations in the range of average friction Reynolds numbers between $Re_\tau^* = 80$ and 225, and related the non-uniform wall-shear stress at the wall with the number of near-wall streaks which are allowed by the geometrical constraints (note that Re_τ^* denotes the Reynolds number averaged on the duct cross-section). On the other hand, Modesti *et al.* (2018) suppressed the secondary flow using a volume force to investigate its role in momentum transport.

We performed simulations of square ducts at $Re_\tau = 180$ with progressively shorter domains, including $L_x = 12.5, 6, 3, 2$, and 1. Note that $L_x = 25$ for the dataset described by Vinuesa *et al.* (2018) and considered in **Papers 8 & 9**. Figure 3.11 (top) shows the streamwise velocity on horizontal planes at a distance from the wall of $y^+ = 25$ (based on the friction velocity at the centre plane). As expected, the progressively shorter domain reduces the streak

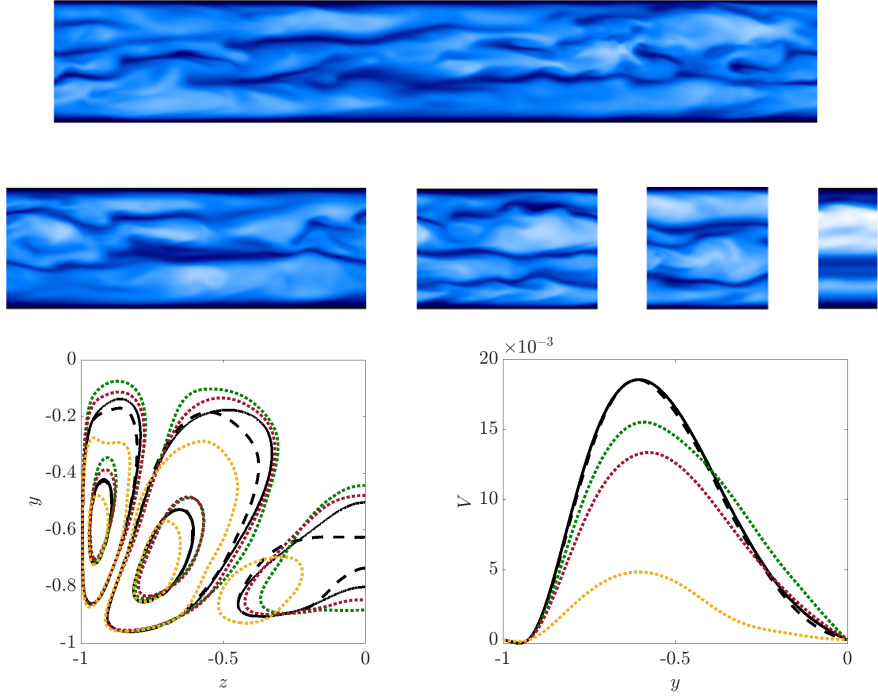


Figure 3.11: Flow across ducts with a progressively shorter domain. (Top panel) Streamwise velocity at $y^+ = 25$ for $L_x = 12.5, 6, 3, 2$, and 1 . (Bottom left) contours of the mean velocity vertical component, V , scaled with its maximum and (bottom right) vertical profile of V at the location of the near-corner maximum ($z \approx -0.95$). Black solid and dashed lines denote $L_x = 12.5$ and 6 , respectively, and green, red, and yellow lines denote $L_x = 3, 2$, and 1 , respectively.

meandering in the near-wall region. For the shortest domain length, we observed that only a single high-speed streak is present at most time steps, although the flow is still not fully relaminarized. This is perhaps a surprising result since (Jiménez & Moin 1991) reported that the minimal domain length for turbulence to be sustained in a periodic channel is between $L_x^+ = 250$ and 350 . We observed that the pattern of the secondary flow is recognisable for most domain lengths L_x , in particular in the corner region where it is more intense, including the case with $L_x = 1$ (Figure 3.11, bottom left). However, its intensity is progressively reduced in cases with shorter domains (Figure 3.11, bottom right).

These preliminary findings possibly corroborate the conclusions of **Papers 8 & 9**, excluding a direct connection between secondary flow and intense Reynolds-stress events. In fact, on the one hand, the secondary flow is stronger

when the domain length does not interfere with the near-wall cycle, which is a direct consequence of the role that turbulent fluctuations have in generating mean streamwise vorticity. On the other hand, however, it is still present in artificial flow configurations where burst and large ejections do not occur, because of the very short domain length.

This study requires further effort to obtain more convincing conclusions. For instance, using techniques as proper orthogonal decomposition (POD) or empirical mode decomposition (EMD) could help to clarify how the flow dynamics changes for different domain lengths. Unfortunately, the very low statistical convergence and the small intensity of the secondary flow lead to high computational costs even for low Reynolds numbers, and its particular scaling properties require considering at least one case at $Re_\tau > 300$.

3.2. Intense events in boundary layers over airfoils

In **Paper 10**, we discuss structure identification in the turbulent boundary layers around a NACA4412 airfoil at $Re_c = 200,000$, and we present some preliminary results on the connection between intense Reynolds-stress events and wall-normal convection. In **Paper 11**, the same analysis is carried out including cases with control. In the present section, I summarize our observations on the opportunity of taking into account the TNTI interface and discuss the quadrant distribution at different wall-normal distances on the pressure and suction sides of the uncontrolled case.

Compared with the previous studies on channel and ducts, external flows such as boundary layers developing around a wing section require considering more carefully the case geometry. For instance, it is possible to perform the structure identification globally in the entire domain, including the wake. This approach would allow studying *e.g.* mixing between suction- and pressure-side boundary layers downstream the trailing edge, but it poses difficult challenges in establishing a consistent threshold and we determine that it was not convenient to investigate pressure-gradient effects. We focused on two subsets of the computational domain, corresponding to the regions between $x/c = 0.2$ and $x/c = 0.8$ on the suction and pressure sides, and we perform the structure identification on a rotated frame of reference, substituting the vertical and horizontal directions with the wall-tangential and wall-normal directions, respectively. Hereafter, the subscripts $(\dots)_t$ and $(\dots)_n$ are omitted for simplicity, so that *e.g.* the condition for intense Reynolds-stress events is written as in 3.1 for channel flow:

$$|uv| > H_{uv} u_{\text{rms}} v_{\text{rms}} . \quad (3.4)$$

However, in this expression, u and v denote the instantaneous velocity fluctuations in the wall-tangential and wall-normal directions, respectively, and u_{rms} and v_{rms} the corresponding root-mean-squared distributions.

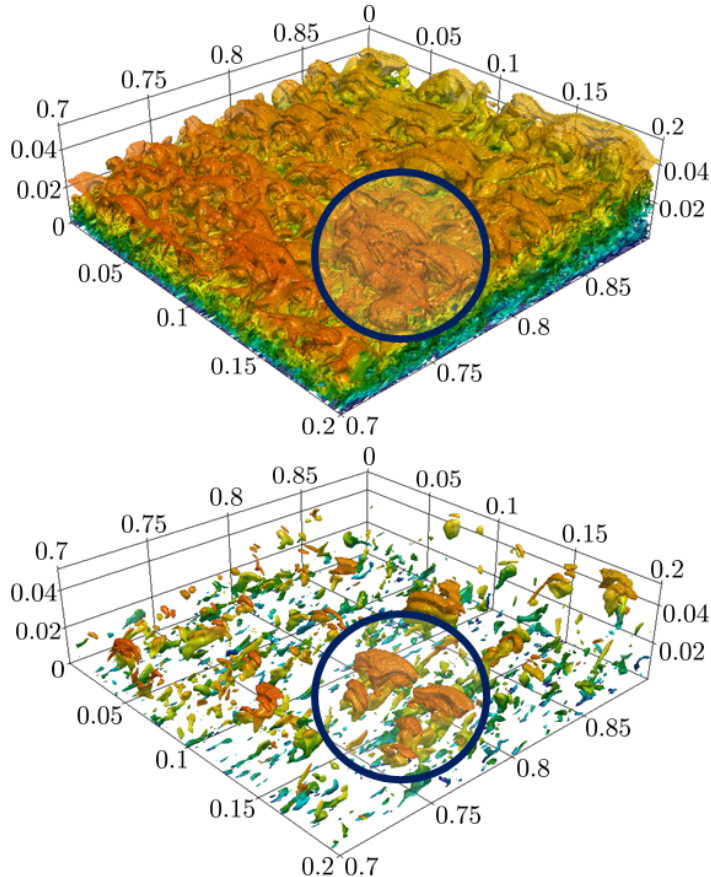


Figure 3.12: Intense Reynolds-stress events above the suction side of the airfoil for (top) $H_{uv} = 0.25$ and (bottom) $H_{uv} = 0.4$, coloured with the wall-tangential velocity. Structures that cross the TNTI interface are almost not affected by H_{uv} increase.

3.2.1. Turbulent-non-turbulent interface and structure identification

As mentioned before, conditions 3.1 give ambiguous results at very low y^+ due to the low values of the normalization factors such as $u_{\text{rms}}v_{\text{rms}}$. A similar effect is also observed in the region at a distance above the turbulent-not-turbulent interface (TNTI), as illustrated in Figure 3.12. This Figure shows coherent structures in the domain section above the suction side of the airfoil and between $x/c = 0.7$ and $x/c = 0.9$ for two values of the thresholds, *i.e.* $H_{uv} = 0.25$ and 4 (note that the rotated reference frame is used). At $H_{uv} = 0.25$, a significant volume fraction of the flow is included in coherent structures, most of which

are very large objects. This value is close to the percolation crisis for most turbulent flows and lower than that usually employed in structure identification. Increasing H_{uv} leads to progressively reducing the volume fraction, and splitting occurs simultaneously in the domain at the critical H_{uv} of the percolation crisis. After the percolation crisis, intense events become progressively smaller and eventually disappear, depending on their intensity. However, as illustrated for $H_{uv} = 4$, which is a much larger value than the critical one, structures in the laminar region of the flow above the TNTI have higher persistence because of the extremely low values of $u_{\text{rms}}v_{\text{rms}}$. These structures are extensions of intense events in the boundary layer propagating as large areas of very low-amplitude velocity fluctuations in the laminar region, and they are not directly comparable with that in the turbulent boundary layer. We thus examined three different conditions to apply in conjunction with 3.1 to restrict the identification region.

The first condition is based on the enstrophy criterion formulated by Bisset *et al.* (2002) to identify the TNTI and it reads:

$$|\tilde{\omega}| > C_e U_e / \delta_{99}. \quad (3.5)$$

In this expression, $|\tilde{\omega}| = \sqrt{\tilde{\omega}_1^2 + \tilde{\omega}_2^2 + \tilde{\omega}_3^2}$ is the square-root of the local enstrophy, U_e is the mean-velocity component in the wall-tangential component, δ_{99} is the boundary-layer thickness, and C_e is a numerical threshold which is arbitrary assigned. Note that $\tilde{\omega}_1$, $\tilde{\omega}_2$, and $\tilde{\omega}_3$ denote the three component of the instantaneous vorticity. The second condition is based on the modified kinetic-energy criterion formulated by Chauhan *et al.* (2014) and it reads:

$$\tilde{k}^* > C_k^* U_e^2, \quad (3.6)$$

where \tilde{k}^* denotes the flow kinetic energy in the frame of reference moving with free-stream velocity and averaged over a small volume of fluid and C_k^* has the same role as C_e . The third condition is based on the turbulent kinetic energy and the mean kinetic energy at the edge of the boundary layer, denoted by $k = 1/2(\bar{u}^2 + \bar{v}^2 + \bar{w}^2)$ and $\tilde{k} = 1/2(u^2 + v^2 + w^2)$, respectively, and it reads:

$$\tilde{k} > C_k k_e, \quad (3.7)$$

where C_k is a scalar value. Note that the previous conditions were developed specifically to study the behaviour the flow in the region accross the TNTI. The third criterion is not selected to represent precisely the TNTI, but it is the simplest to implement using the same minimal amount of data that is already required by the turbulent identification. Furthermore, it excludes the viscous sub-layer as well, thus rendering superfluous *ad-hoc* conditions at the wall. The qualitative effects of the three criteria for the instantaneous flow field at $x/c = 0.8$ are shown in Figure 3.13. We determine that, at least for the considered dataset (**Paper 9**), it is possible to select values for the three thresholds C_e , C_k^* , and C_k which yield the same mean location of the interface. Furthermore, if the mean location of the interface is the same, the impact of using a different criterion on the quantities such as probability detection or

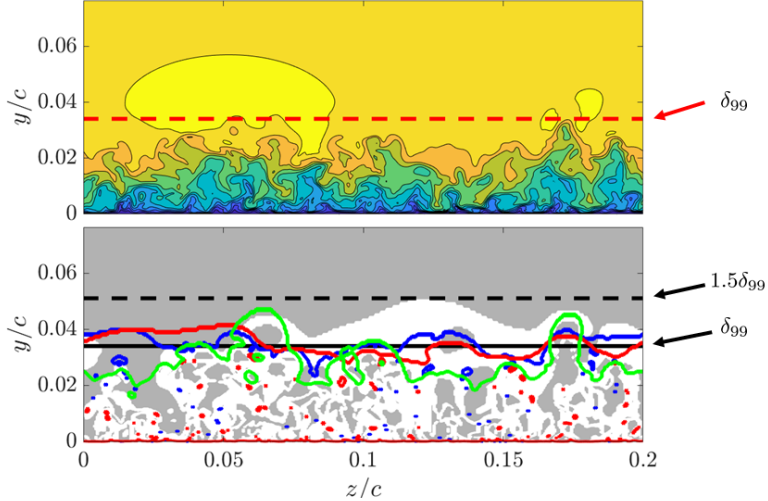


Figure 3.13: (Top) Instantaneous streamwise velocity at $x/c = 0.8$ on the airfoil suction side and (bottom) comparison between the regions where conditions (blue) 3.5, (green) 3.6, and (red) 3.7 are fulfilled for the same time step. The grey contours denote regions where $|uv| > Hu_{\text{rms}}v_{\text{rms}}$, for $H = 2$.

contributions turned out to be negligible, a fact that allows selecting condition (3.7). Intense uv events are thus defined as flow regions where:

$$\begin{cases} \tilde{k} > C_k k_e \\ |uv| > H_{uv} u_{\text{rms}} v_{\text{rms}} . \end{cases} \quad (3.8)$$

From now on, we will focus on these structures.

3.2.2. Effects of the adverse pressure gradient

A prominent feature of APG turbulent boundary layers is more intense velocity fluctuations in the outer region. Before performing comparisons between different pressure-gradient conditions, an interesting question is how the distribution of Reynolds-stress events change when various fluctuation intensities are considered. Figure 3.14 illustrates the probability of detecting the different quadrants at various values of the threshold H_{uv} at $x/c = 0.8$ on the suction side of the NACA4412 at $Re_c = 200,000$. The wall-normal profiles in this Figure are shown up to δ_{99} , which corresponds to the TNTI average location. Note that the four quadrants are defined based on how regions with velocity fluctuations are distributed in the uv Cartesian plane. In particular, Q1 denote regions where $(u > 0, v > 0)$; Q2 denote regions where $(u < 0, v > 0)$, called ejections; and Q3 and Q4 denote regions where $(u < 0, v < 0)$ and $(u > 0, v < 0)$, respectively, the latter of which are called sweeps.

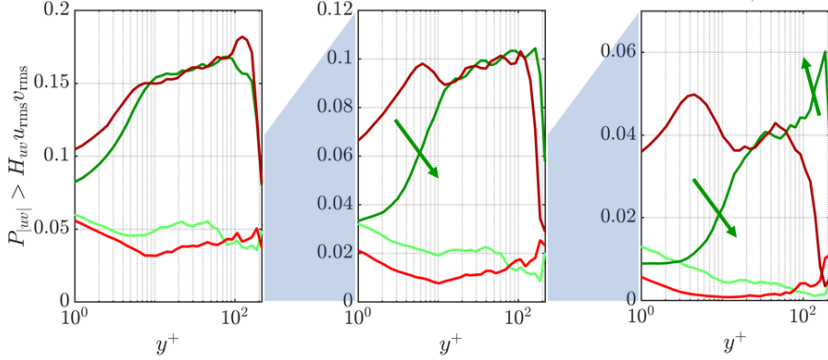


Figure 3.14: Probability of detecting different quadrants: light green Q1, dark green Q2, light red Q3, dark red Q4, for (from left to right) $H_{uv} = 0.5$, $H_{uv} = 1$, and $H_{uv} = 2$.

For $H_{uv} = 0.5$, which is a low threshold value for structure identification but still high enough to include only $\approx 30\%$ of the fluid volume, Q2 and Q4 have similar probabilities of occurrence, which progressively increase up to $y^+ \approx 100\%$ and rapidly decreases farther from the wall. Ejections are only slightly less common than sweeps in the near-wall region ($y^+ < 7\%$) at this intensity level. Increasing H_{uv} causes a reduction of the total probability of detecting events but also modifications of their relative abundance at different wall-normal distances. The two other quadrants, Q1 and Q3, are much less common than Q2 and Q4 overall in this kind of flow. For $H_{uv} = 1$, the total volume fraction included in intense events is $\approx 20\%$, and ejections become even rarer in the near-wall region than sweeps. In addition, the region where ejections are less common than sweep expand farther from the wall, up to $y^+ \approx 10\%$. This trend continues for higher values of the threshold. For $H_{uv} = 2$, uv events account for $\approx 10\%$ of the total volume. Ejections of this intensity are rarer than sweeps up to $y^+ \approx 20\%$, while the highest probably of sweep detection is at $y^+ \approx 5\%$. As very intense sweeps (positive fluctuations of the wall-normal velocity) are more likely than ejections near the wall, ejections (negative fluctuations of the wall-normal velocity) become more likely than sweeps approaching the boundary-layer edge. These results are intuitively related to the two different constraints on turbulent fluctuations imposed by the wall, on the one hand, and the presence of the laminar region, on the other hand.

Figure 3.15 illustrates the probability of occurrence of the four quadrants on the suction and pressure sides at the same streamwise location, $x/c = 0.8$, for very intens events ($H_{uv} = 2$). The adverse pressure gradient on the suction side is already relatively intense at this location, resulting in $\beta = 6$, and the Reynolds numbers based on the momentum thickness and friction velocities

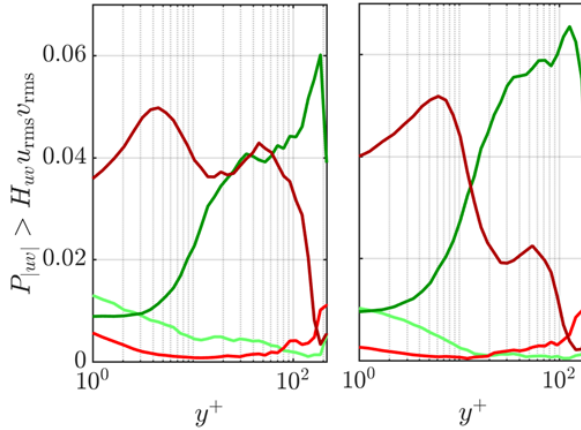


Figure 3.15: Probability of detecting different quadrants: light green Q1, dark green Q2, light red Q3, dark red Q4, for (left) APG and (right) ZPG.

are $Re_\theta = 1124$ and $Re_\tau = 226$. On the pressure side, the mild favourable pressure gradient results in $\beta \approx -0.1$, and lower Reynolds numbers $Re_\theta = 460$ and $Re_\tau = 185$. Note that β does not uniquely determine the flow properties (Bobke *et al.* 2017) on the suction side. A qualitative comparison between these two locations can nevertheless clarify the main effects of a strong APG on the flow. The probabilities of the four quadrants are in good agreement in the near-wall region, *i.e.* below $y^+ \approx 5$, where Q2 are much more likely than Q4, and, interestingly, immediately before the boundary-layer edge, where Q4 become more likely than Q2. In the intermediate region above $y^+ \approx 10$ and below $y^+ \approx 100$, there are interesting differences between the two flows. The total probability of detection is similar, but ejections are more common than sweeps in the zero-pressure-gradient case because the probability of sweeps rapidly decreases outside the near-wall region. Under this perspective, the zero-pressure-gradient boundary layer is more similar to internal flows than the case with strong APG.

Pressure-gradient effects are also apparent in the contribution to the mean wall-normal convection, which is present in boundary layers in general because of the streamwise development of the flow and it is strongly enhanced by adverse pressure gradients. Figure 3.16 shows the fractional contribution to the wall-normal velocity component, V_{uv}^+ , defined as in the study on the secondary flow in ducts:

$$V_{uv} = \frac{\mathcal{V}_{uv}}{\mathcal{V}} \int \tilde{v} \delta_{uv} d\mathcal{V}, \quad (3.9)$$

and scaled in viscous units. In this expression, \mathcal{V} is the total volume, \tilde{v} is the wall-normal instantaneous velocity component, \mathcal{V}_{uv} is the volume occupied

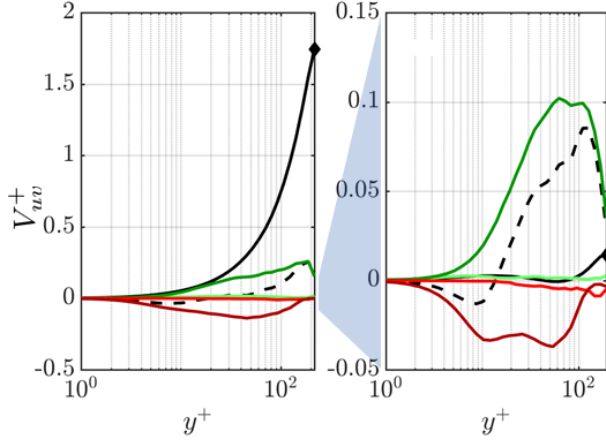


Figure 3.16: Contribution, solid line is the mean, dashed line is the total contribution, and Probability of detecting different quadrants: light green Q1, dark green Q2, light red Q3, dark red Q4, for (left) APG and (right) ZPG.

by uv events, and δ_{uv} is 1 if condition (3.8) is fulfilled and 0 otherwise. The contribution of each quadrant is defined similarly, with δ_{uv} equal to 0 or 1 depending on the velocity sign.

On both pressure and suction sides, the total contribution from all quadrants is negative up to $y^+ \approx 10$, where sweeps are more common than ejections, and positive for higher wall-normal distances, when ejections are more the most likely event. However, over the suction side, the contributions from ejections and sweeps have similar intensities, resulting in relatively low values of V_{uv} with respect to the mean V . On the other hand, over the pressure side, the contribution from ejections is significantly more intense than that from sweeps above $y^+ \approx 20$, resulting in a total contribution from intense events V_{uv} higher than the mean V .

3.3. Turbulent structures and time tracking

The development of the in-situ adaptor described in [Paper 14](#) aims at facilitating post-processing tasks such as flow visualization and also at enabling data analyses which would be too storage-intensive to be practical. One such analysis is time tracking of coherent structures, which requires high temporal resolution to be effective and long sampling to obtain statistically significant results. In most cases, these two constraints lead to excessive storage requirements to perform time tracking as standard post-processing. In the framework of the “In-Situ Big Data Analysis for Flow and Climate Simulations” consortium, Miguel Zavala (PDC, KTH - Royal Institute of Technology) developed a new time-tracking

algorithm using the in-situ adaptor and the VTK library, which was tested on the case of a square duct at centreplane $Re_\tau = 180$. In-situ analysis converts storage requirements into additional computational cost and memory usage, which, in the case of structure time tracking, are directly related to the sampling frequency, f . Note that the tracking is based on a collision-detection algorithm that compares structures in two flow fields separated by a certain sampling time interval, Δt^* , and $f = \Delta t / \Delta t^*$ denotes the ratio between the simulation time step, Δt , and Δt^* . In the safest but most expensive configuration, Δt and Δt^* coincide, so that $f = 1$.

For any structures already existing in the domain at a given time step, three possible interactions can occur: 1) if a structure corresponds to one structure in the following time step, it has simply propagated in the domain; 2) if multiple structures correspond to only one structure in the following time step, merging has occurred; and 3) if a structure corresponds to multiple structures in the following time step, splitting has occurred. In addition, if a structure has no correspondent in the next time step, it has disappeared, and structures in a new time step that do not correspond to structures in the previous time step have just been created. A too low sampling frequency would result in any of the possible interactions between structures to be misidentified as structures disappearing (instead of merging) or being created (instead of propagating or splitting). The average rates at which intense events interact, appear, or disappear in the domain are constants for statistically stationary solutions and should, in principle, not depend on the sampling frequency.

To assess the impact of the sampling frequency on the results of the tracking algorithm, we show in Figure 3.17 the averaged probabilities for structures in a time step to be the result of propagation (P_P), merging (P_M), splitting (P_S), or nucleating as a new structure (P_N), as functions of the sampling frequency, f . We observed that the merging and splitting rates, as well as that of nucleation of new structures, decrease as the sampling frequency increases up to 1, *i.e.* when the time tracking is performed each simulation time step (Figure 3.17). This result implies that time tracking needs to be performed with the highest possible time resolution, *i.e.* the same as that of the simulation. This condition leads to a considerable computational cost, and it is a surprisingly strict constraint because the simulation time step is much shorter than the viscous time unit, which is the characteristic time scale relevant for physical phenomena. Furthermore, Lozano-Durán & Jiménez (2014) reported that for their observable a sampling interval larger than the viscous time was sufficient. Further analyses are required to determine the sampling-frequency effects on statistical quantities such as the average lifetime, or what kind of structures are responsible for this sensitivity to time resolution.

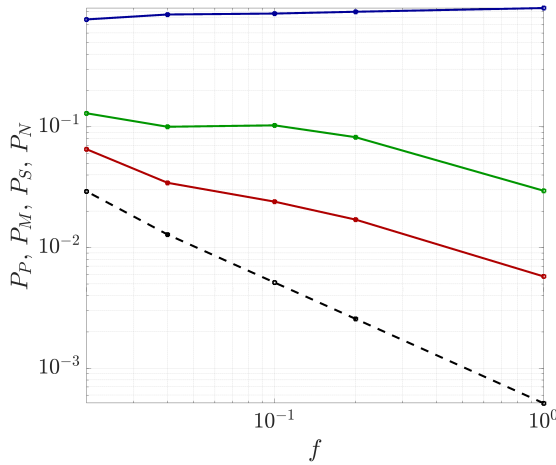


Figure 3.17: Impact of the sampling frequency, f , on the probabilities of a structure to be classified as the result of propagation (P_P , blue line), merging (P_M green line), splitting (P_S , red line), or as a new structure (P_N , black dashed line). Note that $P_P + P_M + P_S + P_N = 1$.

CHAPTER 4

Conclusions and Outlook

In this chapter, the main results obtained in the project are summarized and possible directions for future studies are discussed.

4.1. Control strategies

We studied various combinations of uniform blowing and suction applied to a NACA4412 airfoil at $Re_c = 200,000$ and $Re_c = 400,000$ with high-fidelity numerical simulations, and a wider range of conditions using RANS simulations, and we described in details control effects on wall turbulence and on aerodynamic properties, including an evaluation of the actuation cost. It is worth mentioning that, although these Reynolds numbers are obviously lower than those encountered in full-scale commercial airplanes, $Re_c = 400,000$ is the same as *e.g.* that in the study by Albers *et al.* (2019) on a different control strategy and the highest considered for LES of airfoil with control. In addition, it is relatively close to that reached in experiments and smaller aircraft such as gliders and unmanned aerial vehicles (UAV). Therefore, the present results are relevant for aeronautics applications.

The comparison between control effects on the airfoil suction and pressure sides, *i.e.* under different pressure-gradient conditions, showed significant differences. In particular, the adverse-pressure-gradient boundary layer over the suction side is more sensitive to blowing and suction, in the sense that the increase or decrease of boundary-layer thickness, as well as that of mean wall-normal convection and turbulent fluctuations are more significantly amplified. These effects also influence the mechanisms that generate skin friction, as shown using both the FIK and RD decompositions, and the distributions of energy in different scales, as shown by spectral analysis and empirical mode decomposition.

An obvious consideration inspired by these findings is that it can be challenging to extrapolate results obtained for ZPG boundary layer or channel flow to cases with non-uniform adverse pressure gradients, thus we highlight the importance of considering boundary layers subjected to pressure gradients in studies on control, if the control is ultimately aimed at aerodynamic flows. Because of the complex interactions between inner- and outer-region dynamics,

this principle equally applies to both predetermined and closed-loop control strategies.

We identified blowing applied to the pressure side as the most promising configuration for improving aerodynamic efficiency (at moderate angles of attack). Uniform suction and uniform blowing applied to the suction side can also give higher aerodynamic efficiency, depending on the relative proportion of skin friction and pressure drag, which is determined by the Reynolds number. However, when the actuation cost is considered, only blowing applied to the pressure side yields net-energy saving. Furthermore, this configuration appears to be consistently beneficial over a relatively broad range of Reynolds numbers.

A few interesting points have been deliberately neglected during this project, mainly because of time constraints. We did not thoroughly investigate the reason why APG TBLs are more sensitive to blowing and suction effect. An intuitive explanation is that these control strategies act on the wall-normal convection, which is already stronger than in ZPG TBLs, but the increase or decreases of wall-normal convection still needs to be connected with other effects *e.g.* excitation or attenuation of turbulent fluctuations. A related topic is how this control interacts with history effects.

In this work, we considered both the FIK and RD decompositions. Although the RD decomposition has been formulated specifically to be easier to interpret than the FIK decomposition, the same qualitative trends have been observed using both approaches in every circumstance without major differences. Whether one or the other is more effective to explain skin-friction generation ultimately depends on what they can be employed for, but both of them tend to be used for qualitative discussions and describing the data rather than modelling or predictions. This circumstance makes somewhat difficult to clearly assess which one is most suitable. We believe that it is more appropriate to compare both decompositions on a broader set of data in the future.

Optimization of control amplitude or location has not been considered. Experiments carried using RANS simulations showed, unsurprisingly, that for control strategies beneficial for the aerodynamic efficiency, the “optimal” configuration is to extend the control region as much as possible. Optimization can be used in scenarios where the total control surface is limited, for instance in series of parallel stripes, as in the study carried out by Mahfoze *et al.* (2019). This approach would probably be very beneficial for industrial applications, but we believed that a uniform control region was more appropriate to study interactions between control and pressure gradients without additional effects.

4.2. Coherent structures

We examined intense Reynolds-stress events in turbulent ducts with square and rectangular cross-sections and in the boundary layers developing around a NACA4412 wing section, which was also considered in the studies on control. The majority of previous research efforts on this topic aimed to discover the fundamental dynamical processes in wall-bounded turbulent flows and are

focused on scaling properties and the role of different types of instantaneous structures, as in the work by Lozano-Durán *et al.* (2012). Our goal was to investigate the connection between these structures and specific phenomena such as the secondary flow of Prandtl's second kind and pressure-gradients effects. To this end, we analysed the structure dimensions, intensity, and contributions to the mean flow.

Comparing channels and ducts, we found that the structures' geometrical properties are affected by the presence of the corner and the additional constraint represented by the vertical walls, which is perhaps not particularly surprising. However, their contributions to the secondary flow are negligible, both in the centre and the corner regions. In the centre region, the contributions to the mean vertical velocity from coherent structures are in very good agreement between channel and duct. In the corner region, intense events are less likely to occur, but their contributions are still unrelated to the secondary flow. Overall, the most significant differences between channel and ducts are found in the contributions from the portion of flow complementary to intense events.

Studying coherent structures in boundary layers, we found significant differences between adverse- and zero-pressure-gradient cases, both in their distribution in space and connection to the mean flow. The adverse pressure gradient reduces the dimensions and the occurrence of very large structures attached to the wall and the proportion of ejections in the quadrant analysis. In zero-pressure-gradient boundary layers, as in channels or ducts, ejections are dominant. In these cases, the intense-event contribution to wall-normal convection is positive, and the mean flow is the result of a balance between coherent structures and the complementary portion of the flow. In adverse-pressure-gradient boundary layers, the contribution to wall-normal convection from coherent structures is much lower than the mean and even less intense than that in zero-pressure-gradient boundary layers near the wall.

For the control strategies that we considered, *i.e.* uniform blowing, uniform suction, and body-force damping, mean effects are more relevant than those on coherent structures. Under this perspective, similarly to what was observed comparing channel and duct flows, we found that intense events tend to have relatively universal properties and they are similar between controlled and uncontrolled cases. On the one hand, this fact corroborates their relevance for fundamental research but, on the other hand, makes it difficult to investigate secondary effects through their properties.

Overall, our experience studying intense events confirms the warning given by Hussain (1986) about the risk of getting lost in details when performing this kind of analysis. The reason for detecting and describing instantaneous structures is to isolate a certain portion of the flow that is relevant to explain a phenomenon, but this premise is difficult to verify. However, our study cannot exclude that better approaches will be more successful, and there are many aspects that we did not tackle.

Direct contributions to the mean flow are a very simplified way to assess the relevance of certain instantaneous flow features. Still, formulating a consistently better measure is not a trivial task. On the one hand, the quadrant analysis was originally aimed at investigating structures relevant to generate Reynolds stresses, and intense events obviously contribute to fluctuations by a larger amount, given their volume fraction, relatively to the rest of the flow. However, the Reynolds-stress fluxes are relevant, not their intensity directly (Jiménez 2016), so Reynolds-stress contributions are not necessarily more significant than contributions to the mean. On the other hand, data-analysis approaches such as proper orthogonal decomposition (POD), dynamic mode decomposition (DMD), and resolvent analysis, designed to identify the most relevant coherent features to reconstruct the flow, do not retain information about instantaneous structures. We did not investigate how these different approaches are related or how to optimize structure detection.

A natural step forward in the study of coherent structures defined as regions of flow where certain conditions are fulfilled is to examine their evolution in time. However, it is challenging from a technical perspective because of the high computational costs and storage requirements. Lozano-Durán & Jiménez (2014) carried out this analysis in turbulent channel flows using an ad-hoc implementation, but it has not become of common use in the following years. This fact is partly due to technical difficulties and partly to the more fundamental question of how to interpret its results. The in-situ approach is probably the most promising to make time tracking in high-fidelity simulations more viable and to explore its effectiveness in cases with more complex geometries. We did some initial effort in this direction, but additional work is required in the future.

Acknowledgements

Perhaps inevitably, there are many decisions in the last four years that I would change. The choice of my supervisors, however, is not one of them. We have worked well together during this project, and I will always be grateful for their mentorship and help. I have become familiar with many topics and techniques relevant to our discipline. I have become a better researcher, a more effective team player, and even a (slightly) less terrible writer. All of this has been possible, not in a small portion, for their merit. So, thank you, Philipp! Thank you, Ricardo! I believe you have done a good job :)

I would also like to thank all the colleagues who contributed to obtaining the results described in this thesis. I am well aware that this project would have been very different and more difficult for me without them. I did my best to acknowledge their work properly in this document, and I feel in debt with each of them.

Many people who have not been mentioned yet also helped me with exciting discussions, making appropriate jokes in dire moments, or with their mere presence, which has been consistently proven of great aid in finding bugs in codes. In particular, I would like to mention my office mates, Luca de Vincentiis, Pierluigi Morra, and Kristina Đurović, as well as Alvaro Tanarro.

Finally, I would like to thank my parents for their great support and many friends who helped indirectly, answering questions on life, the universe, and everything.

Financial support for this project was provided by the Swedish Foundation for Strategic Research (project “In-Situ Big Data Analysis for Flow and Climate Simulations”), and the Knut and Alice Wallenberg Foundation. Participation to the third and fourth turbulence workshops in Madrid was supported by the Coturb program of the European Research Council. Travels were supported by the foundation Petersohns Minne and the ÅForsk Foundation. Numerical simulations were performed on resources provided by the Swedish National Infrastructure for Computing (SNIC) and within the project CWING on the national supercomputer Cray XC40 Hazel Hen at the High Performance Computing Center Stuttgart (HLRS), Germany.

Bibliography

- DEL ÁALAMO, J., JIMÉNEZ, J., ZANDONADE, P. & MOSER, R. 2006 Self-similar vortex cluster in the turbulent logarithmic region. *J. Fluid Mech.* **561**, 329–358.
- ALBERS, M., MEYSONNAT, P. & SCHRÖDER, W. 2019 Actively reduced airfoil drag by transversal surface waves. *Flow Turbul. Combust.* **102**.
- BECK, N., LANDA, T., SEITZ, A., BOERMANS, L., LIU, Y. & RADESPIEL, R. 2018 Drag Reduction by Laminar Flow Control. *Energies* **11** (1), 252.
- BILLS, A., SRIPAD, S., FREDERICKS, W. L., SINGH, M. & VISWANATHAN, V. 2020 Performance metrics required of next-generation batteries to electrify commercial aircraft. *ACS Energy Lett.* **5** (2), 663–668.
- BISSET, D., HUNT, J. & ROGERS, M. 2002 The turbulent/non-turbulent interface bounding a far wake. *J. Fluid Mech.* **451**, 383–410.
- BOBKE, A., VINUESA, R., ÖRLÜ, R. & SCHLATTER, P. 2017 History effects and near-equilibrium in adverse-pressure-gradient turbulent boundary layers. *J. Fluid Mech.* **820**, 667–692.
- BRYNJELL-RAHKOLA, M. 2017 *Studies on instability and optimal forcing of incompressible flows*. PhD Thesis, KTH Royal Institute of Technology, Sweden.
- CHAUHAN, K., PHILIP, J., DE SILVA, C. M., HUTCHINS, N. & MARUSIC, I. 2014 The turbulent/non-turbulent interface and entrainment in a boundary layer. *J. Fluid Mech.* **742**, 119–151.
- CHOI, H. & MOIN, P. 2012 Grid-point requirements for large eddy simulation: Chapman’s estimates revisited. *Phys. Fluids* **24**, 011702.
- CHOI, H., MOIN, P. & KIM, J. 1994 Active turbulence control for drag reduction in wall-bounded flows. *J. Fluid Mech.* **262**, 75–110.
- CHONG, M., PERRY, A. & CANTWELL, B. 1990 A general classification of three-dimensional flow fields. *Phys. Fluids* **2**, 765–777.
- CUCITORE, R., QUADRI, M. & BARON, A. 1999 On the effectiveness and limitations of local criteria for the identification of a vortex. *Eur. J. Mech. B* **18**, 261–282.
- DONG, S., KARNIADAKIS, G. E. & CHRYSOSTOMIDIS, C. 2014 A robust and accurate outflow boundary condition for incompressible flow simulations on severely-truncated unbounded domains. *J. Comput. Phys.* **261**, 83–105.
- EITEL-AMOR, G., ÖRLÜ, R. & SCHLATTER, P. 2014 Simulation and validation of a spatially evolving turbulent boundary layer up to $Re_\theta = 8300$. *Int. J. Heat Fluid Flow* **47**, 57–69.
- EL KHOURY, G., SCHLATTER, P., NOORANI, A., BRETHOUWER, G. & JOHANSSON,

- A. V. 2013 Direct Numerical Simulation of Turbulent Pipe Flow at Moderately High Reynolds Numbers. *Flow Turbul. Combust.* **91**, 475–495.
- FISCHER, P., LOTTES, J. & KERKEMEIER, S. 2008 Nek5000: Open source spectral element CFD solver. Available at: <http://nek5000.mcs.anl.gov>.
- FISCHER, P. F. 1997 An overlapping Schwarz method for spectral element solution of the incompressible Navier-Stokes equations. *J. Comput. Phys.* **133**, 84–101.
- FRISCH, U. 1995 *Turbulence*. Cambridge University Press.
- FUKAGATA, K., IWAMOTO, K. & KASAGI, N. 2002 Contribution of reynolds stress distribution to the skin friction in wall-bounded flows. *Phys. Fluids* **14**, 73–76.
- GAVRILAKIS, S. 2019 Post-transitional periodic flow in a straight square duct. *J. Fluid Mech.* **859**, 731–753.
- GUPTA, A. K., LAUFER, J. & KAPLAN, R. E. 1971 Spatial structure in the viscous sublayer. *J. Fluid Mech.* **50** (3), 493–512.
- HOLZMANN, T. 2018 *Mathematics, Numerics, Derivations and OpenFOAM(R)*. Holzmann CFD.
- HOSSEINI, S. M., VINUESA, R., SCHLATTER, P., HANIFI, A. & HENNINGSON, D. S. 2016 Direct numerical simulation of the flow around a wing section at moderate Reynolds number. *Int. J. Heat Fluid Flow* **61**, 117–128.
- HUNT, J. C. R., WRAY, A. A. & MOIN, P. 1988 Eddies, streams and convergence zones in turbulent flows. *Center for Turbulence Research, Proceedings of the Summer Program 1988* pp. 193–208.
- HUSSAIN, F. 1986 Coherent structures and turbulence. *J. Fluid Mech.* **173**, 303–356.
- JEONG, J. & HUSSAIN, F. 1995 On the identification of a vortex. *J. Fluid Mech.* **285**, 69–94.
- JIMÉNEZ, J. 2016 Optimal fluxes and reynolds stresses. *J. Fluid Mech.* **809**, 585–600.
- JIMÉNEZ, J. 2018 Coherent structures in wall-bounded turbulence. *J. Fluid Mech.* **P1**.
- JIMÉNEZ, J. & MOIN, P. 1991 The minimal flow unit in near-wall turbulence. *J. Fluid Mech.* **225**, 214–240.
- KAMETANI, Y., FUKAGATA, K., ÖRLÜ, R. & SCHLATTER, P. 2015 Effect of uniform blowing/suction in a turbulent boundary layer at moderate Reynolds number. *Int. J. Heat Fluid Flow* **55**, 134–142.
- KLINE, S. J., REYNOLDS, W. C., SCHRAUB, F. A. & RUNSTADLER, P. W. 1967 The structure of turbulent boundary layers. *J. Fluid Mech.* **30** (4), 741–773.
- LEE, D., FAHEY, D., SKOWRON, A., ALLEN, M., BURKHARDT, U., CHEN, Q., DOHERTY, S., FREEMAN, S., FORSTER, P., FUGLESTVEDT, J., GETTELMAN, A., DE LEÓN, R., LIM, L., LUND, M., MILLAR, R., OWEN, B., PENNER, J., PITARI, G., PRATHER, M., SAUSEN, R. & WILCOX, L. 2021 The contribution of global aviation to anthropogenic climate forcing for 2000 to 2018. *Atmospheric Environment* **244**, 117834.
- LEE, M. & MOSER, R. 2015 Direct numerical simulation of turbulent channel flow up to $re_\tau \approx 5200$. *J. Fluid Mech.* **774**, 395–415.
- LEMOULT, G., SHI, L., AVILA, K., JALIKOP, S. V., AVILA, M. & B., H. 2016 Directed percolation phase transition to sustained turbulence in couette flow. *Nature Physics* **12**, 254–258.
- LOZANO-DURÁN, A., FLORES, O. & JIMÉNEZ, J. 2012 The three-dimensional structure of momentum transfer in turbulent channels. *J. Fluid Mech.* **694**, 100–130.

- LOZANO-DURÁN, A. & JIMÉNEZ, J. 2014 Time-resolved evolution of coherent structures in turbulent channels: characterisation of eddies and cascades. *J. Fluid Mech.* **759**, 432–471.
- MADAY, Y. & PATERA, A. 1984 Spectral element methods for the navier-stokes equations. *A.K. Noor (Ed.), State of the Art Surveys in Computational Mechancis, ASME, France*. pp. 71–143.
- MAHFOZE, O. A., MOODY, A., WYNN, A., WHALLEY, R. D. & LAIZET, S. 2019 Reducing the skin-friction drag of a turbulent boundary-layer flow with low-amplitude wall-normal blowing within a bayesian optimization framework. *Phys. Rev. Fluids* **4**, 094601.
- MENTER, F. 1993 Zonal Two Equation k-w Turbulence Models For Aerodynamic Flows. In *23rd Fluid Dynamics, Plasmadynamics, and Lasers Conference*. Orlando,FL,U.S.A.: American Institute of Aeronautics and Astronautics.
- MODESTI, D., PIROZZOLI, S., ORLANDI, P. & GRASSO, F. 2018 Turbulence and secondary motions in square duct flow. *J. Fluid Mech.* **847**, R1.
- MOISY, F. & JIMÉNEZ, J. 2004 Geometry and clustering of intense structures in isotropic turbulence. *J. Fluid Mech.* **513**, 111–133.
- NAGAOSA, R. & HANDLER, R. A. 2003 Statistical analysis of coherent vortices near a free surface in a fully developed turbulence. *J. Fluid Mech.* **15**, 375–394.
- NEGI, P., VINUESA, R., HANIFI, A., SCHLATTER, P. & HENNINGSON, D. 2018 Unsteady aerodynamic effects in small-amplitude pitch oscillations of an airfoil. *Int. J. Heat Fluid Flow* **72**, 378–391.
- OFFERMANS, N. 2019 *Aspect of adaptive mesh refinement in the spectral element method*. PhD Thesis, KTH Royal Institute of Technology, Sweden.
- OFFERMANS, N., MARIN, O., SCHANEN, M., GONG, J., FISCHER, P. & SCHLATTER, P. 2016 On the strong scaling of the spectral element solver nek5000 on petascale systems. In *Proceedings of the 2016 Exascale Applications and Software Conference (EASC2016)*, pp. 1–10.
- PARK, J. & CHOI, H. 1999 Effects of uniform blowing or suction from a spanwise slot on a turbulent boundary layer flow. *Phys. Fluids* **11** (10), 3095.
- PATANKAR, S. V. & SPALDING, D. B. 1972 A spectral element method for fluid dynamics: laminar flow in a channel expansion. *Int. J. Heat Mass Transfer* **15** (10), 1787–1806.
- PATERA, A. T. 1984 A spectral element method for fluid dynamics: laminar flow in a channel expansion. *J. Comput. Phys.* **54**, 468–488.
- PINELLI, A., UHLMANN, M., SEKIMOTO, A. & KAWAHARA, G. 2010 Reynolds number dependence of mean flow structures in square duct turbulence. *J. Fluid Mech.* **644**, 107–122.
- PIROZZOLI, S., MODESTI, D., ORLANDI, P. & GRASSO, F. 2018 Turbulence and secondary motions in square duct flow. *J. Fluid Mech.* **840**, 631–655.
- RENARD, N. & DECK, S. 2016 A theoretical decomposition of mean skin friction generation into physical phenomena across the boundary layer. *J. Fluid Mech.* **790**, 339–367.
- SCHLATTER, P. & ÖRLÜ, R. 2012 Turbulent boundary layers at moderate Reynolds numbers: inflow length and tripping effects. *J. Fluid Mech.* **710**, 5–34.
- SCHLATTER, P., STOLZ, S. & KLEISER, L. 2004 LES of transitional flows using the approximate deconvolution model. *Int. J. Heat Fluid Flow* **25**, 549–558.

- STAUFFER, D. & AHARONY, A. 1994 *Introduction to Percolation Theory*. Boca Raton, Florida: CRC Press.
- STEVENSON, T. N. 1963 A law of the wall for turbulent boundary layers with suction or injection. *CoA Report Aero. No. 166*.
- STOLZ, S., ADAMS, N. A. & KLEISER, L. 2001 An approximate deconvolution model for large-eddy simulation with application to incompressible wall-bounded flows. *Phys. Fluids* **13**, 997.
- STROH, A., HASEGAWA, Y., SCHLATTER, P. & FROHNAPFEL, B. 2016 Global effect of local skin friction drag reduction in spatially developing turbulent boundary layer. *J. Fluid Mech.* **805**, 303–321.
- SUMITANI, Y. & KASAGI, N. 1995 Direct numerical simulation of turbulent transport with uniform wall injection and suction. *AIAA J.* **32**, 1220–1228.
- TANARRO, A., VINUESA, R. & SCHLATTER, P. 2020 Effect of adverse pressure gradients on turbulent wing boundary layers. *J. Fluid Mech.* **883**, A8.
- VINUESA, R., BOKE, A., ÖRLÜ, R. & SCHLATTER, P. 2016 On determining characteristic length scales in pressure-gradient turbulent boundary layers. *Phys. Fluids* **28**, 055101.
- VINUESA, R., NEGI, P., ATZORI, M., HANIFI, A., HENNINGSON, D. & SCHLATTER, P. 2018a Turbulent boundary layers around wing sections up to $Re_c = 1,000,000$. *Int. J. Heat Fluid Flow* **72**, 86–99.
- VINUESA, R., ROZIER, P. H., SCHLATTER, P. & NAGIB, H. M. 2014 Experiments and computations of localized pressure gradients with different history effects. *AIAA J.* **55**, 368–384.
- VINUESA, R., SCHLATTER, P. & NAGIB, H. M. 2018b Secondary flow in turbulent ducts with increasing aspect ratio. *Phys. Rev. Fluids* **3**, 054606.
- WALLACE, J. M., ECKELMAN, H. & BRODKEY, R. S. 1972 The wall region in turbulent shear flow. *J. Fluid Mech.* **54**, 39–48.
- WELLER, H., GREENSHIELDS, C., SANTOS, B., BAINBRIDGE, W. & JANSENS, M. 2019 OpenFOAM v7 | Patch Releases. Available at: <https://openfoam.org/news/v7-patch/>.
- YEUNG, P. K. & RAVIKUMAR, K. 2020 Advancing understanding of turbulence through extreme-scale computation: Intermittency and simulations at large problem sizes. *Phys. Rev. Fluids* **5**, 110517.

Part II

Papers

Summary of the papers

Paper 1

Turbulent boundary layers around wing sections up to $Re_c = 1,000,000$

Reynolds-number effects in the adverse-pressure-gradient (APG) turbulent boundary layer (TBL) developing on the suction side of a NACA4412 wing section are assessed in the present work. To this end, we analyze four cases at Reynolds numbers based on freestream velocity and chord length ranging from $Re_c = 100,000$ to $1,000,000$, all of them with 5° angle of attack. The results of four well-resolved large-eddy simulations (LESs) are used to characterize the effect of Reynolds number on APG TBLs subjected to approximately the same pressure-gradient distribution (defined by the Clauser pressure-gradient parameter β). Comparisons of the wing profiles with zero-pressure-gradient (ZPG) data at matched friction Reynolds numbers reveal that, for approximately the same β distribution, the lower-Reynolds-number boundary layers are more sensitive to pressure-gradient effects. This is reflected in the values of the inner-scaled edge velocity U_e^+ , the shape factor H , the components of the Reynolds-stress tensor in the outer region and the outer-region production of turbulent kinetic energy. This conclusion is supported by the larger wall-normal velocities and outer-scaled fluctuations observed in the lower- Re_c cases. Thus, our results suggest that two complementing mechanisms contribute to the development of the outer region in TBLs and the formation of large-scale energetic structures: one mechanism associated with the increase in Reynolds number, and another one connected to the APG. Future extensions of the present work will be aimed at studying the differences in the outer-region energizing mechanisms due to APGs and increasing Reynolds number.

Paper 2

Aerodynamic effects of uniform blowing and suction on a NACA4412 airfoil

We carried out high-fidelity large-eddy simulations (LES) to investigate the effects of uniform blowing and uniform suction on the aerodynamic efficiency of a NACA4412 airfoil at the moderate Reynolds number based on chord length and incoming velocity of $Re_c = 200,000$. We found that uniform blowing applied at the suction side reduces the aerodynamics efficiency, while uniform

suction increases it. This result is due to the combined impact of blowing and suction on skin friction, pressure drag and lift. When applied to the pressure side, uniform blowing improves aerodynamic efficiency. The Reynolds-number dependence of the relative contributions of pressure and friction to the total drag for the reference case is analysed via Reynolds-averaged Navier–Stokes (RANS) simulations up to $Re_c = 10,000,000$. The results suggest that our conclusions on the control effect can tentatively be extended to a broader range of Reynolds numbers.

Paper 3

Blowing and suction applied to non-uniform adverse-pressure-gradient boundary layers

We performed a detailed analysis of the effects of uniform blowing, uniform suction and body-force damping on the turbulent boundary layer developing around a NACA4412 airfoil. The flow over the suction and the pressure sides of the airfoil is subjected to a non-uniform adverse pressure gradient and a moderate favourable pressure gradient, respectively. We found that the changes in total skin-friction due to blowing and suction are not very sensitive to different pressure-gradient conditions or the Reynolds number. However, when blowing and suction are applied to an adverse-pressure-gradient (APG) boundary layer, their impact on properties such as the boundary layer thickness, the intensity of the wall-normal convection and turbulent fluctuations, are more pronounced. We employed the FIK decomposition (Fukagata *et al.*, *Phys. Fluids*, vol. 14, 2002, pp. 73–76) for the first time to study the interaction between intense adverse pressure gradient and these control strategies. We found that the control modifies skin-friction contributions differently in adverse-pressure-gradient and zero-pressure-gradient boundary layers. In particular, the control strategies modify considerably both the streamwise-development and the pressure-gradient contributions, which have high magnitude when a strong adverse pressure gradient is present. Overall, our results show that it is not possible to simply separate pressure-gradient and control effects, a fact to take into account in future studies on control design in practical applications.

Paper 4

Investigation of Blowing and Suction for Turbulent Flow Control on Airfoils

An extensive parametric study of turbulent boundary layer control on airfoils via uniform blowing or suction is presented. The control is applied on either suction or pressure side of several 4-digit NACA-series airfoils. The considered parameter variations include angle of attack, Reynolds number, control intensity, airfoil camber and airfoil thickness. Two comprehensive metrics, designed to account for the additional energy required by the control, are introduced to evaluate the net aerodynamic performance enhancements. The study confirms previous findings for suction side boundary layer control and demonstrates the interesting potential of blowing on the pressure side under various conditions,

which achieves a maximum total net drag saving of 14% within the considered parameter space. The broad parameter space covered by the presented Reynolds-average Navier-Stokes (RANS) simulations allows for more general conclusions than previous studies and can thus provide guidelines for the design of future detailed experimental or numerical studies on similar boundary layer control schemes.

Paper 5

Decomposition of the mean friction drag in adverse-pressure-gradient turbulent boundary layers

In the present study, we exploit the Renard-Deck identity [“A theoretical decomposition of mean skin friction generation into physical phenomena across the boundary layer”, *J. Fluid Mech.* **790**, 339–367 (2016)] to decompose the mean friction drag in adverse-pressure-gradient turbulent boundary layers (APG-TBLs) into three components, associated with viscous dissipation, turbulence kinetic energy production, and spatial growth of the flow, respectively. We consider adverse-pressure-gradient turbulent boundary layers developing on flat-plates and airfoils, with friction Reynolds numbers in the range $200 < Re_\tau < 2000$, and with Rotta-Clauser pressure-gradient parameters (β) ranging from 0 to 50. The effects of Reynolds number, adverse pressure gradient, and the pressure-gradient-history on the contributing components are individually investigated, and special attention is paid to the comparisons with zero-pressure-gradient turbulent boundary layers (ZPG-TBLs). Our results indicate that the inner peaks of the dissipation and production terms are located at $y^+ \approx 6$ and $y^+ \approx 16.5$, respectively, and their outer peaks scale with the 99% boundary-layer thickness (δ_{99}), *i.e.* $y/\delta_{99} \approx 0.7$ and $y/\delta_{99} \approx 0.53$, respectively. These results are independent of the friction Reynolds number, the magnitude of β and its development history. Moreover, the spatial-growth component is negative in the investigated APG-TBLs, and its magnitude increases with β .

Paper 6

Friction drag decompositon of the turbulent boundary layers on a NACA4412 airfoil under uniform blowing and suction

The application of control strategies on distinct canonical wall-bounded turbulent flows, such as periodic channel and zero- or adverse-pressure-gradient boundary layers, raises the question of how to describe control effects consistently for different reference cases. Renard and Deck (*J. Fluid Mech.*, **790**, 2016, pp. 339–367) proposed a skin-friction decomposition based on turbulent-kinetic-energy budget, which we employ in this paper for the first time to investigate the effects of uniform blowing and uniform suction applied to a NACA4412 airfoil in combination with the empirical-mode decomposition (EMD). We found that

uniform blowing increases the skin-friction contribution related to turbulent-kinetic-energy production, slightly decreases that related to viscous dissipation, and significantly decreases the contribution related to flow development. Uniform suction has opposite effects. By inspecting the contributions at different wall-normal distances, it is shown that blowing and suction have different effects on the flows in different layers. In particular, blowing inhibits the skin-friction generation near the wall, but it increases it in the outer regions, while uniform suction does the opposite. It is also found that, in both control and reference cases, the locations of the inner peak of the contributions scale in viscous units, while that of the outer peak scale in outer units. The EMD unveils that this control modifies the small- and large-scales turbulent structures, but it has negligible effects on cross-scale interactions.

Paper 7

Design and setup of a wing model in the Minimum-Turbulence-Level wind tunnel

A reinforced fiber-glass model of a NACA 4412 wing profile is designed and set-up in the Minimum-Turbulence-Level (MTL) wind-tunnel facility at KTH Royal Institute of Technology (Sweden), aiming to complement the high-fidelity numerical work performed by our research group on the same airfoil, including direct numerical simulations (DNS) and large-eddy simulations (LES). The model has 65 pressure taps, and the set-up includes two mounting panels designed to allow for particle image velocimetry (PIV) and hot-wire anemometry (HWA) measurements of the boundary layer on the model (both to be performed in a future campaign). In this first experimental campaign pressure scans are carried out at four angles of attack of interest (0, 5, 10 and 12 degrees), and at four different Reynolds numbers based on chord length and inflow velocity (200,000, 400,000, 1,000,000 and 1,640,000). The experimental data is then compared with reference high-fidelity and $k - \omega$ SST RANS simulations. The preliminary results show an excellent agreement with the reference numerical data, specially at the moderate angles of attack.

Paper 8

Characterization of turbulent coherent structures in square duct flow

This work is aimed at a first characterization of coherent structures in turbulent square duct flows. Coherent structures are defined as connected components in the domain identified as places where a quantity of interest (such as Reynolds stress or vorticity) is larger than a prescribed non-uniform threshold. Firstly, we qualitatively discuss how a percolation analysis can be used to assess the effectiveness of the threshold function, and how it can be affected by statistical uncertainty. Secondly, various physical quantities that are expected to play an important role in the dynamics of the secondary flow of Prandtl's second kind are studied. Furthermore, a characterization of intense Reynolds-stress events in square duct flow, together with a comparison of their shape for analogous events in channel flow at the same Reynolds number, is presented.

Paper 9

Intense Reynolds-stress events in turbulent ducts

The aim of the present work is to investigate the role of intense Reynolds shear-stress events in the generation of the secondary flow in turbulent ducts. We consider the connected regions of flow where the product of the instantaneous fluctuations of two velocity components is higher than a threshold based on the long-time turbulence statistics, in the spirit of the three-dimensional quadrant analysis proposed by Lozano-Durán *et al.* (*J. Fluid Mech.*, vol. 694, 2012, pp. 100–130). We examine both the geometrical properties of these structures and their contribution to the mean in-plane velocity components, and we perform a comparison with turbulent channel flow at similar Reynolds number. The contribution to a certain mean quantity is defined as the ensemble average over the detected coherent structures, weighted with their own occupied volume fraction. In the core region of the duct, the contribution of intense events to the wall-normal component of the mean velocity is in very good agreement with that in the channel, despite the presence of the secondary flow in the former. Additionally, the shapes of the three-dimensional objects do not differ significantly in both flows. In the corner region of the duct, the proximity of the walls affects both the geometrical properties of the coherent structures and the contribution to the mean component of the vertical velocity. However, such contribution is less relevant than that of the complementary portion of the flow not included in such objects. Our results show that strong Reynolds shear-stress events are affected by the presence of a corner but, despite the important role of these structures in the dynamics of wall-bounded turbulent flows, their contribution to the secondary flow is relatively low, both in the core and in the corner.

Paper 10

Coherent structures in turbulent boundary layers over an airfoil

This preliminary study is concerned with the identification of three-dimensional coherent structures, defined as intense Reynolds-stress events, in the turbulent boundary layer developing over the suction side of a NACA4412 airfoil at a Reynolds number based on the chord length and the incoming velocity of $Re_c = 200,000$. The scientific interest for such flows originates from the non-uniform adverse pressure gradient that affects the boundary-layer development. Firstly, we assess different methods to identify the turbulent-non-turbulent interface, in order to exclude the irrotational region from the analysis. Secondly, we evaluate the contribution of the considered coherent structures to the enhanced wall-normal velocity, characteristic of adverse pressure gradients. Our results show that it is necessary to limit the detection of coherent structures to the turbulent region of the domain, and that the structures reveal qualitative differences between the contributions of intense events to the wall-normal velocity in

adverse-pressure-gradient and zero-pressure-gradient turbulent boundary layers.

Paper 11

Control effects on coherent structures in a non-uniform adverse-pressure-gradient boundary layer

In the present report, we examine the effects of three control strategies, namely uniform blowing, uniform suction, and body-force damping, on the intense Reynolds-stress events in the turbulent boundary layer (TBL) developing on the suction side of a NACA4412 airfoil. This flow is subjected to a non-uniform adverse pressure gradient (APG), which substantially modifies its turbulence statistics with respect to a zero-pressure-gradient (ZPG) boundary layer, and it also changes how control strategies affect the flow. We found that the strong APG results in intense events that are shorter and more often detached from the wall than in ZPG TBLs, and it also modified the contributions of different quadrants. Ejections remain the most relevant structures, but sweeps become more important than in ZPG TBLs, a fact that results in a lower contribution to the wall-normal vertical velocity from intense events. We found that control effects are relatively less important on intense events than on the turbulent statistics. Uniform blowing has an impact similar to that of an even more intense APG, while uniform suction has more complex effects, most likely due to the particular behavior of the wall-normal velocity component near the wall. Body-force damping also reduces the probability of occurrence of very-large attached structures and, not surprisingly, that of intense events in the proximity of the actuation region.

Paper 12

Notes on Percolation Analysis of Sampled Scalar Fields

Percolation analysis is used to explore the connectivity of randomly connected infinite graphs. In the finite case, a closely related percolation function captures the relative volume of the largest connected component in a scalar field's superlevel set. While prior work has shown that random scalar fields with little spatial correlation yield a sharp transition in this function, little is known about its behavior on real data. In this work, we explore how different characteristics of a scalar field – such as its histogram or degree of structure – influence the shape of the percolation function. We estimate the critical value and transition width of the percolation function, and propose a corresponding normalization scheme that relates these values to known results on infinite graphs. In our experiments, we find that percolation analysis can be used to analyze the degree of structure in Gaussian random fields. On a simulated turbulent duct flow data set we observe that the critical values are stable and consistent across time. Our normalization scheme indeed aids comparison between data sets and relation to infinite graphs.

Paper 13

Distributed Percolation Analysis for Turbulent Flows

Percolation analysis is a valuable tool to study the statistical properties of turbulent flows. It is based on computing the percolation function for a derived scalar field, thereby quantifying the relative volume of the largest connected component in a superlevel set for a decreasing threshold. We propose a novel memory-distributed parallel algorithm to finely sample the percolation function. It is based on a parallel version of the union-find algorithm interleaved with a global synchronization step for each threshold sample. The efficiency of this algorithm stems from the fact that operations in-between threshold samples can be freely reordered, are mostly local and thus require no inter-process communication. Our algorithm is significantly faster than previous algorithms for this purpose, and is neither constrained by memory size nor number of compute nodes compared to the conceptually related algorithm for extracting augmented merge trees. This makes percolation analysis much more accessible in a large range of scenarios. We explore the scaling of our algorithm for different data sizes, number of samples and number of MPI processes. We demonstrate the utility of percolation analysis using large turbulent flow data sets.

Paper 14

In-situ visualization of large-scale turbulence simulations in Nek5000 with Paraview Catalyst

In-situ visualization on HPC systems allows us to analyze simulation results that would otherwise be impossible, given the size of the simulation data sets and offline post-processing execution time. We design and develop in-situ visualization with Paraview Catalyst in Nek5000, a massively parallel Fortran and C code for computational fluid dynamics applications. We perform strong scalability tests up to 2,048 cores on KTH's Beskow Cray XC40 supercomputer and assess in-situ visualization's impact on the Nek5000 performance. In our study case, a high-fidelity simulation of turbulent flow, we observe that in-situ operations significantly limit the strong scalability of the code, reducing the relative parallel efficiency to only $\approx 21\%$ on 2,048 cores (the relative efficiency of Nek5000 without in-situ operations is $\approx 99\%$). Through profiling with Arm MAP, we identified a bottleneck in the image composition step (that uses Radix-kr algorithm) where a majority of the time is spent on MPI communication. We also identified an imbalance of in-situ processing time between rank 0 and all other ranks. Better scaling and load-balancing in the parallel image composition would considerably improve the performance and scalability of Nek5000 with in-situ capabilities in large-scale simulation.

